The Potential of Cellulose Nanocrystals in the Detection and Treatment of Cancer

Katelyn Rose Colacino

Dissertation submitted to the faculty of Virginia Tech-Wake Forest School of Biomedical Engineering and Sciences in partial fulfillment of the requirements for the degree of:

Doctor of Philosophy
in
Biomedical Engineering

Yong Woo Lee (Chair)
Maren Roman
Luke E. K. Achenie
John L. Robertson
M. Nichole Rylander

June 20th, 2013
Blacksburg, VA

Keywords: Folate Receptor, Early Cancer Detection, Targeted Drug Delivery, Irreversible Electroporation

The Potential of Cellulose Nanocrystals in the Detection and Treatment of Cancer

Katelyn Rose Colacino

Abstract

Conventional methods of cancer therapy have been severely limited by inefficient delivery of therapeutic doses without incidence of harsh and toxic side effects in normal tissues. Consequently, countless new methods for early detection and drug delivery have been investigated in the area of nanoparticles and hydrogels. Although many of these methods are promising, the complex nature of cancer increases the difficultly for the development of the perfect system.

Cellulose nanocrystals (CNCs) have been studied widely for a variety of applications. Despite their advantages, investigations of their abilities in the biomedical field have not been explored. The goal of this project is to delve into the potential uses of CNCs in detection, targeted drug delivery, and potentiation of irreversible electroporation (IRE)-induced cell death in folate receptor (FR)-positive cancers. To accomplish this task we have prepared stable and reproducible CNCs from wood pulp *via* sulfuric acid hydrolysis. Furthermore, we have functionalized the surface of these nanoparticles and conjugated them with the targeting ligand folic acid (FA) and the fluorescent imaging agent fluorescein-5'-isothiocyanate (FITC) to create FITC-CNC-FA. CNCs have also been conjugated with doxorubicin (DOX), a potent chemotherapeutic (DOX-ALAL-CNC-FA). We have determined FITC-CNC-FA's and DOX-ALAL-CNC-FA's ability to specifically target FR-positive cancer cells *in vitro*; meanwhile non-targeted CNCs (FITC-CNC) were shown unable to bind to these cell types. In addition, we have investigated FITC-CNC-FA's pharmacokinetic activity *in vivo*. To properly model the CNC conjugate's activity *in vivo*, a physiologically based pharmacokinetic (PBPK) model has been constructed.

We have also examined CNCs' ability to potentiate a new technique for tumor ablation, IRE. Pre-incubation with FA-conjugated CNCs (CNC-FA) have shown an increase in cytotoxicity in FR-positive cancer cells induced by IRE. In addition, CNC-FA did not potentiate IRE-induced cytotoxicity in an FR-negative cancer cell type. For a more comprehensive understanding of CNC-FA's ability to potentiate IRE induced cytotoxicity, we optimized a 3D *in vitro* hydrogel

system. Preliminary data suggest this method of experimentation will be more realistic to *in vivo* studies to be completed in the future. Together, these studies showcase CNCs as efficient and effective nano-carriers in tumor detection and treatment.

Acknowledgements

This work has been put together with the immeasurable help and advisement of numerous individuals. I would first like to thank my advisor, Dr. Yong Woo Lee for imparting on me your knowledge and expertise in experimental design and execution. The countless hours of support and direction you have given me, has shaped me into a true scientist. Thank you for believing in me from the start; I am grateful to have had the opportunity to assist in the development of novel cancer therapies and extensively learn about cancer biology. Your attention to detail and laboratory directive skills are seldom matched. I am who I am today because of your significant influence and support; I could not have completed this work without you, and for that I am thankful.

I would also like to extend gratitude to my committee members for their tremendous insight. Their expertise in the various aspects on my project has opened my mind to new ways of thinking and problem solving. Dr. Roman, you have been an invaluable collaborator and mentor. Without you and your lab, I might still be trying to figure out the direction of my project. You are truly an expert in your field and it has been an honor working with you. Drs. Robertson, Achenie, and Rylander have all conducted independent studies with me, personalized around my dissertation studies. Dr. Bob, thank you for expanding my critical thinking abilities and for the hours you've spent with me and the mice; you were always more than willing to help me in any aspect of this project and you are an amazing scientist. Dr. Achenie, I would probably still be trying to open an .m file in Matlab without you. Your guidance in coding and mathematical modeling has truly been a gift and it has been a pleasure learning from you. Dr. Rylander, thank you for your thoughtful insights into my project. Your scientific curiosity and passion are aspects I hope to mimic in my own career.

I would especially like to thank my fellow labmates Hyung Joon Cho, Won Hee Lee, Anjali Hirani, and Paul Kim. You all have taught me many experimental and data analysis techniques as well as facilitated the conception, preparation and completion of my studies. During my research, I have collaborated with Shuping Dong, Dr. Christopher Arena, and Dr. Rafael Davalos. Without you, I would not have been able to accomplish a thorough investigation of this interdisciplinary project. I would also like to thank Kristen Zimmermann for her expertise in materials science and shared interest in nanoparticle design and formation. Special thanks go to

my undergraduate student Alex Callo, who has donated much of his time to becoming a successful scientist, and helped immensely in the execution of hydrogel experiments.

The administrative staff in the School of Biomedical Engineering and Sciences has ensured a smooth path to the completion of my degree. Thank you to Tess, Pam, Kathy, and Jo for being cheerful and diligent. I am especially grateful for Tess Sentelle; you have been extremely helpful and informative since I first took interest in this program.

I would like to extend thanks to all the friends I've made here at Virginia Tech. The life-long friendships I have formed with each of you have shaped my personality and kept my sane during crunch times. Thank you Joon, Szot, Kristen, Bill, Lyle, Mikey, Cara, Paulo, Ashby, and Kerry for your words of encouragement and great times spent together. I would also like to thank Kara, Jay, Kate and Bill who spent hours driving all the way from New York to continue being a part my life. You're visits have meant the world to me and I will always be thankful.

The biggest thanks go to my family and boyfriend Eric. Mom and Dad, we've spent hours talking about my research and I loved every single visit. You have supported me from day one and without it, I would not have continued into graduate school. I love you both so very much. Eric, you have endured all my good days and bad; thank you for putting up with all of my shenanigans and providing everlasting love and support. Having you here in Blacksburg has made this journey worthwhile and unforgettable. I love you dearly and am glad you are a part of my life.

Attributions

Several colleagues aided in the research and writing contained in this dissertation. A brief description of their contributions is included below.

Yong Woo Lee is the primary advisor and committee chair for this research. He has considerable insight and guidance on the plan and execution of research, and provided editorial revisions on all manuscripts.

Maren Roman contributed to the conception and design of experiments, interpretation of results, and provided editorial revisions to all manuscripts.

Shuping Dong developed and characterized all nanoparticle conjugates for this research. She contributed to the conception and design of experiments and is a co-author on all manuscripts in this research.

Chapter 3:

John Robertson dedicated time and effort in the design and execution of *in vivo* experimentation.

Luke Achenie spent countless hours teaching me Matlab and how to effectively execute a physiologically based pharmacokinetic model.

Chapter 4: Folate-Attached Cellulose Nanocrystals Potentiate Irreversible Electroporation-Induced Cytotoxicity in Cancer Cells

Rafael Davalos contributed to the conception and design of experiments, interpretation of results, and provided editorial revisions to the manuscript.

Christopher Arena developed unique electrical probes for experiments. He also contributed to the conception and design of experiments, interpretation of results, and provided writing and editorial revisions to the manuscript.

Hyung Joon Cho and *Joo Won Im* provided in-depth knowledge of Photoshop and their illustration expertise in creating Figure 4-6 of this manuscript.

Chapter 5:

Christopher Szot provided insight for the hydrogel formation and analytical techniques.

Katherine Prokop isolated collagen from rat tails used in these experiments.

Alex Callo heavily contributed to the design and execution of all experiments in this study.

Table of Contents

List of Figures

List of Tables

List of Terms and Abbreviations

2D:	two dimensional
3D:	three dimensional
A549:	FR-negative human lung cancer cells
AFS:	attachment factor solution
AFM:	atomic force microscopy
ALAL:	alanine-leucine-alanine-leucine
ANOVA:	analysis of variance
BNNT:	boron nitride nanotubes
CNC:	cellulose nanocrystal
DCC:	*N,N'*-dicyclohexylcarbodiimide
DI:	deionized
DMEM:	dulbecco's modified eagle medium
DNA:	deoxyribonucleic acid
DOX:	doxorubicin
ECH:	epichlorohydrin
ECM:	extracellular matrix
EDC:	1-ethyl-3-(3-dimethylaminopropyl)carbodiimide
EGTA:	ethylene glycol tetraacetic acid
EPR:	enhanced permeability and retention
FA:	folic acid
FBS:	fetal bovine serum
FITC:	fluorescein-5'-isothiocyanate
FR:	folate receptor
FR-α:	folate receptor alpha
HAEC:	human aortic endothelial cells, FR-negative
IRE:	irreversible electroporation
IVIS:	*in vivo* imaging system
KB:	FR-positive human HeLa contaminant cells
MDA-MB-468:	FR-positive human breast cancer cells
MRI:	magnetic resonance imaging

NHS:	N-hydroxysuccinimide
PBPK:	physiologically based pharmacokinetic
PBS:	phosphate buffered saline
PDI:	polydispersity index
PEF:	pulsed electric field
PET:	positron emission tomography
RFC:	reduced folate carrier
RT:	room temperature
TFA:	trifluoroacetic acid

Chapter 1. Introduction

1.1. Problem Statement

In the United States, cancer is the 2nd most common cause of death, following heart disease, and accounts for 1 out of every 4 deaths[6]. The general population talks about finding the cure to cancer as if one perfect solution exists. The search for the "magic bullet" in curing cancer has been elusive due to a number of reasons. Firstly, cancer is a complex consortium of diseases defined by the ability of abnormal cells to divide uncontrollably and occupy distant organs using the vasculature and lymphatic systems[2]. Furthermore, there are innumerable causes and risk factors for all types of cancer[6]. There are six major hallmarks of cancer as seen in Figure 1-1; these features are key to understanding not only the complexity of cancer, but how to overcome it.

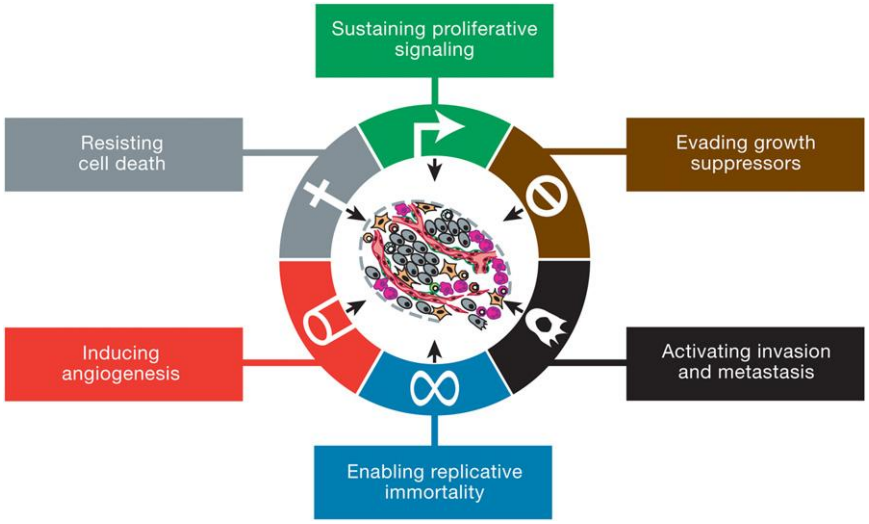

Figure 1-1: The hallmarks of cancer. This was reprinted from Hanahan et al.[2] with permission from Elsevier Inc.

A huge effort in the fight against cancer is the development of nanoparticles to effectively and efficiently deliver agents directly to cancer cells. In 2008 the National Institutes of Health estimated that the cost of cancer was $201.5 billion[6]. Furthermore, The National Cancer Institute budgets over $5.83 billion for their cancer research projects in 2013[7]. Despite this, there are currently only a fraction of nanoparticle formulations available in the market, most of which are untargeted[8]. There seems to be a gap in knowledge on how to optimize the design of nanoparticles. The Decuzzi and Ferrari groups have published multiple articles[4, 9-14] investigating optimal design of nanoparticle delivery, yet few have implemented their principles. This leads to particles that may work wonders *in vitro* but do not translate well *in vivo*.

1.2. Background

1.2.1. Conventional Cancer Treatments

Conventional methods of cancer therapy have been severely limited by inefficient delivery of therapeutic doses without incidence of harsh and toxic side effects in normal tissues. This is seen quite clearly with radiation therapy and chemotherapy[15]. Radiation therapy utilizes high doses of radiation to destroy cancer cells and shrink tumors. This treatment is non-specific, but the beams can be arranged in such a way where healthy tissue receives lower doses of radiation. When angled correctly, radiation beams cross where the tumor lies, creating an additive effect at that specific location. Radiation therapy still has harsh side effects associated with treatment including diarrhea, fatigue, changes in fertility, nausea and vomiting[16].

Chemotherapy is another common treatment plan for cancer patients. Depending on cancer type, a cocktail of chemotherapeutics is usually administered intravenously, repeatedly with recovery periods. Side effects include anemia, bleeding issues, constipation, fatigue, infection, fertility changes and pain[16]. Doxorubicin (DOX), a particularly toxic drug, is a chemotherapeutic which acts across multiple cancer types by intercalating into DNA and inhibiting cell division. Though extremely effective for inducing apoptosis in rapidly dividing cells, the free drug has no specificity and causes harm systemically. Cardiotoxicity is a major concern with this drug which limits the therapeutic dose to what healthy tissues can tolerate instead of ideal concentrations for cancer treatment[17-19].

Many external factors including diet, exercise, and tobacco use are known causes of cancer, yet for the most part, the general population has not changed their habits[6]. For this reason it is important to detect cancer early for the best possible rate of survival and increased quality of life. Some of the more common cancers, such as breast, prostate, and ovarian, have screening diagnostics to aid in early detection. Contrastively, no routine screening methods exist for the most deadly cancers, such as lung, pancreatic, and liver; moreover, these cancers show little to no early symptoms and may become metastasized before it is found[6].

1.2.2. Tumor Microenvironment

As shown in Figure 1-1, the tumor microenvironment plays an important role in the development of cancer. As a tumor grows, it releases growth signals to induce angiogenesis for better access to oxygen and nutrients. This new vasculature does not form in the same manner as

with healthy cells; branching is excessive, turbid, unorganized, and disproportionate with areas of blinded vascular endings, lack of a lymphatic system, and inadequate endothelial lining[20]. Pericytes and the basement membrane, in which normally provide structure to the vessels, are abnormal or absent, leading to fenestrae and increased permeability (Figure 1-2)[20, 21]. Though meant to provide a highway for nutrients, the tumor forms an irregular vasculature proving inefficient and unstable. This phenomenon leads to abnormal fluid transport dynamics in what's known as the enhanced permeability and retention (EPR) effect. Macromolecular drugs and nanoparticle tend to accumulate in the tumor tissue compared to normal tissue[22].

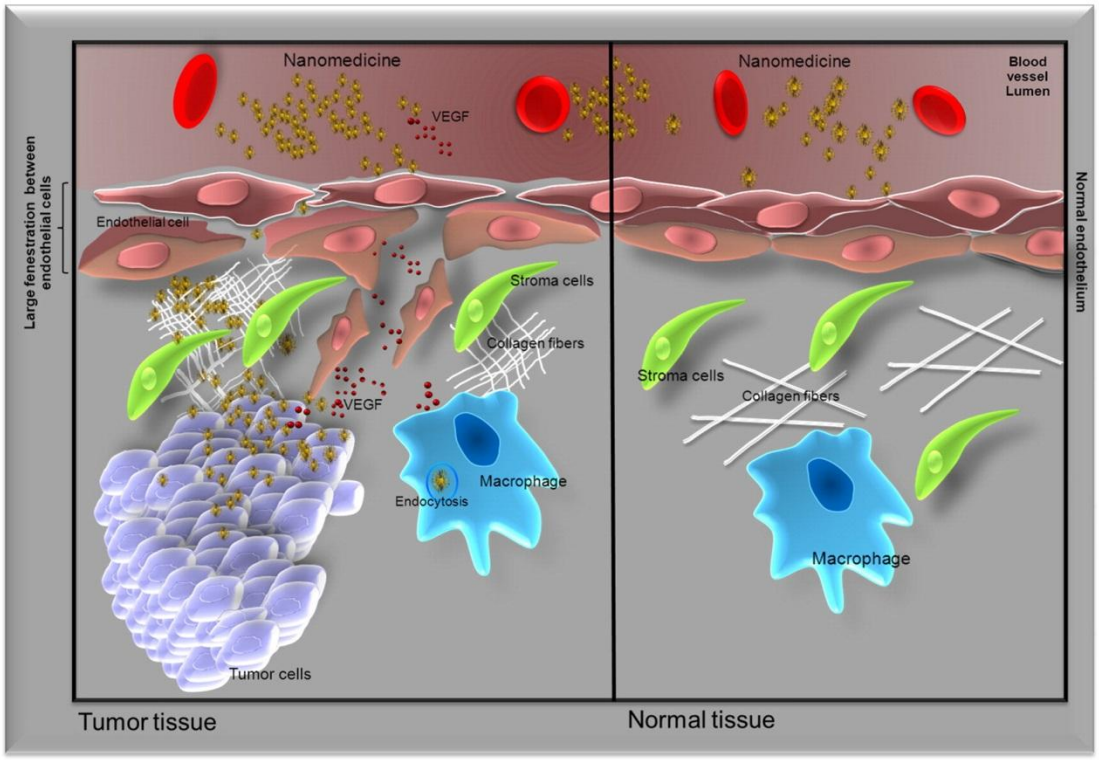

Figure 1-2: Differences between normal and tumor tissue in relation to the enhanced permeability and retention (EPR) effect. Normal tissue contains tightly connected endothelial cells which prevents the diffusion of the nanomedicine outside the blood vessel. Tumor tissue contains large fenestration between the endothelial cells allowing the nanomedicines to reach the matrix and the tumor cells by the EPR effect. Reprinted from Taurin et al.[1] with permission from Elsevier.

1.2.3. Folate Receptor

A few of the hallmarks relate to cancer's ability to evade death and become immortalized. During this process the cell undergoes phenotypical changes resulting in differing genes and proteins being expressed; one of which is the overexpression of the folate receptor (FR). The FR has been observed to be overexpressed in multiple cancer types including breast, ovarian, lung, kidney, brain, and endometrium[23-28]. The FR has a high affinity for folic acid, however it has

quite a low affinity for the most common form of folate in the body, 5-methyltetrahydrofolate. Healthy tissues require folate to undergo DNA replication yet they rarely express the folate receptor in large quantities. This is because there are two additional pathways for folate to enter a cell; the reduced folate carrier (RFC) and the proton-coupled folate transporter, both of which have a very low affinity for folic acid. The RFC is ubiquitously present in healthy tissues and explains low expression levels of FR in these sites[29, 30].

Unlike most endocytic pathways, the FR endosome does not experience a shift to a low pH. This is because FR containing endosomes do not traffic to lysosomes, but to recycling receptors to be sorted and recycled back to the plasma membrane (Figure 1-3). Interesting to note, because of its high affinity, folic acid remains bound to the FR during the entire endocytic pathway. Due to the endosome's lack of acidification (pH of 6.6-6.8), acid-labile linkers will not efficiently cleave or release drugs bound directly or indirectly to folic acid[30].

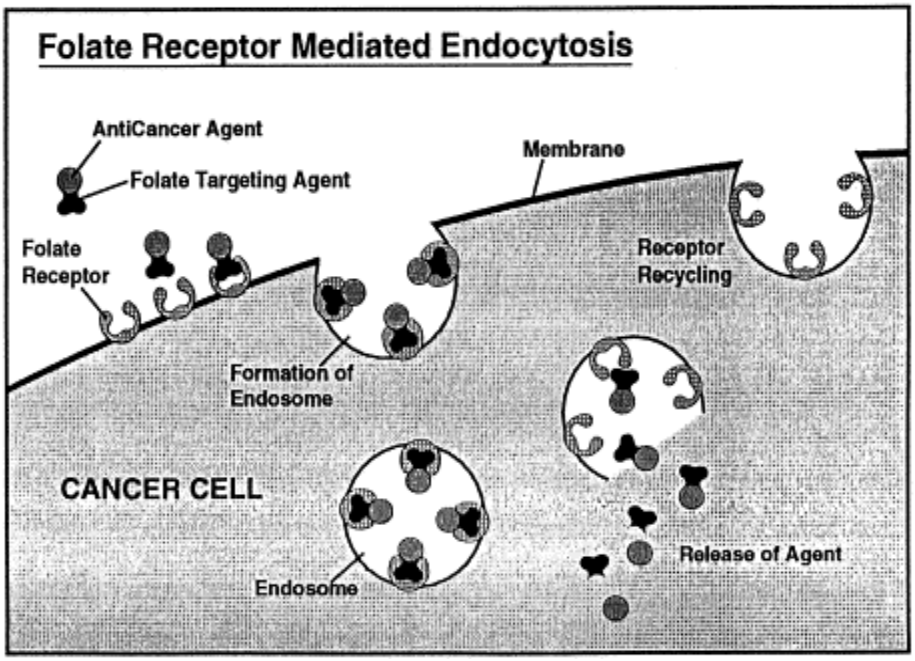

Figure 1-3: Diagrammatic representation of the folate receptor mediated endocytosis pathway. Covalent conjugates of drugs, macromolecules, or imaging agents linked to folic acid *via* the vitamin's γ-carboxyl group bind to the folate receptor with equal affinity to free folic acid (KD~50 pM). Following endocytosis and vesicular trafficking, much of the material is released into the cell cytoplasm. The unligated folate receptor may then recycle to the cell surface. Reprinted from Wang et al.[5] with permission from Elsevier.

1.2.4. Nanoparticles

Paul Ehrlich envisioned antibodies in search of toxins as "magic bullets" over a century ago (Figure 1-4). His efforts led to the findings of two "magic bullet" drugs in combat against malaria and sleeping sickness[31]. This ideal has given hope to many researchers in their search for treatments and cures for thousands of diseases. In the realm of cancer, the term "magic bullet" has been largely associated with targeted drug delivery *via* cancer-specific receptors. There has

been a heavy focus on chemotherapeutics being modified to selectively target cancer cells using various nano-carriers including liposomes, hydrogels, proteins, metals, polymers, dendrimers, micelles, and ceramics[32]. Currently there are about two dozen nano-delivery systems in clinical use while even more are in clinical trials[33]. Though many have great potential and have advanced cancer treatment in many ways, not one can be considered a "magic bullet." Cancer is a large group of complex diseases and these nano-carriers all have advantages and disadvantages in each case.

Over the past few decades, innumerous amounts of nanoparticles have emerged as potential carriers for drugs in cancer and other applications. Carbon nanoparticles are most commonly

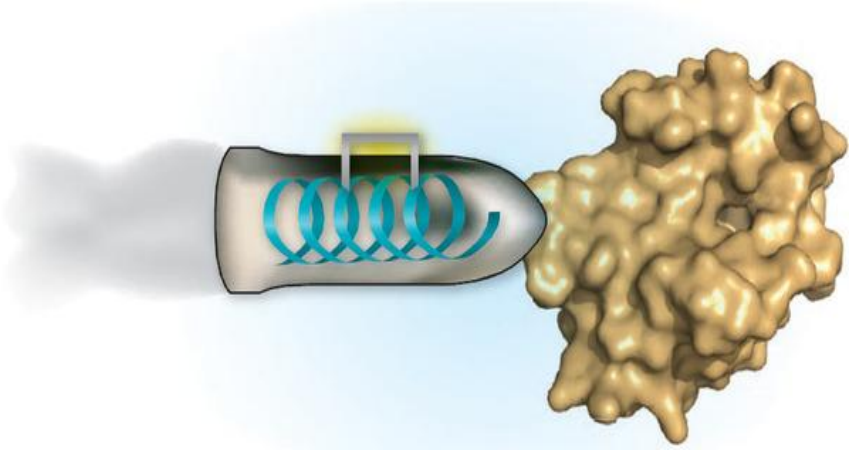

Figure 1-4: A primary goal of drug development is to design 'magic bullets,' compounds that selectively target only one of a closely related family of proteins. Reprinted from Kritzer[3], with permission from Nature Publishing Group.

high aspect ratio sheets of grapheme folded to form a tube; however they can range in shape, style and architecture from fullerenes, to multi-walled tubes, to nanohorns. One of the most popular nanomaterials for targeted drug delivery is graphene in the form of single and multi-walled nanotubes, horns, and spheres[34-36]. A major concern with this class of nanoparticles is their inherent hydrophobicity. Furthermore, these particles are not metabolized or degraded and tend to accumulate in the body. The surface of carbon nanoparticles can be modified to increase hydrophilicity yet the accumulation obstacle still poses a challenge. Lastly the aspect ratio of nanotube is dramatically high. These particles can range in length into the micron range while having a width of 1-2 nm. This aspect ratio makes it difficult if not impossible for the particles to be endocytosis by target tissues[34, 35] (Figure 1-5).

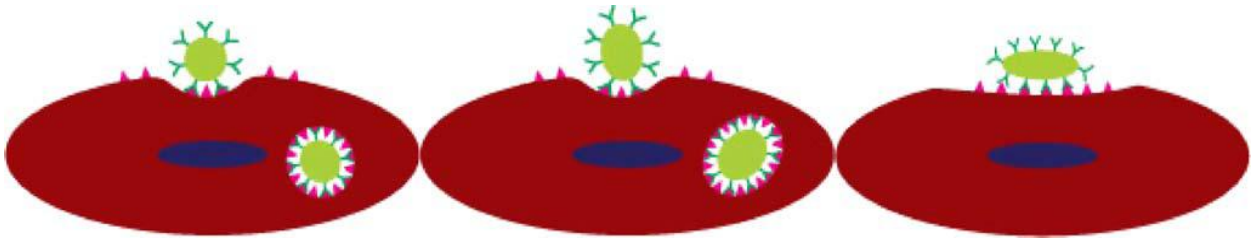

Figure 1-5: Controlling cell uptake by using particles with different shapes: ovoidal and spherical particles are more easily internalized compared to elongated particles laying parallel to the cell membrane. High aspect nanoparticles in receptor-mediated endocytosis are not preferential for uptake. Reprinted from Decuzzi et al.[4] with permission from Springer New York LLC.

Liposomes, usually spherical in shape, are engineered vesicles made up of a lipid bilayer. Normally they encapsulate a drug or delivery agent in their center and have moieties attached to their surface for targeting and biocompatibility[37]. Despite their versatility, their production costs can be quite high; they have short half-lives and comparatively low stability, and most are non-soluble. An additional concern with these types of nanoparticles is their retention and release properties of encapsulated drug. Leakage and fusion are both possible and unintended side effects[37, 38].

Increased circulation time by evading phagocytosis to more effectively reach the target tissue depends on the nanoparticles' size, shape, surface, and stiffness[13, 39]. Carriers should be composed of natural compounds and exhibit a neutral and hydrophilic surface. These properties describe a class of natural polymers known as polysaccharides to which cellulose nanocrystals (CNCs) belong[40]. According to Decuzzi et al.[11], a nanoparticle's shape is very important in drug delivery *via* circulation. They explain that nano-sized non-spherical particles tend to be pushed towards the vascular walls in laminar flow. This is why platelets are normally found in this region, while red blood cells are almost nonexistent. From this we can conclude that CNCs have a superior shape in circulation to reach targeted tissues through fenestrations.

On the opposite end of the spectrum, particles too small in size incur additional obstacles. There is an entire field dedicated to nanotoxicology and studying the differences between bulk materials and their nanosized counterparts[41, 42]. According to Alkilany et al.[43], gold nanoparticles of sizes under a diameter of 5 nm, display chemical reactivity, while bulk gold is chemically inert; this is due to nanoparticles greater surface area per mass property. Furthermore, nanoparticles of various materials have been shown to collect in lung tissue and evade the alveolar macrophages, a key defense mechanism in the lungs[44]. It is important to understand that

there are mechanical and chemical differences between different sized particles of the same substance as to not assume a non-toxic nature based on material.

1.2.5. Cellulose Nanocrystals

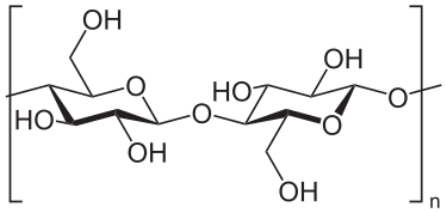

Figure 1-6: Molecular structure of cellulose.

CNCs are composed of an abundant, benign polymer and show promise in being a desirable nano-carrier for imaging probes and drugs[32]. In effect, there is a plentiful resource of generating CNCs with low cost. Cellulose (Figure 1-6), a starting material for the production of CNCs, can be degraded by reactive oxygen and nitrogen species, such as those used by phagocytes to break down phagocytosed materials[45]. Therefore, CNCs are not expected to accumulate permanently in mononuclear phagocytic system organs. Most importantly, cellulose is considered non-toxic and biocompatible, and it does not cause an inflammatory response in the body[46, 47]. Lastly, the use of polymeric nanoparticles *in vivo* requires them to be hydrophilic with a pH close to physiological values[48], which are properties of CNCs.

It has been known that acid hydrolysis of native cellulose fibers produces highly stable aqueous suspensions of CNCs[49, 50]. CNCs have large specific surface areas, and high strength and stiffness, making them viable candidates for a wide variety of applications[51]. However, the potential use of CNCs as targeted drug delivery carriers has not been investigated. A number of chemical and physical features have been presented by previous studies demonstrating CNCs as promising candidates for biomedical applications. For example, CNCs have a size range between 50 and 200 nm with the majority of the rod-like particles between 100 and 150 nm long. This is too large to be freely filtered by the renal system and yet small enough to delay clearance by the mononuclear phagocytotic system[52]. In addition, CNCs are composed of polysaccharide molecules making them hydrophilic which is expected to increase the life of CNCs in the blood stream seeing as the surface impedes adsorption of opsonin proteins, a critical step before phagocytosis. Therefore, CNCs are expected to have an inherent prolonged blood circulation half-life as compared to hydrophobic particles[53]. The surface of CNCs is abundant with hydroxyl groups. These groups are easily converted to functional groups for conjugation such as carboxyl groups for covalent and non-covalent binding of targeting and/or drug moieties to the surface[52, 54].

1.2.6. Irreversible Electroporation

Irreversible electroporation (IRE) is a non-thermal, focal ablation technique, which exposes cells to electric pulses to increase the permeability of the plasma membrane past the point of recovery[55]. This technique is especially useful in tumors that are inoperable due to their positioning near sensitive structures[56]. IRE damages the cell membrane of living cells, but it does not cause harm to the supporting stroma, including major blood vessels and extracellular matrix, in close proximity[57, 58]. The exact mechanism at the membrane scale is still under scrutiny. However the general consensus is that electroporation creates nano-scale pores in the plasma membrane (Figure 1-7). Electroporation can be reversible (below threshold) temporarily generating pores in the plasma membrane, or irreversible (above threshold) where pores are high in number or permanent disrupting the cell's homeostasis inducing cell death[59]. These reversible and irreversible zones are clearly defined regions of tissue with a sharp distinction between them. Like all techniques, IRE exhibits some disadvantages; it requires intense electric fields which can be painful at the localized site, and affect distant tissues, stimulating involuntary muscle contractions and cardiac arrhythmias[60, 61].

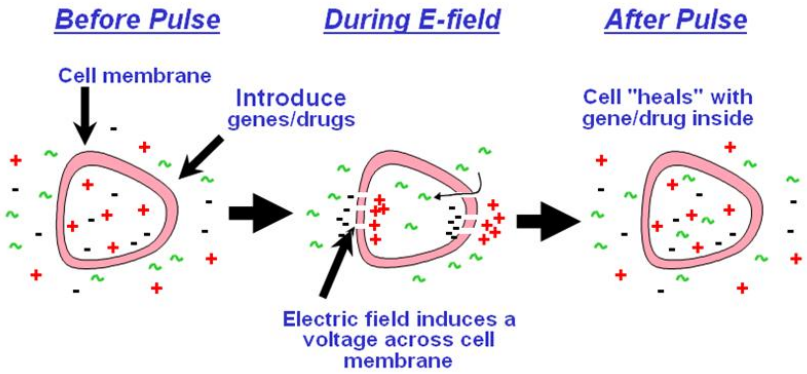

Figure 1-7: Pore-formation at poles of cell caused by reversible electroporation. This method can be used to introduce small molecules that would not normally be allowed to cross the membrane. With high electric field application the cell may not be able to recover causing irreversible electroporation and cell death. Reprinted with permission from Harvard Apparatus.

1.3. Hypothesis and Specific Objectives

The proposed set of studies is a collaborative effort between a polymer chemistry lab (Dr. Roman) and two biomedical engineering groups (Drs. Lee and Davalos) to assess the potential of CNCs as a novel carrier system for targeted imaging and drug delivery applications in FR-positive cancer cells. CNCs are rod-like polysaccharide-based nanoparticles, obtained by chemical degradation of purified cellulose starting materials, such as cotton or bleached wood pulp. Their advantageous chemical, physico-chemical, and mechanical properties have made

CNCs attractable for a wide range of potential applications[51, 52]. CNCs are particularly suitable for applications in the pharmaceutical and medical field due to their non-toxic nature and the biocompatibility of cellulose[62]. Although CNCs have promising attributes, their potential as carriers in imaging and targeted drug delivery applications have not fully been explored.

Previous studies indicate that CNCs are non-toxic to a number of different cell types[32, 52]. For cellular binding/uptake studies, there are developed chemical methods for fluorescent labeling of CNCs[40, 52], and conjugation of the targeting ligand folic acid (FA). FA has a high affinity and specificity for the FR which is highly overexpressed in most cancer cells[23-28]. The majority of normal tissue types obtain folate derivatives through the RFC which has a low affinity for FA[63, 64]. Our studies demonstrated that FA conjugation to fluorescently labeled CNCs increased binding and uptake of the nanoparticles in FR-positive cancer cells. Targeted CNCs conjugated with doxorubicin, a potent chemotherapeutic, (DOX-ALAL-CNC-FA), also selectively bind to the folate receptor and effectively deliver DOX to cancer cells inducing cell death. The apparent lack of cytotoxicity and potentially high cell targeting ability of CNCs suggest they possess benefits over current nanoscale carrier systems, which suffer from toxicity or low stability.

IRE, a non-thermal, focal ablation technique, exposes cells to electric pulses to increase the permeability of the plasma membrane past the point of recovery[55]. While IRE affects the cell membrane of living cells, it does not cause damage to the supporting stroma, including major blood vessels and extracellular matrix in the vicinity[57, 58]. This enables the treatment of tumors that are normally considered surgically inoperable due to their close proximity to these sensitive structures. The main drawback of this technique is its uniform distribution[55, 65]. Human tumors are for the most part non-uniform[66, 67]. They have branches of cancerous tissue which protrude from the main body of the tumor. To ensure complete eradication of tumor tissue *via* IRE, a large amount of the healthy tissue within the target region will also be subjected to necrosis. CNCs can be designed to accumulate at a target tissue, giving the ability to tune the electrical properties at the site of electroporation. This flexibility decreases the uniformity of IRE and can potentially spare normal tissue in the immediate vicinity of the tumor.

Our main hypothesis is CNCs, modified with a targeting ligand, have the ability to image, deliver chemotherapeutics, and potentiate IRE-induced cytotoxicity in human cancer. This hypothesis has been investigated through four specific objectives:

Hypothesis

Cellulose nanocrystals, modified with a targeting ligand, have the ability to image, deliver chemotherapeutics, and potentiate IRE-induced cytotoxicity in human cancer.

Specific Objective 1
Fluorescently labeled and chemotherapeutic loaded CNCs conjugated with folic acid selectively target folate receptor-positive cancer cells *in vitro*.

Specific Objective 3
CNCs conjugated with folic acid selectively target folate receptor-positive cancer cells to potentiate IRE-induced cytotoxicity.

Specific Objective 2
Fluorescently labeled CNCs conjugated with folic acid selectively target folate receptor-positive cancer cells *in vivo*.

Specific Objective 4
Hydrogels are a more intricate 3D *in vitro* model for assessing CNCs conjugated with folic acid ability to selectively target folate receptor-positive cancer cells to potentiate IRE-induced cytotoxicity.

1. **FITC or DOX attached CNCs conjugated with folic acid selectively target folate receptor-positive cancer cells *in vitro*:** Assess the potential of CNCs as a novel carrier system for cancer imaging applications. Conjugating CNCs with the targeting ligand FA and fluorescently labeling with fluorescein-5'-isothiocyanate (FITC) was observed to be selectively bound or uptaken into FR-positive cancer cells. Conjugating CNCs with the targeting ligand FA and chemotherapeutic DOX was observed to selectively target FR-positive cancer cells and induce cell death. These conclusions were observed through a series of experiments investigating cellular binding and uptake assays, competitive assays with FA, as well as cell viability assays in FR-positive cancer cell types (KB and MDA-MB-468).
2. **Fluorescently labeled CNCs conjugated with folic acid selectively target folate receptor-positive cancer cells *in vivo*:** Assess the imaging abilities of FITC-labeled CNC-FA conjugates *in vivo*. Pharmacokinetic analysis *in vivo* and through mathematical modeling has been completed. Preliminary data has been collected in

human breast cancer xenografted athymic nude mice. Successful completion of this specific objective will lead to development of targeted delivery systems of imaging agents *in vivo* as well as preclinical trials of early detection of FR-positive cancers.

3. **CNCs conjugated with folic acid selectively target folate receptor-positive cancer cells to potentiate IRE-induced cytotoxicity:** Assess the potential of CNCs conjugated with FA to potentiate IRE-induced cytotoxicity in FR-positive cell types. This was observed by comparing IRE-induced cytotoxicity with IRE + CNC-FA-induced cytotoxicity in FR-positive and FR-negative cancer cells.
4. **Hydrogels are a more intricate 3D *in vitro* model for assessing CNCs conjugated with folic acid ability to selectively target folate receptor-positive cancer cells to potentiate IRE-induced cytotoxicity:** Develop and fully optimize a hydrogel model for investigating CNC-FA's ability to potentiate IRE-induced cytotoxicity. Hydrogel parameters have been assessed in preliminary experiments. We plan to continue experimentation in the future.

1.4. Scientific Merit and Clinical Significance

While previous groups have investigated various materials and strategies for nanoparticle-mediated delivery in cancer, few have begun clinical trials, while even fewer have reached the market. Many formations suffer from toxicity and poor translation to *in vivo* models. Understanding the tumor microenvironment as well as the physical and chemical properties of a nanocarrier, more effective cancer detection methods and therapies can be developed and implemented.

This study examines the potential of cellulose nanocrystals to act as a non-toxic nanocarrier of imaging agents and chemotherapeutics, which can be modified for targeting purposes. This project utilizes interdisciplinary tactics to develop, characterize, and implement our nanoparticles. This work is the basis of a new nanocarrier to be used in clinical trials.

Chapter 2. Cellulose Nanocrystals Conjugated with Folic Acid Selectively Target Folate Receptor Positive Cancer Cells

Katelyn R. Colacino[1], Shuping Dong[2], Maren Roman[2], Yong Woo Lee[1, 3]

[1]School of Biomedical Engineering and Sciences, Virginia Tech-Wake Forest University, Blacksburg, VA

[2]Macromolecules and Interfaces Institute and Department of Sustainable Biomaterials, Virginia Tech, Blacksburg, VA

[3]Department of Biomedical Sciences and Pathobiology, Virginia-Maryland Regional College of Veterinary Medicine, Virginia Tech, Blacksburg, VA

Manuscript will soon be submitted to Biomacromolecules.

2.1. Abstract

The potential of cellulose nanocrystals (CNCs) as a nanocarrier for chemotherapeutics and imaging agents was investigated. Cellulose was broken down through sulfuric acid hydrolysis to form CNCs in the nanometer range. Folic acid was used as a targeting ligand and is attached to the surface of the CNCs. For imaging purposes, the CNCs were conjugated with fluorescein-5'-isothiocyanate (FITC). Alternatively, doxorubicin (DOX) was conjugated to the CNC surface *via* peptidase linker for targeted drug delivery. The particles were characterized by atomic force microscopy, dynamic light scattering, and ultraviolet spectroscopy. Both CNC conjugates (FITC-CNC-FA and DOX-ALAL-CNC-FA) showed selective targeting to folate receptor positive cancer cells, which offers a promising and potential avenue in cancer imaging and treatment.

2.2. Introduction

One of the most appealing applications of nanotechnology is specialized delivery is accomplished using novel systems in which selective targeting agents, therapeutic drugs, and imaging probes are conjugated to the surface or encapsulated within the particle[16, 32, 68, 69]. In addition, cancer imaging through multiple receptor targeting sites has been an attractive approach for the early detection of cancer in recent years[70]. Many factors are involved in designing the ideal nano-carrier system for such imaging probes. One must consider optimizing parameters, such as particle shape, size, surface, cytotoxicity, and circulation time[11]. Decuzzi et al. investigated optimal size and shape of nanoparticles to increase circulation time and accumulation at tumor sites. Particles that are spherically shaped were shown to be inefficient, since they tend to flow towards the center of blood vessels with laminar flow; while irregularly shaped or high aspect ratio nanoparticles tend to be pushed to the walls of blood vessels, similar to platelets. This increases the likelihood of nanoparticles entering tumor tissues through fenestrations in the vasculature[10, 11].

Cellulose nanocrystals (CNCs) are rod-shaped particles ranging in length from 50-200 nm and in width of 4-5 nm. This aspect ratio increases fenestration penetration compared to spherical particles, which many carriers are by design (liposomes[71-73], metals[74, 75], and dendrimers[76, 77])[13]. Furthermore, it has been observed that this size range is expected to be too large for quick renal clearance, yet small enough to evade the mononuclear phagocytic system[78]. However, due to their rod-like shape, it is possible for CNCs to orient themselves to pass through glomerular fenestrations in the kidney[79]. The starting material, cellulose, is extremely abundant in nature, with low cost and high strength properties[32, 51, 80]. The surface of CNCs contains multiple hydroxyl groups which are amendable to functionalized groups for ligand targeting, labeling of image probes, and drug conjugating.

The folate receptor (FR) has been observed to be overexpressed on the plasma membrane of many cancer cell types, including breast, ovarian, lung, kidney, brain, and endometrium; meanwhile, normal tissues seldom express the FR[23-28]. Folic acid (FA) is commonly used as a ligand for the FR due to its' high affinity. Furthermore, the hydrophilic and anionic nature of FA at physiologic pH precludes their passive diffusion through the plasma membrane. FA is a key vitamin for cell division and is needed by all cells to proliferate. However, the most common and biologically active form of folate is 5-methyltetrahydrofolate, not folic acid, which has means of

entering cells other than the FR, such as the reduced folate carrier (RFC) and the proton-coupled folate transporter[63, 64]. Overexpression of the FR is essential for rapidly dividing cells, which is evident in cancer cells.

Conventional methods of cancer therapy have been severely limited by inefficient delivery of therapeutic doses without incidence of harsh and toxic side effects in normal tissues. This is seen quite clearly with chemotherapy[15]. Depending on cancer type, a cocktail of chemotherapeutics is usually administered intravenously, repeatedly with recovery periods. Side effects include anemia, bleeding issues, constipation, fatigue, infection, fertility changes and pain[16]. Doxorubicin, a particularly toxic drug, is a chemotherapeutic which acts across multiple cancer types by intercalating into DNA and inhibiting cell division. Though extremely effective for inducing apoptosis in rapidly dividing cells, the free drug has no specificity and causes harm systemically. Cardiotoxicity is a major concern with this drug which limits the therapeutic dose to what healthy tissues can tolerate instead of ideal concentrations for cancer treatment[17-19].

In this study, we assessed the potential of CNCs as a novel carrier system for cancer imaging and treatment applications. Conjugating CNCs with the targeting ligand FA and fluorescently labeling with fluorescein-5'-isothiocyanate (FITC) was observed to be selectively bound/uptaken into FR-positive cancer cells. In addition, when DOX was attached to CNCs in place of FITC, these conjugates induced cytotoxicity equal to and greater than DOX alone. This was observed through a series of experiments including cellular binding and uptake assays, as well as cell viability assays in FR-positive cell types (KB and MDA-MB-468).

2.3. Materials and Methods

2.3.1. Materials

Dissolving-grade softwood sulfite pulp (Temalfa 93A-A) was kindly provided by Tembec, Inc. (Montréal, QC, CA). FITC, FA, genistein, doxorubicin, and dimethylsulfoxide were purchased from Sigma-Aldrich Corporation (St. Louis, MO, USA). Chlorpromazine was purchased from MP Biomedicals (Santa Ana, CA, USA). Folate-free RPMI 1640 medium, medium 200, low serum growth supplement, Concanavalin A Alexa Fluor® 594 and 633 conjugates, and donkey anti-goat Alexa Fluor® 488 were purchased from Invitrogen Corp. (Carlsbad, CA, USA). Goat poly IgG FR-α and goat non IgG primary antibodies and bovine serum albumin (BSA) were purchased from Santa Cruz Biotech (Santa Cruz, CA, USA).

Antibiotics (penicillin and streptomycin) and fetal bovine serum (FBS) were purchased from Mediatech, Inc. (Manassas, VA, USA). Spectra/Por dialysis tubes were purchased from Spectrum Lans (Rancho Dominguez, CA, USA). RNeasy Mini Kit was purchased from Qiagen (Valencia, CA, USA) according to the protocol of the manufacturer. Reverse Transcription System and CellTiter-Blue® Cell Viability Assay Kit were purchased from Promega (Madison, WI, USA). TaqMan® Universal PCR Master Mix, gene-specific TaqMan® PCR probes and primers were purchased from Applied Biosystems (Carlsbad, CA, USA). VECTASHIELD® HardSet Mounting Media with and without DAPI were purchased from Vector Labs (Burlingame, CA, USA). Attachment factor solution (AFS) was purchased from Cell Applications (San Diego, CA, USA). The human cancer cell lines KB, and MDA-MB-468 were purchased from American Type Culture Collection (Manassas, VA, USA) while human aortic endothelial cells (HAEC) were purchased from Invitrogen Corp. (Carlsbad, CA, USA). Remaining reagents and supplies were purchased from Fisher Scientific (Pittsburgh, PA, USA).

2.3.2. Instrumentation

Sonication was performed with an ultrasonic processor (Sonics & Materials Inc., Newton, CT, USA). CNC characterization data was observed using a Malvern Zetasizer NanoZS particle analyzer and Zetasizer Nano 4.2 software (Malvern Instruments Ltd., Malvern, UK). Atomic force microscopy (AFM) images were produced with an AFM equipped with an Olympus AC160TS tip (Olympus AC160TS, nominal tip radius < 10nm, spring constant 42 N/m) (Asylum Research, Santa Barbara, CA, USA). PCR results were observed and analyzed using a 7300 Real-time PCR System and 7300 Real-time PCR System Sequence Detection Software v1.2.3 (Applied Biosystems, Carlsbad, CA, USA). Fluorescence images were taken with a Leica AF6000 fluorescent microscope (Leica Microsystems Inc., Buffalo Grove, IL, USA). Confocal images were taken with a Zeiss LSM 510 Laser Scanning Microscope purchased from Carl Zeiss Microscopy LLC. (Thornwood, NY, USA). Cytotoxicity measurements were taken with a SpectraMax M2e microplate reader (Molecular Devices, Sunnyvale, CA).

2.3.3. CNC preparation

CNC suspension was prepared using sulfuric acid hydrolysis. Bleached softwood pulp was milled through a Wiley Mini Mill with a 60-mesh screen. 64 wt.% sulfuric acid (acid to pulp ratio 10 ml:1 g) was preheated to 45°C and mixed with the pulp. The hydrolysis reaction started

immediately with vigorous stirring for 1 h. The reaction was then quenched by a 10 fold dilution in ultra-pure deionized cool water and centrifuged at 4,550 × g for 10 min. The supernatant, which contains excess sulfuric acid, was removed and the pellet was washed with water before centrifugation once more. The resulting ivory colored gel was transferred to dialysis tubes with a molecular weight cut off of 12,000 – 14,000 and dialyzed against deionized water until the pH of the water stabilized to a near neutral pH (~6). The resulting suspension was sonicated using an ultrasonic processor (Model VC505) once at 200 Watts for 10 min, then centrifuged at 4,550 × g for 10 min to remove large particles.

2.3.4. Synthesis of CNC-NH_2

The amount of epichlorohydrin (ECH) and ammonia were in excess for CNC surface OH groups. 500 g of 3.44 wt.% CNC suspension was put into a 1,000 ml flask and cooled in an ice-water bath. 40 ml of 50% (w/v) NaOH aqueous solution was added slowly to the reaction flask under stirring. Next, 27.0 g of ECH was charged into the reaction flask with a fast stirring speed (around 500 rpm). The reaction mixture was heated to 60°C for 6 h. The reaction was stopped and the liquid mixture was transferred to a Spectra/Por dialyzing tube which was dialyzed against deionized water until pH reached around 12. After dialysis, the CNC suspension was transferred into a 1,000 ml flask and mounted with a mechanical stirrer. 90 ml of ammonia was added into the reaction flask under slow stirring. The reaction mixture was then heated to 60°C for 6 h. The reaction was stopped and immediately transferred into Spectra/Por dialyzing tubes to be dialyzed again. This time, the dialysis continued until the mixture was a stable pH. After dialysis, the suspension was cooled and sonicated in an ice-water bath at 150 watts for 10 min. The suspension was centrifuged at 4,550 × g for 12 min to remove aggregated larger particles; the supernatant was then collected. The gravimetric method[81] was used to conclude a concentration of 2.01wt%.

2.3.5. Synthesis of FITC-CNC

The reaction was designed as 1:1 molar ratio for CNC surface OH groups to FITC. Buffer solution was made by mixing 41.1 g sucrose, 0.76 g of ethylene glycol tetraacetic acid (EGTA), 3.52 g of NaCl, 7.64 g of $Na_2B_4O_7 \cdot 10H_2O$, and 240 ml of deionized water. All further reactions were protected from light with aluminum foil to not photo-bleach fluorescent molecules. 2.0 g of FITC was charged into an Erlenmeyer flask with 240 ml of buffer solution under stirring and

cooled by ice-water bath. Then, 50.0 g of 2.01 wt.% CNC-NH_2 suspension was added. After 4 h, an additional 140 ml of buffer solution was charged in to the reaction flask to completely dissolve the FITC. The reaction ran over night and was then stopped. The mixture was transferred into dialyzing tubes and dialyzed against deionized water until most of the free FITC was no longer in the dialyzing medium. The FITC-CNC suspension was collected and cooled to 4°C. The suspension was then sonicated at 200 Watts for 10 min in cool conditions. The sonicated suspension was centrifuged once at 4,550 × *g* for 12 min. The supernatant was further dialyzed two additional days until FITC was no longer detectable *via* absorbance peaks during a UV/Vis spectrum analysis. The weight concentration (wt.%) of the final FITC-CNC suspension was measured gravimetrically, which was 0.07 wt.%. FITC labeling ratio to CNC was measured and calculated by UV/Vis spectra.

2.3.6. Synthesis of FITC-CNC-FA

The reaction was designed as 3:1 molar ratio for CNC surface OH groups to FA. FA 0.12g (0.26 mmol) was charged into a reaction beaker with 20 ml of pH 7.2 PBS under stirring. Then 0.054 g of 1-ethyl-3-(3-dimethylaminopropyl)carbodimide (EDC) and 0.061 g N-hydroxysuccinimide (NHS) were added to the reaction mixture. The pH of reaction mixture was checked and adjusted to achieve a neutral pH with 0.02 M NaOH. 150.0 g of 0.1 wt.% FITC-CNC suspension was charged into the reaction beaker; the pH of the reaction mixture was checked and adjusted to neutral once more. The reaction was stirred at the room temperature for 40 h. After the reaction completed, the mixture was charged into a dialysis tube and dialyzed against deionized water until the media was mostly cleared of free FA. Then the FITC-CNC-FA suspension was transferred into a wide-mouth plastic jar and put into a refrigerator for 2 h to cool. The suspension was sonicated for 10 min at 200 Watts in an ice-water bath. After sonication, the suspension was centrifuged at 4,550 × *g* for 12 min to collect the supernatant, which was then dialyzed against deionized water again until there was no FA in the media detectable by UV/Vis spectrum analysis. The final clear yellow suspension was collected and stored at 4°C. The concentration was measured gravimetrically and was determined to be 0.08 wt.%. The complete synthesis scheme of CNC conjugates is described in Figure 2-1.

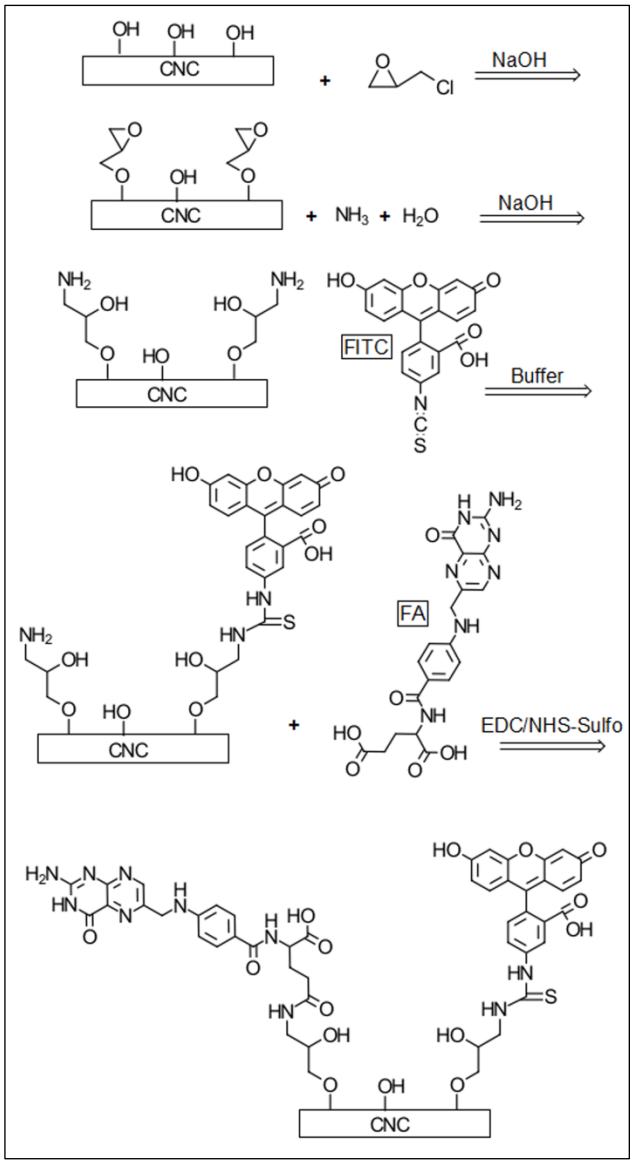

Figure 2-1: Synthetic scheme for preparation of FITC-CNC-FA. First the CNC surface was modified for the attachment of FITC. Next FITC was conjugated to the surface followed by FA.

2.3.7. Synthesis of TEMPO-oxidized CNCs

CNCs were oxidation to produce CNC-COOH *via* modified TEMPO-NaBr-NaOCl method[82]. 2.0 g of freeze-dried CNCs were pretreated with a 20% of NaOH solution for 1 h, and washed with DI water. The suspension was then added to TEMPO (80 mg) and NaBr (0.96 g) directly and kept at 30 °C, while 60 ml of 4% NaClO solution was slowly added under stirring. During the reaction, pH was monitored and adjusted with NaOH solution to keep pH slightly above 10. After 4 h, the reaction was quenched with addition of 1 ml of methanol. Then the solution was dialyzed against DI water until the pH of media was stable. The suspension was sonicated in an ice-water bath for 10 min and dialyzed for an additional day.

2.3.8. Synthesis of DOX with linker

42 mg of t-Boc-ALAL, 25 mg of DCC, and 14 mg of NHS were dissolved in 5 ml of anhydrous DMSO under stirring for 90 min. 50 mg of DOX.HCl was then added; the reaction was protected from light under stirring at room temperature for 48 hr. 2 ml trifluoracetyl acid (TFA) was added. After 30 min, the reaction mixture was transferred to a rotational evaporator and dried under vacuum.

2.3.9. Synthesis of FA-CONH-C_2H_4-NH_2

0.88 g of folic acid was dissolved in 60 ml DMSO at 50 °C, and 0.49 g of *N,N'*-dicyclohexylcarbodiimide (DCC) and 0.46 g of NHS was added under stirring. After 4 h, 2 ml of ethylenediamine (excess) and was kept under stirring for 48 h, at RT. 200-300 ml of acetal nitrile

(CH_3CN) was added to precipitate the final yellow product, which was collected by filtration under vacuum.

2.3.10. Synthesis of DOX-ALAL-CNC-FA

113 mg of 1-ethyl-3-(3-dimethylaminopropyl)carbodiimide (EDC) (0.55 mmol) and 119 mg of sulfo-NHS (0.55 mmol) were added to CNC-COOH (33.5 g, 1.11 wt.%, containing 0.5 mmol COOH) to activate the CNC-COOH. pH was adjusted to 7 and remained stirring for 2 h at RT. DOX-ALAL (0.086 mmol) was added for 24 h, and the suspension was transferred to a dialysis tube and dialyzed against DI water for 2 days. 113 mg of EDC and 119 mg of sulfo-NHS was added for 2 h. FA-CONH-C_2H_4-NH_2 (4 mmol) was then added and kept under stirring for 24 h. Then suspension was purified fully through dialysis against DI water until no UV/vis absorption peaks from folic acid or doxorubicin was detected within the dialysis medium (Figure 2-2).

2.3.11. Atomic force microscopy (AFM)

The suspensions were diluted to 0.001 wt.% and sonicated at 150 Watts for 3 min, then were directly dropped on a freshly peeled smooth mica surface and dried in ambient conditions. Later, the samples were scanned by AFM equipped with an Olympus AC160TS tip (nominal tip radius < 10nm, spring constant 42 N/m) in intermittent contact mode in ambient conditions. Height, amplitude, and phase images were collected as 5×5 μm scan size (512 scans, and 512 points/scan) for comparison and analysis.

2.3.12. Dynamic light scattering (DLS)

DLS measurements were conducted with a Malvern Zetasizer NanoZS particle analyzer (Malvern Instruments Ltd., Malvern, UK) at a wavelength of 633 nm from a 4.0 mW, solid-state He-Ne laser at a scattering angle of 173° at 25 ± 0.1°C. All samples were prepared in 0.01 wt.% concentration with deionized water. DLS was completed with clear disposable plastic cells (Malvern). Average diameters were calculated from the autocorrelation function using Malvern's Zetasizer Nano 4.2 software.

2.3.13. Zeta potential

The zeta potential was measured by electrophoresis coupled with laser Doppler velocimetry using a Malvern Zetasizer NanoZS instrument. All samples were measured at 0.01 wt.% shortly after sonication in a water bath (output: 100 Watts).

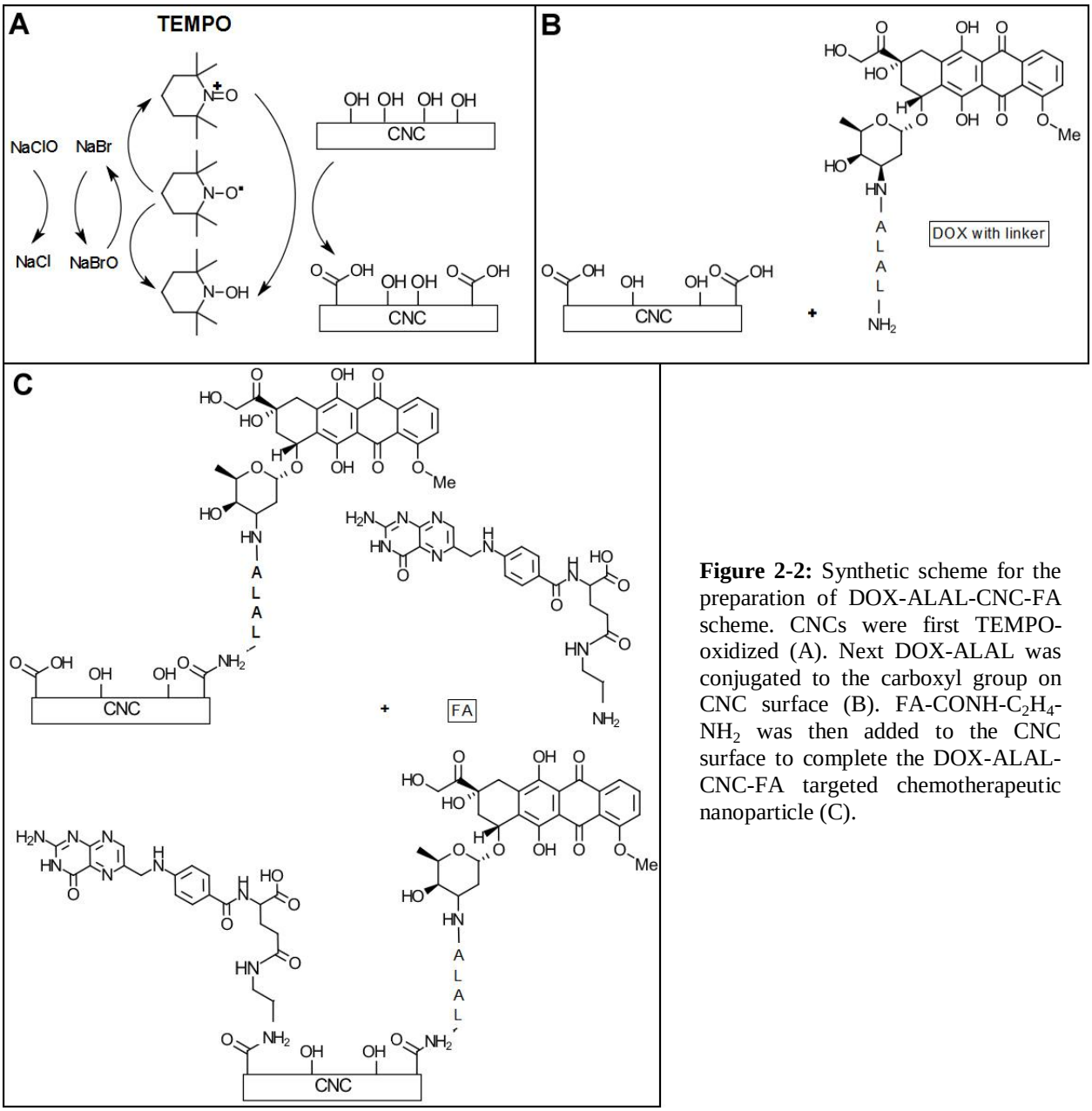

Figure 2-2: Synthetic scheme for the preparation of DOX-ALAL-CNC-FA scheme. CNCs were first TEMPO-oxidized (A). Next DOX-ALAL was conjugated to the carboxyl group on CNC surface (B). FA-CONH-C_2H_4-NH_2 was then added to the CNC surface to complete the DOX-ALAL-CNC-FA targeted chemotherapeutic nanoparticle (C).

2.3.14. Cell culture

HAEC were grown in Medium 200 supplemented with low serum growth supplement. KB and MDA-MB-468 cells were grown in folate-free RPMI 1640 medium supplemented with 10% FBS. Cells were grown at 37°C and 5% CO_2. All experiments were conducted in basal medium.

2.3.15. Real-time reverse transcription-polymerase chain reaction (RT-PCR)

Total RNA from HAEC, KB and MDA-MB-468 cells was isolated and purified using RNeasy Mini Kit (Qiagen, Valencia, CA, USA) according to the protocol of the manufacturer.

Quantitative real-time RT-PCR using TaqMan® probes and primers were used for gene expression analyses as described previously[83]. Amplification of individual genes was performed with Applied Biosystems 7300 real-time PCR system using TaqMan® Universal PCR Master Mix and a standard thermal cycler protocol. TaqMan® Gene Expression Assay Reagents for human FR-α and GAPDH were used for specific probes and primers of PCR amplifications. Cycle threshold cycle (CT) was determined, and relative quantification was calculated by the comparative CT method as described previously[83].

2.3.16. Fluorescence microscopy

HAEC, KB, and MDA-MB-468 cells were seeded on to Lab-Tek™ Chamber Slide™ systems coated with AFS and grown to confluency. Before imaging, cells were washed and mounted with VECTASHIELD® HardSet Mounting Medium with or without DAPI. Images were obtained with a Leica AF6000. A quantitative comparison of experimental groups was conducted by measuring the total fluorescence intensity normalized by cell area using ImageJ software (National Institutes of Health, Bethesda, MD).

2.3.17. Immunofluorescent staining

Cells were washed and fixed with 4% paraformaldehyde for 15 min. Cells were again washed and blocked with 3% BSA for 1 h. Cells were then treated with 4 µg/ml goat poly IgG FR-α primary antibody or goat non IgG antibody in 1% BSA solution overnight at 4°C. Cells were thoroughly washed and treated with 2 µg/ml donkey anti-goat Alexa Fluor® 488 in 1% BSA solution for 2 h at room temperature.

2.3.18. Binding/uptake assay

Cells were incubated with FITC, FITC-CNC, or FITC-CNC-FA at a FITC concentration of 5 µg/ml for 2 h. Cells were washed twice with PBS and the plasma membranes were briefly stained with 50 ng/µl of Concanavalin A Alexa Fluor® 594 for 2 min. Cells were then fixed with cold ethanol for 1 h.

2.3.19. Free folate inhibition assay

Cells were incubated with FITC-CNC-FA at a FITC concentration of 5 µg/ml containing 0, 5, 10, or 25 mM FA for 2 h. Cells were washed twice with PBS and the plasma membranes were

briefly stained with 50 ng/µl of Concanavalin A Alexa Fluor® 594 for 2 min. Cells were then fixed with cold ethanol for 1 h.

2.3.20. Binding/uptake mechanism assay

Cells were pretreated with PBS, 5 µg/ml chlorpromazine, or 200 µM genistein for 30 min. The medium was replaced with FITC-CNC-FA at a FITC concentration of 5 µg/ml containing PBS, 5 µg/ml chlorpromazine (clathrin inhibitor), or 200 µM genistein (caveolae inhibitor) for 2 h. Cells were washed twice with PBS and the plasma membranes were briefly stained with 50 ng/µl of Concanavalin A Alexa Fluor 594® for 2 min. Cells were then fixed with cold ethanol for 1 h.

2.3.21. Confocal microscopy

KB and MDA-MB-468 cells were seeded onto round coverslips coated with AFS and allowed to grow for 24 h at 37°C. Cells were incubated with FITC, FITC-CNC, or FITC-CNC-FA at a FITC concentration of 5 µg/ml for 2 h. Cells were washed twice with PBS and the plasma membranes were briefly stained with 50 ng/µl of Concanavalin A Alexa Fluor® 633 for 2 min. Cells were then fixed with cold ethanol for 1 h, washed twice with PBS, and mounted with VECTASHIELD® HardSet Mounting Medium. Images were obtained using a Zeiss LSM 510 Laser Scanning Microscope equipped with argon and helium-neon lasers. Images were analyzed using ZEN 2011 blue edition software (Carl Zeiss, Oberkochen, Germany).

2.3.22. Cell viability assay

KB and MDA-MB-468 cells seeded onto 96-well plates and incubated for 24 h. They were treated with various concentrations of DOX and DOX-ALAL-CNC-FA for 2 h, with or without a pre-treatment of 10 mM free FA for 30 min. Treatment medium was washed away and replaced with growth medium for an additional 22 h. 20 µl of CellTiter-Blue® Cell Viability Assay reagent was added to each well and incubated for 4 h. Fluorescence intensity was read with a SpectraMax M2e microplate reader at Ex/Em: 560/590 nm.

2.3.23. Statistical analysis

All statistical analysis of data was performed using SigmaPlot 11 (SPSS Inc., Chicago, IL). One-way analysis of variance (ANOVA) was used to compare mean responses among the

treatments. For each endpoint, the treatment means were compared using the Holm-Sidak method. Statistical probability of $p < 0.05$ was considered significant.

2.4. Results

2.4.1. Characterization

AFM images conclude CNCs to be an average length of 125 ± 75 nm and width of 4.5 ± 0.5 nm. Figure 2-3 is a qualitative analysis demonstrating the average size of CNC conjugates is larger than CNCs. Quantitative studies *via* DLS and zeta potential analysis revealed CNCs and CNC conjugates have a hydrodynamic radius between 80 and 180 nm and an overall negative surface charge. FITC-CNC contains 7.4 wt.% of FITC, while FITC-CNC-FA contains 3.7 wt.% of FITC and 22.9 wt.% of FA. Additionally, DOX-ALAL-CNC-FA contains 6.8 wt.% of DOX and 8.9 wt.% of FA (Table 2-1).

Table 2-1. Characterization data of CNCs and CNC conjugates.

Samples	Hydrodynamic Radius (nm/PDI)[1]	Zeta Potential (mV)[2]	CNC (wt.%)	FITC (wt.%)	DOX (wt.%)	FA (wt.%)
CNCs	81/0.23	–47(±2.4)	100.0	–	–	–
CNC-NH_2	161/0.35	–26(±1.7)	100.0	–	–	–
FITC-CNC	138/0.36	–37(±8.1)	92.6	7.4	–	–
FITC-CNC-FA	177/0.24	–40(±4.0)	73.4	3.7	–	22.9
DOX-ALAL-CNC-FA	177/0.48	-0.14(±0.074)	84.3	–	6.8	8.9

2.4.2. Folate receptor expression

Real-time RT-PCR and immunofluorescent staining revealed KB and MDA-MB-468 cells express significantly higher levels of FR-α mRNA and protein expression, respectively. It was observed that KB cells express FR-α mRNA over 8 million fold as HAEC, while MDA-MB-468 cells express over 7 thousand fold higher levels than HAEC (Figure 2-4A). Protein expression, as seen in Figure 2-4B, demonstrates similar results. Little to no expression of FR-α protein was detected in HAEC; however KB and MDA-MB-468 cells express significantly higher protein expression levels of FR-α.

[1] PDI: polydispersity index
[2] Data shown is mean ± standard deviation.

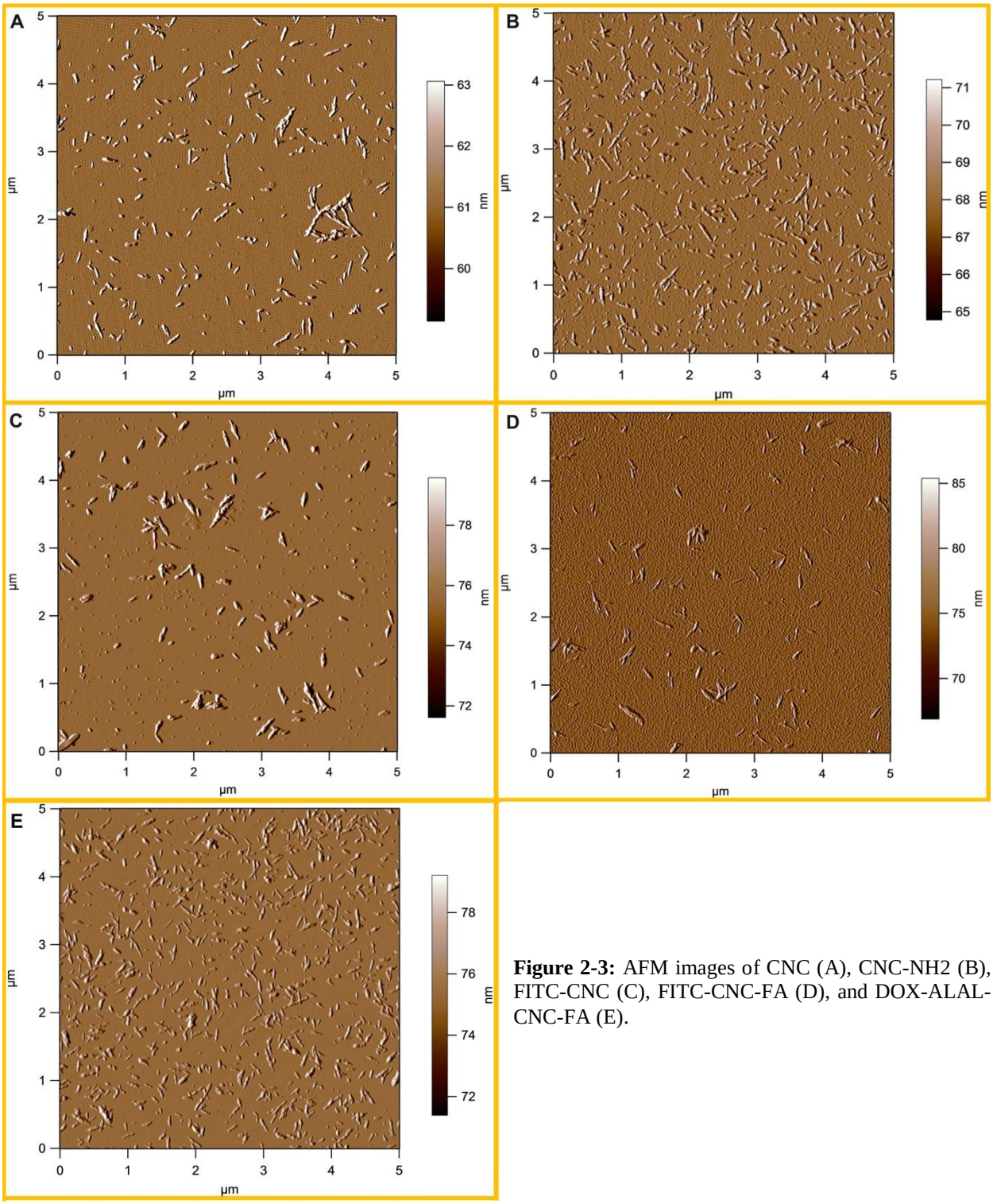

Figure 2-3: AFM images of CNC (A), CNC-NH2 (B), FITC-CNC (C), FITC-CNC-FA (D), and DOX-ALAL-CNC-FA (E).

2.4.3. Cellular binding/uptake assays

FR-positive cancer cells incubated with non-targeted free FITC and FITC-CNC exhibited little to no binding/uptake of these particles; however those incubated with targeted FITC-CNC-FA demonstrated significant binding/uptake of the particles (Figure 2-6). To confirm the targeting specificity of FITC-CNC-FA, they were placed in competition with increasing amounts of free FA to KB cells. As the free FA concentration increases to 25 mM, decreasing amounts of FITC-CNC-FA were observed bound/uptaken into KB cells (Figure 2-5). Furthermore, the mechanism in which mediated endocytosis of the FR was investigated. KB and MDA-MB-468 cells pre-treated with a clathrin inhibitor showed significant reduction of the binding/uptake of FITC-CNC-FA. Binding/uptake of FITC-CNC-FA was also significantly reduced by a caveolae inhibitor in MDA-MB-468 cells. This suggests the mechanism mediating endocytosis is cell dependent and non-exclusive. KB and MDA-MB-468 cells exhibited mostly clathrin-mediated endocytosis of the FR. Interestingly, MDA-MB-468 also significantly rely on caveolae-mediated endocytosis of the FR (Figure 2-7).

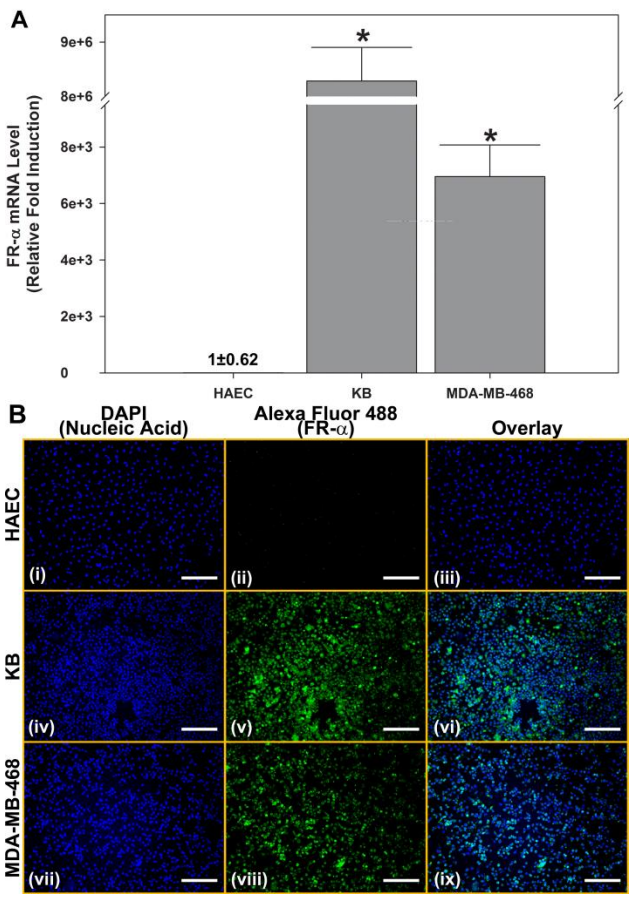

Figure 2-4: Expression levels of FR-α in HAEC, KB, and MDA-MB-468 cells. FR-α mRNA expression levels were determined by real-time RT-PCR (A). Data shown are mean ± SD for each group (n=4) (*p<0.05 vs. HAEC). FR-α protein expression levels were qualitatively confirmed by immunofluorescent staining (B). Data shown are representative images for each group (n=4) (Bar: 250 μm).

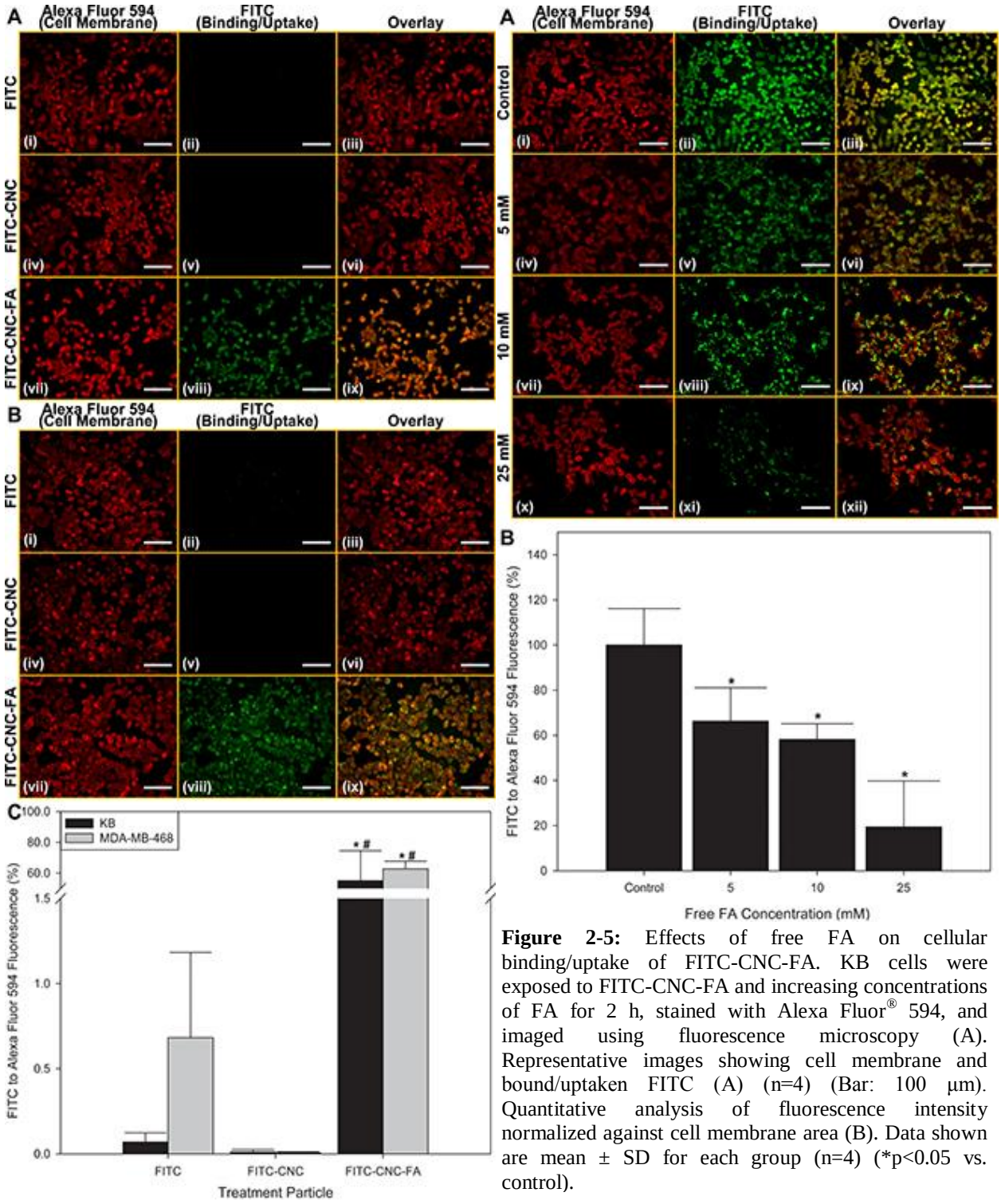

Figure 2-5: Effects of free FA on cellular binding/uptake of FITC-CNC-FA. KB cells were exposed to FITC-CNC-FA and increasing concentrations of FA for 2 h, stained with Alexa Fluor® 594, and imaged using fluorescence microscopy (A). Representative images showing cell membrane and bound/uptaken FITC (A) (n=4) (Bar: 100 µm). Quantitative analysis of fluorescence intensity normalized against cell membrane area (B). Data shown are mean ± SD for each group (n=4) (*p<0.05 vs. control).

Figure 2-6: Effects of free FITC (i-iii), FITC-CNC (iv-vi), and FITC-CNC-FA (vii-ix) on cellular binding/uptake. KB (A) and MDA-MB-468 (B) cells were exposed to either free FITC or FITC conjugates for 2 h, stained with Alexa Fluor® 594, and imaged using fluorescence microscopy. Representative images showing cell membrane (i, iv, vii), bound/uptaken FITC (ii, v, viii), and overlay images (iii, vi, ix), (A-B) (n=4) (Bar: 100 µm). Quantitative analysis of bound/uptaken particles represented by relative fluorescence intensity normalized against cell membrane area (C). Data shown are representative images for each group (n=4) (Bar: 100 µm). Data shown are mean ± SD for each group (n=4) (*p<0.05 vs. free FITC, #p<0.05 vs. FITC-CNC).

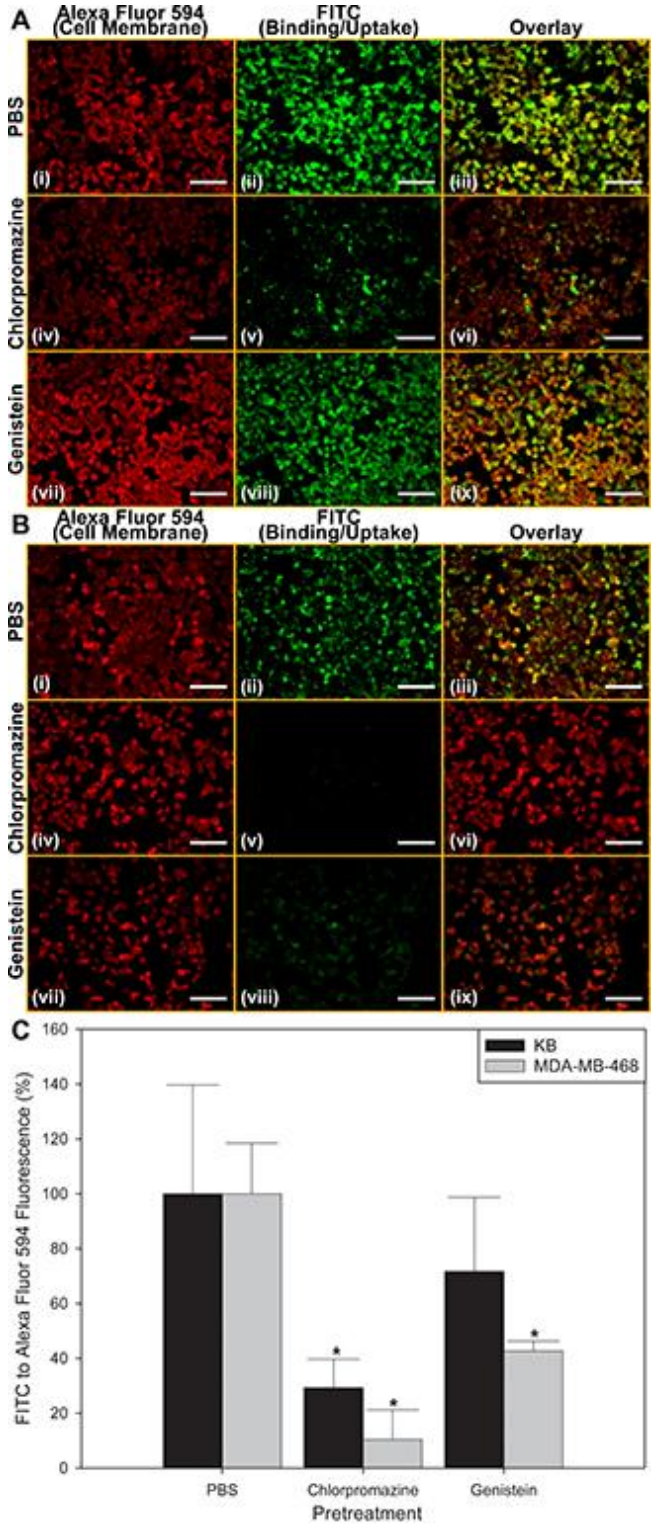

To confirm FITC-CNC-FA particles are being uptaken into FR-positive cancer cells, z-stacks of KB and MDA-MB-468 incubated with free FITC or FITC conjugates were investigated under confocal microscopy. When looking at an internal slice of the cell (Figure 2-8), not only is FITC-CNC-FA bound to the membrane of FR-positive cells, they are taken up into the cells.

2.4.4. Cell viability assay

Lastly chemotherapeutic loaded cellulose nanocrystals (DOX-ALAL-CNC-FA) were synthesized to observe the cytotoxic selectivity. In KB cells (Figure 2-9A), DOX-ALAL-CNC-FA were significantly better at inducing cytotoxicity than DOX alone. In MDA-MB-468 cells (Figure 2-9B) the nanoparticles were equally as strong as DOX alone. However, when each cell was pre-treated with free FA, there was an inhibition of cytotoxicity with DOX-ALAL-CNC-FA particles. This observation suggests the targeted nanocrystals can potentially reduce side effects of DOX by selectively killing FR-positive cells.

Figure 2-7: Effects of endocytosis inhibitors on cellular binding/uptake of FITC-CNC-FA. KB (A) and MDA-MB-648 (B) cells were pre-treated with PBS, 10 µg/ml chlorpromazine, or 200 µM genistein for 30 min, exposed to FITC-CNC-FA and inhibitors for 2 h, stained with Alexa Fluor® 594, and imaged using fluorescence microscopy. Representative images showing cell membrane and bound/uptaken FITC (A-B) (n=4) (Bar: 100 µm). Quantitative analysis of fluorescence intensity normalized against cell membrane area (C). Data shown are mean ± SD for each group (n=4) (*$p<0.05$ vs. PBS).

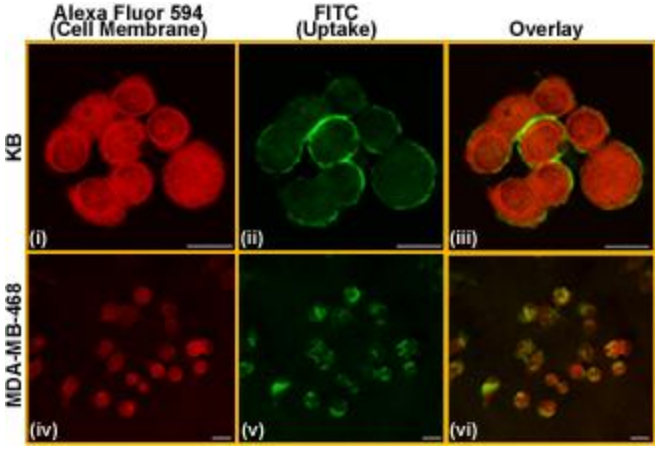

Figure 2-8: Effects of FITC-CNC-FA on cellular uptake. KB (i-iii) and MDA-MB-468 (iv-vi) cells were exposed to FITC-CNC-FA for 2 h, stained with Alexa Fluor® 633, and imaged using confocal microscopy. The left column of images (i, iv) show cell membrane staining, middle column images show FITC fluorescence, while the right column images show the overlay of the two channels. Representative images showing cell membrane and bound and uptaken FITC (n=4) (Bar: 20 µm)

2.5. Discussion

Advancements in the biomedical field have led to the formation of countless nano delivery vehicles. CNCs present characteristics in which they are showcased as an excellent choice as a nanocarrier. The starting material, cellulose, is one of the most abundant natural resources on the planet. Their shape lends them to be preferential for cellular uptake, their size increases circulation time, and their surface is abundant in easily modifiable hydroxyl groups for conjugating moieties[51]. The observations in this study demonstrate the potential of CNCs as novel nanocarriers for imaging agents and chemotherapeutics to selectively bind to and be uptaken by FR-positive cancer cells.

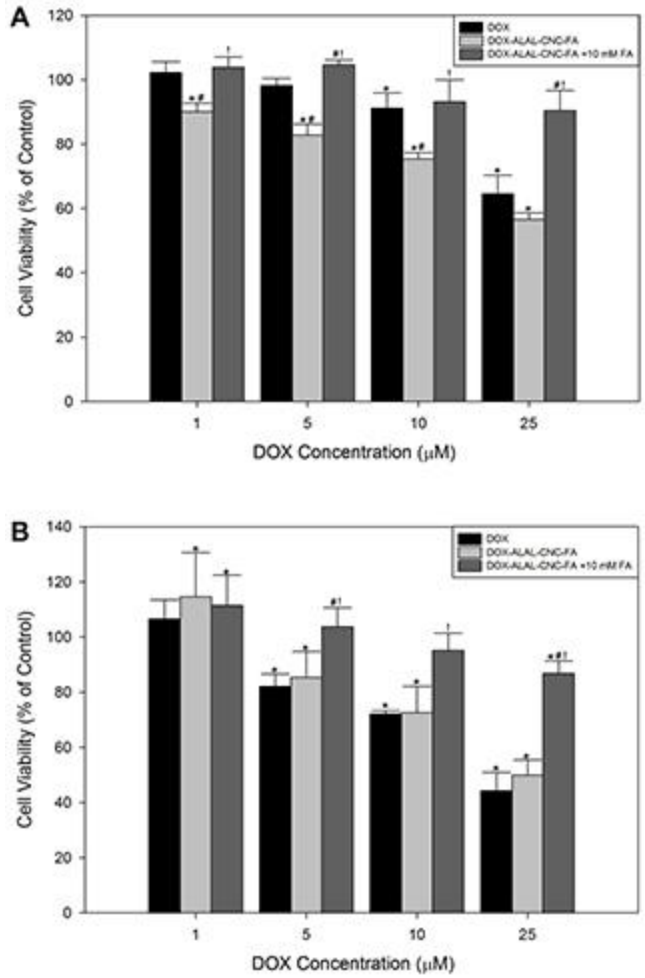

Figure 2-9: Effects of free DOX and CNC conjugation on cell viability. KB (A) and MDA-MB-468 (B) cells were exposed to either free DOX or DOX-ALAL-CNC-FA for 2 h, with or without a pretreatment of 10 mM free FA for 30 min. Medium was replaced with growth medium for 22 h post treatment. 20 µl of CellTiter-Blue® Cell Viability Assay reagent was added to each well and incubated for 4 h. Fluorescence was read at Ex/Em: 560/590 nm. Quantitative analysis of resorufin fluorescence intensity was normalized against cells treated with PBS, while CellTiter-Blue® reagent mixed with treatment solution was subtracted as background fluorescence. Data shown are mean ± SD for each group (n=4) (*$p<0.05$ vs. control, #$p<0.05$ vs. free DOX, †$p<0.05$ vs. DOX-ALAL-CNC-FA).

The selectivity of FITC-CNC-FA is ideal for uptake in FR-positive cells for imaging purposes, as there is no significant uptake observed with free FITC or FITC-CNC particles. Furthermore, the slight decrease in binding/uptake of FITC-CNC compared with free FITC can be attributed to particle size and surface charge. FITC-CNC particles are significantly larger than FITC molecules with an overall negative surface charge, giving them the inability to freely diffuse across the cell membrane.

When FITC-CNC-FA is inhibited by free FA there is a dose-dependent decrease in binding/uptake of FITC-CNC-FA to the FR. Although many studies have shown that 1 mM of free FA is a sufficient amount to inhibit binding of their FA targeted particles[84-87], Nukolova et al.[88] describe similar findings to ours with their folate-decorated nanogels. Our targeted nanoparticles show a much higher binding affinity than free FA which has a binding constant between 0.01 and 1 nM[89]. This can be very beneficial *in vivo*; since our particles have a higher affinity for the folate receptor, it is more likely that these particles will bind to FR-positive cell types efficiently instead of heavily competing with free FA already in circulation.

The endocytotic pathway *via* FR is known to be mediated by two proteins, clathrin and caveolin[90]. Our results suggest the FR is mainly dependent on clathrin-mediated endocytosis; however caveolae-mediated endocytosis plays a significant role in MDA-MB-468 cells. There have been many articles on both sides observing one particular cell type is dependent on clathrin while another is dependent on caveolin for FR endocytosis, suggesting that this dependency is clearly dependent on cell type[91-93].

Fluorescence microscopy has a large limitation in that images are two-dimensional. To further investigate whether FITC-CNC-FA is only binding to the plasma membrane or if uptake can be observed, we employed confocal microscopy. These results demonstrate that not only are the targeted particles binding to the cell membrane, they are being uptaken in both FR-positive cell types tested. These results show great promise in continuing investigations of CNCs ability as an imaging carrier for the detection of FR-positive cancer *in vivo*.

There is one major change in design between CNCs tagged with FITC for imaging and those loaded with DOX for drug delivery. DOX does not become actively cytotoxic without being cleaved from the particle[94]. This obstacle was not present during the imaging part of the study since FITC fluorescence was not hindering when attached to the CNC surface. Many foreign objects that are taken into the cell are transferred to lysosomes, where the pH is relatively acidic

to the outside environment[95]. After binding to the FR the endocytosis process engulfs the receptor and attached particle, but does not travel to a lysosome. Instead the endocytotic vesicle dissociates the receptor from the attached ligand and recycles the receptor back to the membrane. The pH in these vesicles unfortunately does not change much; therefore we could not rely on a pH cleavable linker[96]. In lieu, we chose to use a peptidase-liable linker (Ala-Leu-Ala-Leu)[97] to develop the final product, DOX-ALAL-CNC-FA. This linker is ideal for cleavage in FR endosomes because it is easily cleaved by a number of enzymes including cathepsin B[30, 97].

Moving forward with this study involves *in vivo* experimentation. Many challenges come into play here. Not only do we need to worry about which cells uptake our particles, we need to efficiently deliver our particles to the specific location where a tumor is present and travel through the vasculature. Furthermore the particles need to evade the macrophage and renal clearance systems long enough to optimize the efficacy of the nanoparticle delivery.

2.6. Conclusion

CNCs can be successfully prepared *via* sulfuric acid hydrolysis. Furthermore their surface easily allows for modification with moiety attachment. We have demonstrated that once conjugated with FA, CNCs are selectively uptaken by the FR. When additional moieties are attached, CNCs can actively deliver imaging agents and chemotherapeutics to FR-positive cancer cells and effectively release the chemotherapeutic for active cytotoxicity in the latter case.

2.7. Acknowledgments

This work was supported by the NSF (#DMR0907567).

Chapter 3. Pharmacokinetic Analysis of Cellulose Nanocrystals Conjugated with Folic Acid for use in Selectively Targeting Folate Receptor Positive Tumors

Katelyn R. Colacino[1], Shuping Dong[2], Maren Roman[2], Luke E. K. Achenie[3], John L. Robertson[1], Yong Woo Lee[1, 4]

[1]School of Biomedical Engineering and Sciences, Virginia Tech-Wake Forest University, Blacksburg, VA

[2]Macromolecules and Interfaces Institute and Department of Sustainable Biomaterials, Virginia Tech, Blacksburg, VA

[3]Department of Chemical Engineering, Virginia Tech, Blacksburg, VA

[4]Department of Biomedical Sciences and Pathobiology, Virginia-Maryland Regional College of Veterinary Medicine, Virginia Tech, Blacksburg, VA

Manuscript in preparation.

3.1. Abstract

In vivo pharmacokinetic analysis of cellulose nanocrystals (CNCs) as nanocarriers for imaging agents was investigated. Cellulose was broken down through sulfuric acid hydrolysis to form CNCs in the nanometer range. Folic acid was used as a targeting ligand and was attached to the surface of the CNCs; while fluorescein-5'-isothiocyanate (FITC) was used as a fluorescent imaging agent. CNC conjugates were injected into BALB/c mice *via* tail vein and the animals were euthanized 1, 4, 8, and 24 h post treatment. Blood and various organs were harvested and analyzed for clearance of FITC. Additionally, tumor bearing nude mice were injected with CNC conjugates and imaged using live techniques at the same time points. Mice exhibited no signs of toxicity during experimentation. Data collected was used to validate a physiologically based pharmacokinetic model to more finely predict the life cycle of CNC conjugates within the mouse.

3.2. Introduction

Breast cancer is the most common type of cancer and the second leading cause of cancer death in women in the USA[6]. It has been shown that most breast cancer cells up-regulate the FR expression compared to normal epithelial cells[98]. Furthermore, Hartmann et al.[24] provide evidence of strong correlations between FR overexpression in breast cancer and its reoccurrence, and overexpressed FR has been shown in lung, ovarian, colorectal and kidney cancers[23-27]. As cancer matures into the late stages, survival rate decreases drastically. For patients diagnosed with stage I breast cancer, the 5-year survival rate is about 88%; meanwhile patients with stage IV breast cancer have their survival rate cut down to 15%[99]. In lung cancer, patients diagnosed early on, with stage I have a 52% 5-year survival rate. Adversely, stage IV diagnosed patients have less than 3% chance of surviving past 5 years[100, 101]. Early detection could lead to decreased morbidity rates and a higher quality of life for cancer patients, in effect of less aggressive treatment regimens than in later stages of cancer.

Due to rapid development of screening methods, breast cancer and ovarian cancer early detection in women has dramatically improved[101]. Still, effective screening methods for most cancers do not exist, and the disease goes unnoticed until it becomes symptomatic in late stages. Strategies used to diagnose symptomatic cancer, including MRI, PET, and X-ray, can be used as screening methods, however the cost of running an MRI is extremely high and continued exposure radiation in PET and X-ray scans increases the risk of developing cancer and becomes a problem of risk vs. benefit[102]. Targeted nanoparticles can be used to more accurately map breast and ovarian cancers, and have the potential to be used as an early detection tool for FR-positive cancers lacking screening methods, such as lung and brain.

The complexity between a drug conjugate and the body cannot fully be understood with experimentation alone. Models provide valuable insight into the pharmacodynamics and kinetics of a system. More specifically, physiologically based pharmacokinetic (PBPK) models can be used to determine the life cycle of a drug introduced into the body's system. Factors such as flow, metabolism, clearance, and settling rates can be predicted and determined by PBPK models. Furthermore, these models can be well validated with data from small animal models. These two systems, PBPK and small animal models, complement each other in elucidating the interactions between drug and body system[103, 104].

As a continuation of the *in vitro* studies completed with FITC-labeled CNC conjugates, this study focuses on the *in vivo* imaging abilities and pharmacokinetic effects FITC-CNC-FA nanoparticles. Specifically, tumor bearing mice were administered FITC-CNC-FA conjugates and are imaged using a non-invasive *in vivo* imaging system. Furthermore, non-tumor bearing mice were administered free FITC and CNC conjugates to determine the pharmacokinetic effects.

3.3. Materials and Methods

All animal experiments have been approved by the Institutional Animal Care and Use Committee at Virginia Tech and were performed in accordance with the *Guide for the Care and Use of Laboratory Animals* published by the US National Institutes of Health.

3.3.1. Animal models

Four- to six-week-old female nude mice (Nu/Nu Nude Mouse, Crl:NU-Foxn1nu) were purchased from Charles River Laboratories (Wilmington, MA, USA). Additionally, female BALB/c mice were purchased from Harlan Sprague-Dawley (Indianapolis, IN, USA) for the purpose of pharmacokinetic analysis. Animals were maintained under environmentally controlled conditions and subjected to a 12 h light/dark cycle with food and water *ad libitum*. Normal mouse diets contain high amounts of folic acid which brings folate serum levels dramatically higher than that of humans. They were fed a low folate diet, Folic Acid Deficient Diet (TD.00434; Harlan Laboratories, Madison, WI, USA), for 2 weeks prior to the injection of tumor cells or CNC conjugates, and for the remainder of the investigation to decrease folate levels to around 25 nM, resembling normal human levels (9-14 nM)[86, 105].

3.3.2. *In vivo* tumor models

Female nude mice were subcutaneously inoculated in the right dorsal media area or right mammary fat pad, with FR-positive 1×10^6 KB or 5×10^6 MDA-MB-468 cancer cells, respectively[106, 107]. Prior to tumor cell injection, mice were anesthetized *via* inhalant isoflurane. Tumors were allowed to grow until they reached a size between 70 and 100 mm^3. Tumors were measured with calipers and the size was determined by the equation $½\times L\times W^2$ [19]. Mouse general health was monitored every other day by examining body weight, tumor size and ability to reach food and water.

3.3.3. *In vivo* optical imaging of FITC conjugates

Mice bearing tumors were treated with FITC-CNC-FA and imaged at 4 different time points. There was an additional control group treated with PBS and sacrificed at the final time point. Concentrations used were based on the amount of FITC in each treatment group. Based on preliminary experimentation, the concentration used was 0.5 mg/kg; since the average mouse weight was 20 g, each mouse received up to 0.5 mg/kg total FITC. Treatment was administered once *via* 100 µl tail vein injection and *in vivo* imaging occurred at 1, 4, 8 and 24 h post-treatment. Animals were anesthetized by XGI-8 Gas Anesthesia System that delivers inhalant isoflurane through a 5-port anesthesia manifold housed in the IVIS-200 (Caliper Life Sciences, Hopkinton, MA, USA) chamber and imaged using the GFP excitation and emission filters. This system is designed specifically for small animal, real-time, non-invasive fluorescent imaging. Quantitative data for tumor fluorescence was obtained by manually drawing a region of interest around the tumor's visible margins, and calculating the weighted percentage of fluorescence against fluorescent intensity throughout the mouse and background[18].

3.3.4. Biodistribution of FITC-CNC-FA in tumor models

The following analysis was described by Gabizon et al.[90] Immediately following imaging, mice were anesthetized with inhalant isoflurane for cardiac puncture; blood was collected, aliquoted, frozen and stored at -80°C. After thawing frozen blood, 100 µl of blood was added to 1.9 ml acidified ethanol giving a final dilution of 1:20 (v/v) and incubated at 4°C for 24 h protected from light. In addition, various tissues (liver, spleen, heart, lungs, kidneys, and tumor) were collected to determine the amount of FITC which has accumulated in each organ. Half of each tissue was weighed and added to acidified ethanol to create a 1:10 (v/v) dilution; they were then homogenized using a Power Gen 125 Homogenizer (Fisher Scientific, Pittsburgh, PA, USA) and incubated at 4°C for 24 h protected from light. Digested tissue and blood samples were centrifuged at 20,000 *g* for 20 min at 4°C to collect supernatant. The rate of disappearance or clearance of FITC was determined by measuring fluorescence using a SpectraMax M2e microplate reader (Molecular Devices, Sunnyvale, CA, USA). The concentration of FITC from each time point was calculated using a calibration curve with free FITC in whole blood. The control mice plasma were used as a baseline of the autofluorescence of blood[108].

The other half of each tissue was rinsed, embedded in CRYO-OCT compound (Andwin Scientific Tissue-Tek, Tryon, NC, USA), and stored at -80°C until further processing. 20 µm

thick slices of tissue were fixed to glass slides, mounted with VECTASHIELD® HardSet Mounting Medium with DAPI (Vector Labs, Burlingame, CA, USA) and imaged with a Leica DMI 6000 fluorescent microscope (Leica Microsystems Inc., Buffalo Grove, IL, USA).

3.3.5. Pharmacokinetic model *in vivo*

Female BALB/c mice were broken into 3 treatment groups and 4 time points. Treatment groups include free FITC, FITC-CNC, and FITC-CNC-FA; concentrations were based on the amount of FITC in each treatment group; 0.5 mg/kg. There was one set of control mice that was injected with PBS and sacrificed at the last time point. Treatment was administered once *via* 100 µl tail vein injection. Mice were anesthetized by inhalant isoflurane for blood collection *via* cardiac puncture at 1, 4, 8, and 24 h time points. Blood and tissue samples were analyzed as described in Section 3.3.4.

3.3.6. Physiologically based pharmacokinetic (PBPK) model

To accurately model the life cycle of FITC and CNC conjugates within the mouse, a PBPK model was developed. The aim of this modeling study is to develop a PBPK model, calibrated and validated with experimental data, to predict the time-dependent circulation and settling of FITC-CNC-FA in mice. This model is heavily based on the combination of four models proposed by Reisfeld et al.[103], Evjen et al.[109], Kona et al.[69], and Jones et al.[104]. The model compartmental design is shown in Figure 3-1.

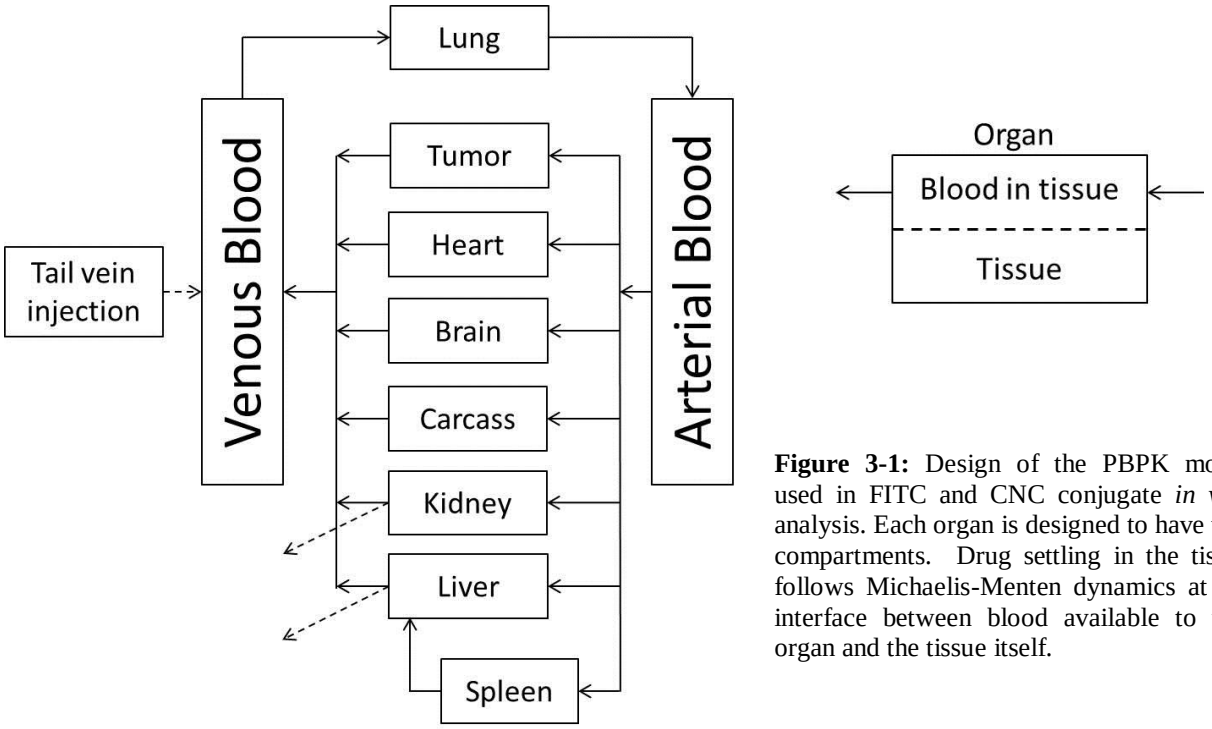

Figure 3-1: Design of the PBPK model used in FITC and CNC conjugate *in vivo* analysis. Each organ is designed to have two compartments. Drug settling in the tissue follows Michaelis-Menten dynamics at the interface between blood available to that organ and the tissue itself.

A number of assumptions can be made to simplify the model without drastically affecting the output. We first assume that there is no free FITC in circulation; this assumption is fairly reasonable considering no free FITC was detectably cleaved from FITC-CNC-FA particles *in vitro* (Chapter 2). The use of tissue homogenates in the previous experiment is appropriate for use in this modeling approach because compartments will be assumed to be "well mixed" and homogenous with respect to drug concentration. This is in contrast to studies of drug activity and efficacy, in which results derived from these types of samples could be misleading or erroneous[110]. In addition, we assume a flow-limited mass transfer in which the blood will be in quick equilibrium with the tissue upon entering that tissue.

Following are the governing equations for intravenous injections of FITC-CNC-FA. Each compartment has a mass balance for the injected drug. The mass balance for all organs excluding the lung, blood, kidney and liver is seen in Equations 1 and 2:

1

$$V_{organ}\frac{d(C_{organ})}{dt} = Q_{organ}(C_{AB} - C_{organ}) - V_{organ}\left(\frac{V_{max} * C_{organ}}{K_{max} + C_{organ}}\right)$$

2

$$V_{organ\ tissue}\frac{d(C_{organ\ tissue})}{dt} = \frac{V_{max} * C_{organ}}{K_{max} + C_{organ}} - CLR_{organ} * C_{organ\ tissue}$$

where C is the concentration of drug available in the blood of the organ, Q is the blood flow to the organ, and $V$is the volume of the organ. $C_{organ\ tissue}$ corresponds to the concentration of drug settling in each organ and follows Michaelis-Menten kinetics. CLR_{organ} is the clearance rate of the drug within the tissue *via* metabolism, lymphatic clearance, or other mechanism. The Michaelis-Menten parameters reflect the expression levels of the FR. Quick dynamics resemble more FR expression in that organ as seen in some normal tissues (brain, heart) and FR-positive tumors. Organ flows are fractions of cardiac output (QC) which was scaled to body weight of mice[103]. The mass balance of drug in the lung (C_{lung}) is governed by Equations 3 and 4:

3

$$V_{lung}\frac{d(C_{lung})}{dt} = Q_{lung}(C_{VB} - C_{lung}) - \frac{V_{max} * C_{lung}}{K_{max} + C_{lung}}$$

4

$$V_{lung\ tissue}\frac{d(C_{lung\ tissue})}{dt} = \frac{V_{max} * C_{lung}}{K_{max} + C_{lung}} - CLR_{lung} * C_{lung\ tissue}$$

The concentration of FITC-CNC-FA in the venous blood is given by Equation 5:

5

$$V_{VB\ volume}\frac{d(C_{VB})}{dt} = \sum\nolimits_{organs}\left(Q_{organ}(C_{organ} - C_{VB})\right) - VB_{Decay} * C_{VB}$$

where C_{VB} is the mass of the venous blood and VB_{Decay} is the rate at which FITC-CNC-FA is being cleared from the blood by the lymphatic and mononuclear phagocytic systems.

The governing equation for mass balance in arterial blood (C_{AB}) is given by Equation 6:

6

$$V_{AB\ volume}\frac{d(C_{AB})}{dt} = Q_{lung} * (C_{lung} - C_{AB})$$** ADD CLEARANCE EQUATION!

The kidneys and liver have an extra clearance term due to excretion and filtration, respectively. These terms are described in Equations 7 and will be subtracted from Equation 1:

7

$$E_{kidney} * C_{kidney}$$

$$F_{liver} * C_{liver}$$

where E_{kidney} is the rate of drug excretion by the kidney and F_{liver} is the rate of drug filtration by the liver.

Using these equations, parameters provided by literature[103, 104, 109], and parameters from our pharmacokinetic studies we will be able to accurately predict where FITC-CNC-FA will settle and clear from the body based on user input of dosage and frequency. This model was built in the MATLAB program (MathWorks, Natick, MA, USA) for its benefits in compartmental modeling.

3.4. Results

3.4.1. *In vivo* imaging studies

Throughout the study mice maintained their health. Their weights (Figure 3-2) stayed consistent overall and their activity level was unchanged. KB tumors rapidly grew and reached the desired minimum size for the experimental study. MDA-MB-468 tumors grew more slowly and most did not reach the desired minimum experimental size over 1 month (Figure 3-3). We chose to treat tumors once they reached desired size or in the case of MDA-MB-468 tumors at the end of 1 month.

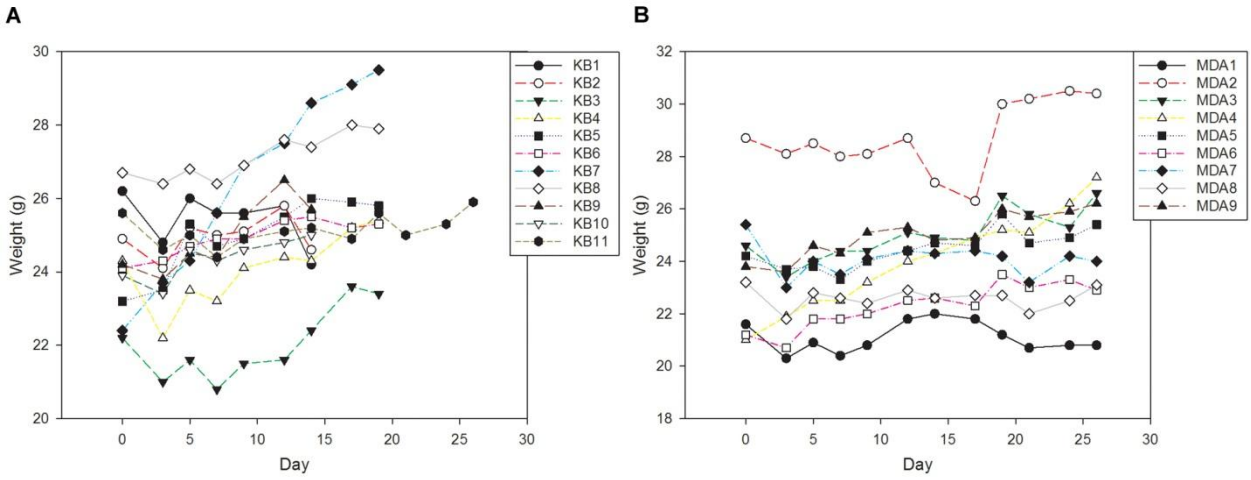

Figure 3-2: Mouse weights over experimental study. KB tumor bearing mice (A) and MDA-MB-468 tumor bearing mice (B).

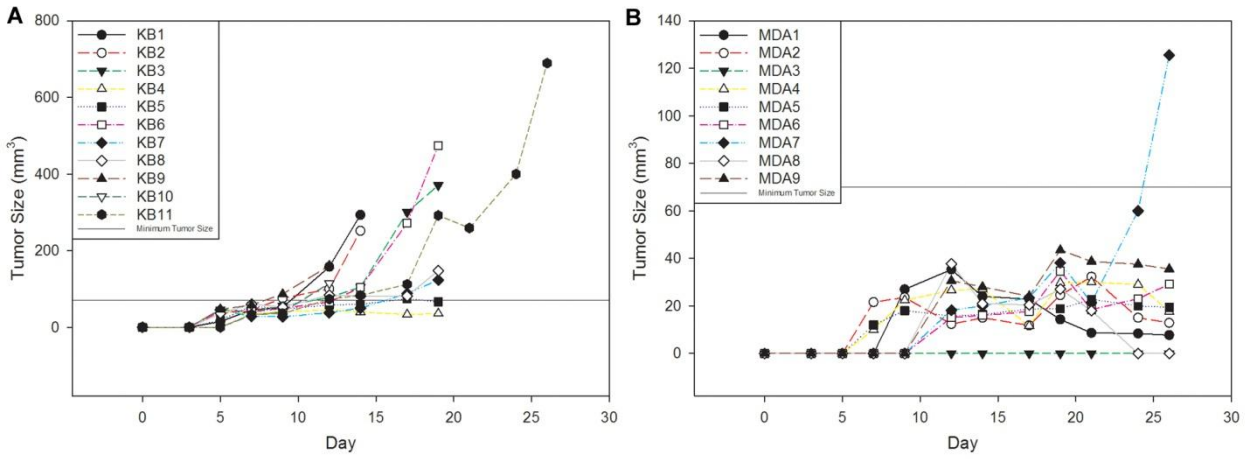

Figure 3-3: Tumor sizes over experimental study. KB tumor bearing mice (A) and MDA-MB-468 tumor bearing mice (B).

The highest concentration injected (0.5 mg/kg FITC) of FITC-CNC-FA was the only noticeable concentration able to be detected using the IVIS. Most KB tumor bearing mice did not show any targeted imaging due to missteps in tail vein injections and concentrations administered. Due to difficulties in tail vein injection, much of the injected dose of FITC-CNC-FA either was extravasated in the tail or not fully administered. Mice bearing MDA-MB-468 tumors were more successful in tail vein injection attempts. As seen in Figure 3-4, most of the injection for mice 1 and 4 did not enter the blood stream and was cleared relatively quickly from the tail. Mice 2, 3 and 5 show that most of the injection entered the blood stream (1 h post injection) and the CNC conjugate aggregated at the tumor site. In mice 3 and 5 (0.5 mg/kg FITC), accumulation at the tumor site was noticeable 4 h post injection while in mouse 2 (0.25 mg/kg FITC), it took 8 h for the nanoparticles to noticeably accumulate at the tumor site.

3.4.2. Pharmacokinetic analysis

FITC and CNC conjugates were nearly cleared from circulation 24 h post injection (Figure 3-5). Considering the blood concentration fold induction reaches over 5 for CNC conjugates, while the FITC fold induction barely reaches 3, more CNC conjugate mass remained in circulation over time. This is most likely due to the larger size of CNC conjugates compared with the small molecule FITC. Although the trends in each organ show some settling in the early time points, the fold induction of the drug concentration never reaches above 1.5. The kidney, which acts as a filter for the blood, is one of the few organs in which the cells normally express the folate receptor in small quantities; in Figure 3-5, we can observe all three variables injected seem

to accumulate here. In most other organs we can see a declining amount of the variables after 24 h, indicating clearance through the lymphatic or other system.

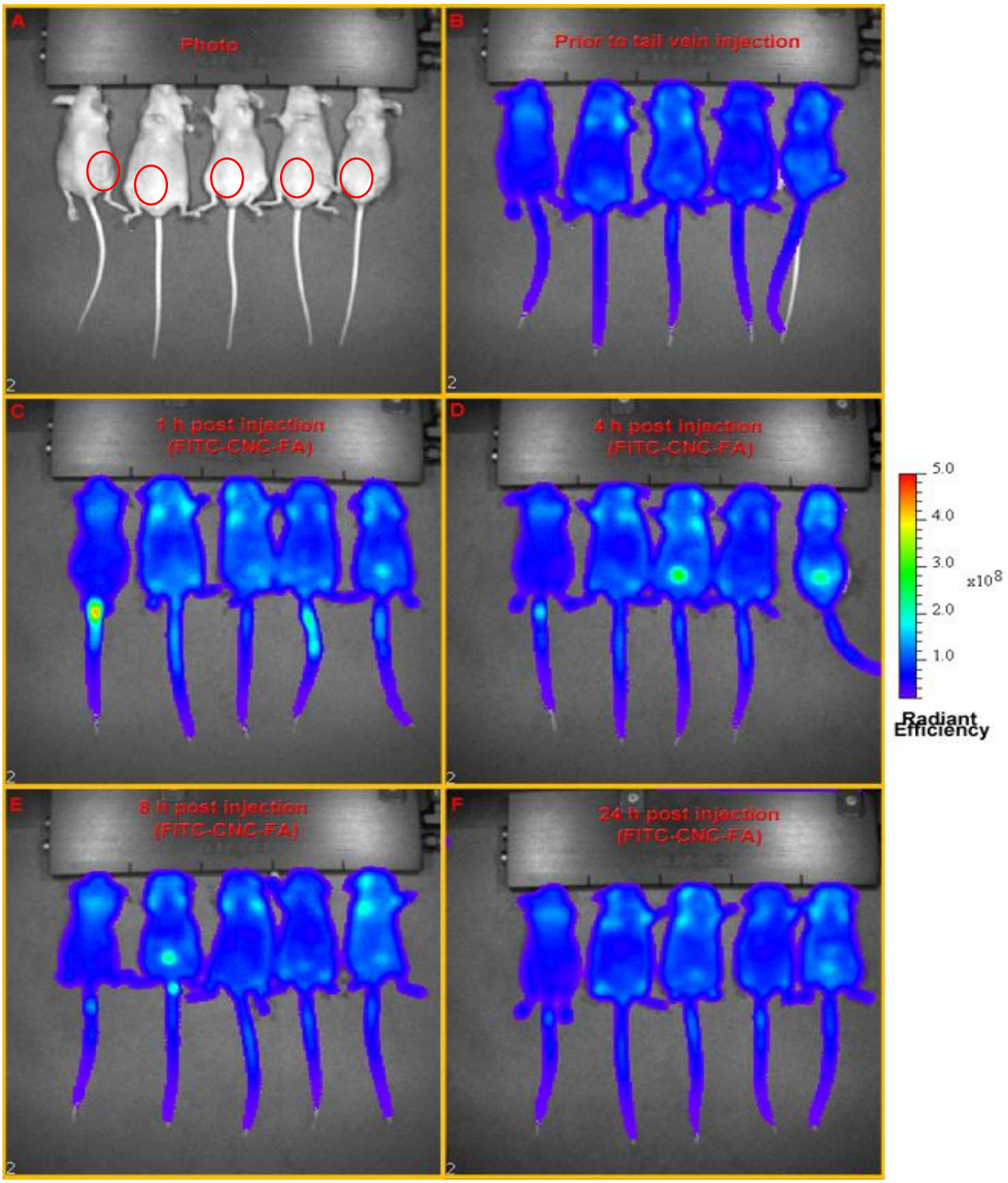

Figure 3-4: IVIS imaging of mice bearing KB and MDA-MB-468 tumors. Mouse 1 bears a KB tumor while mice 2-5 bear MDA-MB-468 tumors (counting from left to right). Mice 1, 3, and 5 received a dose of 0.5 mg/kg FITC concentration of FITC-CNC-FA, while mice 2 and 4 received 0.25 mg/kg FITC concentration. A photograph of mice without fluorescence can be seen in (A). Mice were imaged prior to (B) and 1 (C), 4 (D), 8 (E), and 24 (F) h post injection of targeted imaging agent, FITC-CNC-FA. Tumors are circled in red in (A). MDA-MB-468 tumors are difficult to see in (A) due to their size and location (mammary fat pad, not subcutaneous).

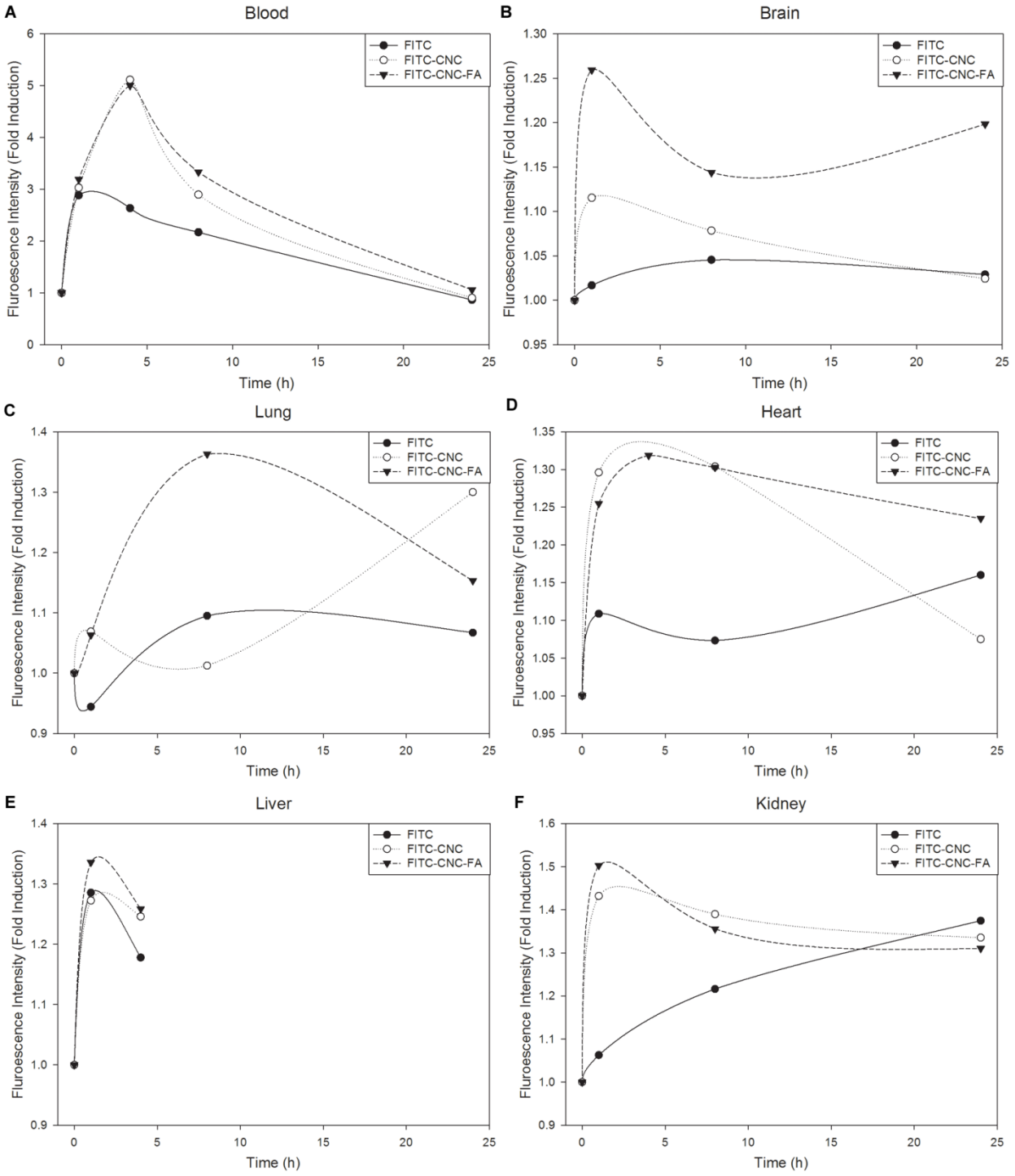

Figure 3-5: Experimental pharmacokinetic analysis of FITC, FITC-CNC, and FITC-CNC-FA over 24 h. Each datum represents n=1 to n=3. The graphs depict the blood (A), brain (B), lung (C), heart (D), liver (E), and kidney (F). In the case of the kidney results past 4 h were inconclusive and discarded from the results presentation.

3.5. Discussion

The amount of mice per group in these experiments was lower than estimated. According to power calculations and sample size analysis completed with SigmaStat 3.5 statistical software (Systat Software, Inc., Richmond, CA, USA), the number of animals to be used for significant difference verification is much higher. Based on inputs (minimum detectable difference in means: 35%; expected standard deviation: 20%; number of groups: 25 for pharmacokinetics, 4 for antitumor activity; desired power: 80%; α=0.050), we need at least 16 and 9 animals in each group for pharmacokinetic analysis and *in vivo* tumor imaging, respectively. Continuing these studies with more mice would strengthen the findings in this study and give a more thorough analysis of the pharmacokinetic effects.

The concentration of FITC-CNC-FA used in the imaging part of this study contains much less FITC then suggested by previous reports[111]. Though we were able to detect some aggregation of nanoparticles within the tumor model at the tumor site, a higher FITC concentration would increase contrast. To achieve this a few options exist; during synthesis of the CNC conjugate it may be possible to increase the amount of NH_2 groups on the modified CNC surface, or modify the reactive end of FITC prior to conjugate to make it more reactive with carboxyl groups on a TEMPO oxidized CNC, a method similarly seen with DOX-ALAL-CNC-FA synthesis. Furthermore, changing the cellulose source, such as bacterial or tunicin cellulose, would drastically help in changing the aspect ratio[112, 113]. Moreover, the synthesis and sterilization process of FITC-CNC-FA decreases the stock concentration; high centrifugation makes it possible to re-concentrate the solution allowing for a higher maximum dose for tumor bearing mice.

In addition, we assume accumulation at the target tissue through fenestrations in the tumor vasculature. The vascular nature in tumors is erratic and leaky; the high pressure levels seen in these sites, decrease blood flow and drainage[114]. Based on these facts, our particles will have to circulate the body multiple times before accumulation becomes significant. This is why increased circulation time is so important.

3.6. Acknowledgements

I would like to extend enormous thanks to Drs. Robertson and Achenie for their immeasurable insight and assistance in this study.

Chapter 4. Folate-Attached Cellulose Nanocrystals Potentiate Irreversible Electroporation-Induced Cytotoxicity in Cancer Cells

Katelyn R. Colacino[1], Christopher Arena[1], Shuping Dong[2], Maren Roman[2], Rafael Davalos[1], Yong Woo Lee[1, 3]

[1]School of Biomedical Engineering and Sciences, Virginia Tech-Wake Forest University, Blacksburg, VA

[2]Macromolecules and Interfaces Institute and Department of Sustainable Biomaterials, Virginia Tech, Blacksburg, VA

[3]Department of Biomedical Sciences and Pathobiology, Virginia-Maryland Regional College of Veterinary Medicine, Virginia Tech, Blacksburg, VA

Manuscript under review after submission to Annals of Biomedical Engineering.

4.1. Abstract

Cellulose nanocrystals are rod-shaped, crystalline nanoparticles that have shown promise for a number of industrial applications for their unique chemical and physical properties. However, investigations of their abilities in the biomedical field are limited. The goal of this study is to show the potential use of folic acid-conjugated cellulose nanocrystals in the potentiation of irreversible electroporation-induced cell death in folate receptor-positive cancers. After optimizing pulse parameters, we have shown cellulose nanocrystals' ability to potentiate a new technique for tumor ablation, irreversible electroporation. Pre-incubation with folic acid-conjugated cellulose nanocrystals has shown an increase in cytotoxicity induced by irreversible electroporation in folate receptor-positive cancer cells. In addition, folic acid-conjugated cellulose nanocrystals did not potentiate irreversible electroporation-induced cytotoxicity in a folate receptor-negative cancer cell type. Without changing irreversible electroporation parameters it is possible to increase the cytotoxic effect on folate receptor-positive cancer cells while not causing further damage to healthy tissue.

4.2. Introduction

Cancer is a class of diseases which varies widely from type to type, making multiple treatment options limited to certain forms. Conventional cancer therapies, including chemotherapy, radiation therapy, and surgery, have serious side effects which harm normal tissue in addition to the tumors. In recent years, a new type of therapy was developed, promising minimally invasive localized treatment of cancerous tissue, with little to no side effects[56, 115, 116]. Irreversible electroporation (IRE), a non-thermal focal ablation technique, exposes cells to electric pulses to increase the permeability of the plasma membrane past the point of recovery[55]. While IRE affects the cell membrane of living cells, it does not cause damage to the supporting stroma in the vicinity, including major blood vessels, nerves, and extracellular matrices[57, 58]. This enables the treatment of tumors that are normally considered surgically inoperable due to their close proximity to these sensitive structures. Another important feature of IRE is the high degree of control over the regions of tissue that experience irreversible, lethal electroporation and sub-lethal doses, made possible by careful selection of the electric field distribution and visualization in real-time on multiple imagining platforms, such as ultrasound[117].

At the membrane scale, the exact mechanisms behind IRE are not fully understood[118, 119]. When cells experience short and intense electrical pulses, there are position-dependent changes in the transmembrane potential that vary based on the cell radius and intensity of the electric field[120]. What remains unclear is the nature of the structural changes in the lipid bilayer that occur as a result of the induced transmembrane potential. The general consensus is the generation of small pores which, if plentiful or large enough, can permanently disrupt the cell's homeostasis and induce cell death[121]. One challenge associated with IRE is that all cells, healthy or cancerous, are subject to structural changes if their transmembrane potential is raised above a critical threshold. However, *we hypothesize that the selectivity of IRE can be potentiated through the use of cellulose nanocrystals (CNCs) functionalized to selectively target cancer cells.*

Nanoparticles can be designed to accumulate at a target tissue, enabling an increase in the treatment volume at the site of electroporation. To serve in this function, nanoparticles should be thermally and chemically stable, insulative, and noncytotoxic. The first group to utilize nanoparticles in combination with IRE demonstrated that boron nitride nanotubes (BNNTs) could potentiate IRE-induced cytotoxicity by lowering the required electric field for treatment[68]. Little is known about the biological effects of BNNTs, but studies have shown them to be

remarkably cytotoxic[122, 123]. As Raffa et al.[68] explain, their cytotoxicity is highly dependent on BNNT production methods and final aspect ratio of the particles. Even with ideal properties, BNNTs have been shown to be noncytotoxic only below a concentration of 500 ng/ml.

CNCs share most of the advantages of BNNTs, including their insulative properties[124]. Furthermore, CNCs have been shown to be noncytotoxic to a multitude of cell types at concentrations as high as 50 µg/ml[32, 125]. CNCs are rod-shaped particles which are relatively simple and inexpensive to produce, and their size is readily controlled *via* sulfuric acid hydrolysis[32, 40, 52]. Additionally, CNCs possess an abundance of hydroxyl groups which are easily converted to functional groups to conjugate drugs, imaging labels, and targeting ligands, such as folic acid. It is widely known that many cancer cells over express the folate receptor (FR) which has a high affinity for folic acid (FA)[29, 52, 87, 126, 127]. By exploiting this fact we can produce particles which target specific areas.

In this study, we demonstrated the ability of FA-conjugated CNCs (CNC-FA) to significantly potentiate the cytotoxicity of IRE on cancer cells. Specifically, key IRE parameters were optimized to elucidate the maximum potentiation effect of conjugated CNCs. Sensitive parameters of IRE include cell radius, pulse duration and intensity[65]; two of which are easily modified. In addition, parameters pertaining to CNC-FA must be evaluated, including concentration and incubation time before electroporation. The optimal incubation time coincides with a peak in membrane bound CNCs, prior to the completion of endocytosis. While some pulse parameters were chosen according to the literature[65, 128-130], the pulse length was optimized with nanoparticle pretreatment while a number of pulsed electric fields (PEFs) were tested across FR-negative and FR-positive cancer cell types.

4.3. Materials and Methods

4.3.1. Materials

Dissolving-grade softwood sulfite pulp (Temalfa 93A-A) was provided by Tembec, Inc. (Montréal, QC, CA). Fluorescein-5'-isothiocyanate (FITC), FA, and dimethylsulfoxide were purchased from Sigma-Aldrich Corporation (St. Louis, MO, USA). Folate free RPMI 1640 and Concanavalin A Alexa Fluor® 633 conjugate were purchased from Invitrogen Corp. (Carlsbad, CA, USA). Antibiotics (penicillin and streptomycin) and fetal bovine serum (FBS) were purchased from Mediatech, Inc. (Manassas, VA, USA). The human cancer cell lines KB, A549,

and MDA-MB-468 were purchased from the American Type Culture Collection (Manassas, VA, USA). The ECM 830 Electro Square Porator was purchased from Harvard Apparatus Inc. (Holliston, MA, USA). The Luxtron m3300 fiber optic temperature kit was purchased from LumaSense (Santa Clara, CA, USA). CellTiter-Blue® Cell Viability Assay Kit was purchased from Promega (Madison, WI, USA). VECTASHIELD® mounting medium was purchased from Vector Labs (Burlingame, CA, USA). Attachment factor solution (AFS) was purchased from Cell Applications (San Diego, CA, USA).

4.3.2. Nanoparticle formulation and characterization

CNCs were prepared as previously described[32] *via* sulfuric acid hydrolysis of dissolving-grade softwood pulp and dialyzed against deionized water. Hydroxyl groups on the CNC surface were partially converted to carboxyl groups (CNC-COOH). More detailed information on the preparation and characterization of nanoparticles can be found in Dong et al[32]. FA was conjugated to carboxyl groups *via* amide bonds (CNC-FA). For imaging studies, CNC-FA was labeled with the fluorescent molecule FITC to create FITC-CNC-FA. Determined by dynamic light scattering, the CNCs had a hydrodynamic diameter of 75 nm (data not shown). The percent weight of FA to CNC-FA was 22.9%.

4.3.3. Cell culture

All cell lines were grown in folate free-RPMI 1640 supplemented with 10% FBS and containing 100 IU/ml penicillin and 100 µg/ml streptomycin. Cells were grown at 37ºC and 5% CO_2. All experiments were conducted in folate free-RPMI 1640 basal medium.

4.3.4. IRE parameter optimization and CNC-FA potentiated IRE

250 µl of KB, A549, or MDA-MB468 cells were seeded into 48-well plates at 2×10^5 cells/ml and allowed to grow for 24 h to create a confluent monolayer. Growth medium was replaced by basal medium with or without CNC-FA (1 ng/ml – 10 µg/ml) and incubated for up to 1 h before application of IRE. IRE was applied using custom plate electrodes made to fit a standard 48-well plate. Specifically, the plates were machined from stainless steel to be 6 mm wide and placed 0.8 cm apart. The pulse repetition rate (1 Hz) and pulse number (80) were held constant, while the applied voltage and pulse duration were varied between treatment groups. Following treatment, CellTiter-Blue® reagent was added to each well and incubated for 4 h at 37ºC. Cell viability was

measured with a SpectraMax M2e microplate reader (Molecular Devices, Sunnyvale, CA, USA) at Ex/Em: 560/590 nm.

4.3.5. Confocal microscopy

1 ml of KB or MDA-MB-468 cells were seeded onto round coverslips coated with AFS at a concentration of 2×10^5 cells/ml. Cells were incubated at 37ºC for 24 h. Cells were treated with FITC-CNC-FA for 10 and 20 min, respectively, washed thoroughly with HBSS and fixed with ethanol for 1 h at room temperature. Cell membranes were stained with 50 ng/µl of Concanavalin A Alexa Fluor® 633 for 2 min. Cells were then washed with PBS and mounted onto glass slides with VECTASHIELD® mounting medium. Confocal images were taken with a Zeiss LSM 510 purchased from Carl Zeiss Microscopy LLC. (Thornwood, NY, USA). Images were processed using ZEN software (Carl Zeiss Microscopy LLC., Thornwood, NY, USA).

4.3.6. Numerical modeling

A three-dimensional finite element model was constructed using a commercial software package (COMSOL Multiphysics 4.2a, Burlington, MA, USA) to illustrate the clinical benefit of incorporating CNCs into IRE protocols. The methods for calculating the electric field distribution are similar to those found in previous reports[131, 132] for the treatment of liver tissue. Briefly, the electric field (E) distribution was obtained by solving the governing equation ($-\nabla\cdot(\sigma_d E) = 0$) with a dynamic electric conductivity function ($\sigma_d = \sigma(|E|)$). The dynamic conductivity function describes how electroporation occurring at the cell scale affects the bulk tissue conductivity as a function of the field magnitude. It was defined as a Heaviside step function with a continuous second derivate that transitions from 0.067 S/m to 0.241 S/m over a range of electric fields (500 V/cm to 800 V/cm[132]). The electrodes (1.0 cm spacing, 1.0 mm diameter) were modeled as needles with blunted tips projecting 1 cm out of an insulative sheath inserted into the center of the tissue domain (15 cm cube). To reduce computational burden, the physical electrode domains were removed from the geometry by subtracting them from the tissue domain to reduce the number of elements. Electric potential boundary conditions of 2000 V and 0 V were applied along the exposed surfaces of the energized and grounded electrodes, respectively. All remaining boundaries were treated as insulation. An extra fine mesh was used that resulted in 951364 elements and less than 1% difference in field at the center of the domain upon successive refinements.

4.3.7. Statistical analysis

All statistical analyses of data were performed using SigmaPlot 11 (SPSS Inc., Chicago, IL, USA). One-way analysis of variance (ANOVA) was used to compare mean responses among the treatments. For each endpoint, the treatment means were compared using the Holm-Sidak method. Statistical probability of $p < 0.05$ was considered significant.

4.4. Results

4.4.1. IRE parameter optimization

Parameters including number of pulses and frequency of pulses were designated according to previous literature[65, 133]. Application of PEF to KB cell monolayers treated with or without CNC-FA revealed a significant difference in cell viability for pulse lengths of 200 µs and 500 µs (Figure 4-1A). Initially, temperature was monitored with the fiber optic probe at the center of the sample between the electrodes. When starting at 37°C, treatment of cells with a pulse length of 500 µs produced an increase of medium temperature to above 42°C. Cells treated below 300 µs did not experience a significant increase in

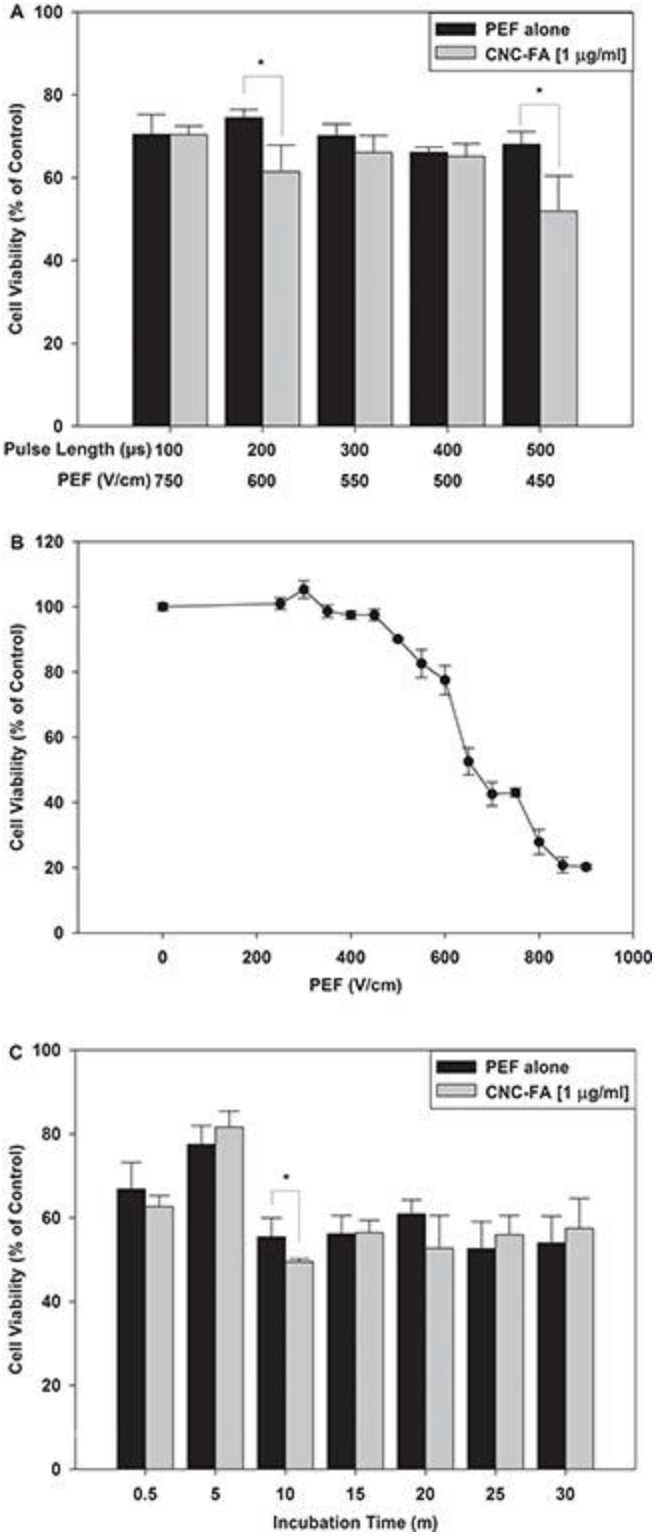

Figure 4-1: Parameter optimization for the potentiation of IRE-induced cytotoxicity with CNC-FA. KB cells were pre-treated with or without CNC-FA [1 µg/ml]. 80 pulses of the specified PEF were applied at a frequency of 1 Hz and cell viability was measured with CellTiter-Blue® Cell Viability Assay Kit. Parameters optimized include pulse length (A), PEF for targeted cell viability (B), and incubation time with CNC-FA (C). Data shown are mean ± SD for each group (n=4) (*$p<0.05$).

temperature and remained at or below 39°C. Therefore 200 µs was chosen as the optimal pulse length for all subsequent experiments. Figure 4-1B demonstrates that a PEF of 600 V/cm resulted in a desired cell viability of ~70% (about half way between maximum and minimum cell viability from IRE alone)[130]; while an incubation time of 10 min with CNC-FA caused a significant decrease in cell viability compared to IRE alone (Figure 4-1C). A cell viability of 70% from IRE alone is desirable to observe the maximum potentiation effect which can be seen in Table 4-1.

Table 4-1: Effects of CNC-FA on IRE-induced cytotoxicity in KB cells. Data shown are mean ± SD for each group (n=4).

	PEF‡ (V/cm)	0	250	450	600	700	850
CNC–FA§	0	100.0 ± 0.4	99.4 ± 0.6	93.5 ± 1.8 *	66.4 ± 2.7 *	36.0 ± 1.7 *	16.0 ± 3.5 *
	ng/ml 1	98.8 ± 1.3	97.5 ± 0.8 *†	96.4 ± 1.3 *†	60.3 ± 1.8 *†	37.8 ± 3.1 *	27.8 ± 3.0 *†
	ng/ml 10	98.3 ± 1.5	96.9 ± 1.6 *†	95.4 ± 1.1 *	51.5 ± 2.8 *†	35.6 ± 2.8 *	18.8 ± 1.1 *
	ng/ml 100	97.5 ± 1.7	96.8 ± 0.9 *†	95.8 ± 1.1 *	52.8 ± 3.7 *†	38.7 ± 3.2 *	22.2 ± 4.2 *
	µg/ml 1	99.6 ± 1.5	96.3 ± 1.2 *†	89.9 ± 2.8 *	56.0 ± 3.2 *†	30.1 ± 3.1 *†	14.8 ± 1.5 *
	µg/ml 10	100.2 ± 2.1	96.4 ± 2.0 *†	92.0 ± 2.5 *	57.0 ± 1.3 *†	34.5 ± 0.5 *	15.5 ± 1.3 *

*significant vs. control †significant vs. PEF alone ‡pulse electric field §cellulose nanocrystal–folic acid

4.4.2. CNC-FA potentiated IRE

Treatment of KB cells with various concentrations of CNC-FA prior to PEF application showed significantly higher cytotoxicity compared to IRE alone at a number of different PEFs. All concentrations of CNC-FA (1 ng/ml – 10 µg/ml) tested, significantly potentiated IRE (Table 4-1and Figure 4-2A). It was concluded that a concentration of 1 µg/ml is the best concentration tested to observe the potentiation effect across multiple PEFs in KB cells. In contrast, treatment of KB cells with non-targeted nanoparticles (CNC-COOH) at 1 µg/ml did not show any significant difference in cytotoxicity compared to IRE alone (Figure 4-2B). Furthermore, treatment of FR-negative cancer cells (A549) with CNC-FA, under the same conditions used for KB cells, also caused no significant increase in cytotoxicity (Figure 4-2C).

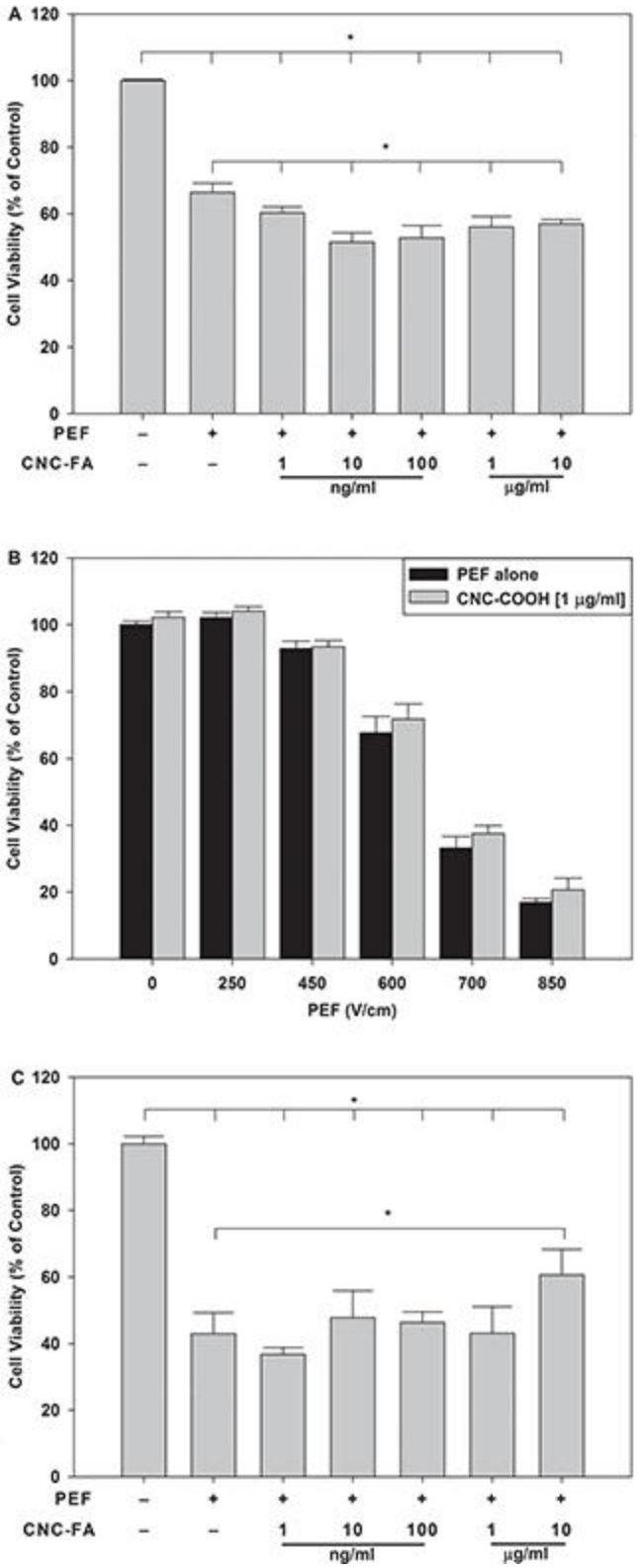

Figure 4-2: Effects of CNC-FA on cytotoxicity due to PEF induction. KB cells were pre-treated with various concentrations of CNC-FA for 10 min prior to PEF application. CellTiter-Blue® Cell Viability Assay Kit was used to measure viability of cells. A closer look at the PEF 600 V/cm (B) magnifies the significant potentiated effect of CNC-FA on IRE (A). KB cells were also pre-treated with non-targeted CNC-COOH [1 µg/ml] prior to PEF application of 600 V/cm (B). FR-negative lung cancer cells, A549 (C), were pre-treated with various concentrations of CNC-FA for 10 min prior to PEF application of 600 V/cm. Data shown are mean ± SD for each group (n=4) (*$p<0.05$).

FR-positive breast cancer cells, MDA-MB-468, further confirmed the results seen with KB cells. As shown in Figure 4-3A, the optimal PEF for this cell type was 500 V/cm to achieve ~70% cell viability. The largest increase in cytotoxicity due to CNC-FA was observed when nanoparticle incubation time was 20 min (data not shown). At 500 V/cm, all concentrations of CNC-FA (1 ng/ml – 10 µg/ml) tested exerted significant potentiation of cytotoxicity when compared to IRE alone (Figure 4-3B). It was concluded that a concentration of 1 and 10 µg/ml are the best concentrations tested to observe the potentiation effect in MDA-MB-468 cells.

4.4.3. Confocal microscopy

Confocal microscopy imaging determines that FITC-labeled CNC-FA particles are only binding to the cell membrane of KB and MDA-MB-468 cells after 10 and 20 min. respectively (Figure 4-4). There is not yet internalization of the particles as seen in Figure 4-4. Complete internalization by KB

and MDA-MB-468 cells has been observed after 1 h of exposure to FITC-CNC-FA particles (data not shown). Non-targeted entities (FITC and FITC-CNC) did not show any significant binding or uptake for exposure times up to 2 h (data not shown).

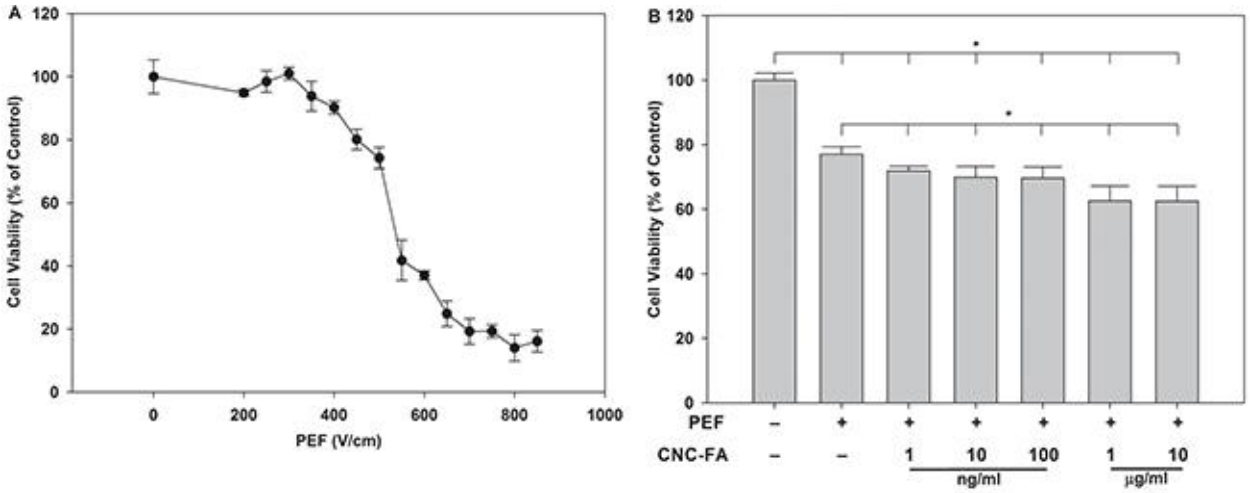

Figure 4-3: Effects of CNC-FA on IRE-induced cytotoxicity in FR-positive human breast cancer cells. Optimal PEF selection was based on application of various PEFs alone on MDA-MB-468 cell monolayers (A). MDA-MB-468 cells were pre-treated with various concentrations of CNC-FA for 20 min prior to PEF application of 500 V/cm (B). CellTiter-Blue® Cell Viability Assay Kit was used to measure viability of cells. Data shown are mean ± SD for each group (n=4) (*$p<0.05$).

4.4.4. Numerical modeling

The results from the finite element model of a clinical IRE scenario are shown in Figure 4-5. For illustrative purposes, it is assumed that the electric field threshold for cell death without CNC-FA is 600 V/cm in liver tissue[134], which is shown in gray. From the *in vitro* results, it was estimated that the greatest difference in electric field strength required to achieve a specific reduction in viability was 50 V/cm between the KB cells treated without CNC-FA and with CNC-FA at concentration of 10 ng/ml. Although 1 µg/ml of CNC-FA is considered the best concentration across multiple PEFs, at 600 V/cm it was observed that 10 ng/ml created the largest potentiation effect. This 50 V/cm reduction is shown on the tissue-scale model by the 550 V/cm contour, which is encompassed by the black region. These results suggest that upon *in vivo* translation, the inclusion of CNC-FA could expand the overall treatment volume from 3 cm^3 to 4 cm^3. Further, within the expanded treatment volume, only cancer cells with bound CNC-FA would be subject to IRE, and the healthy cells would be spared. This would be suitable for treating locally infiltrative disease extending up to 2 mm beyond the tumor margin.

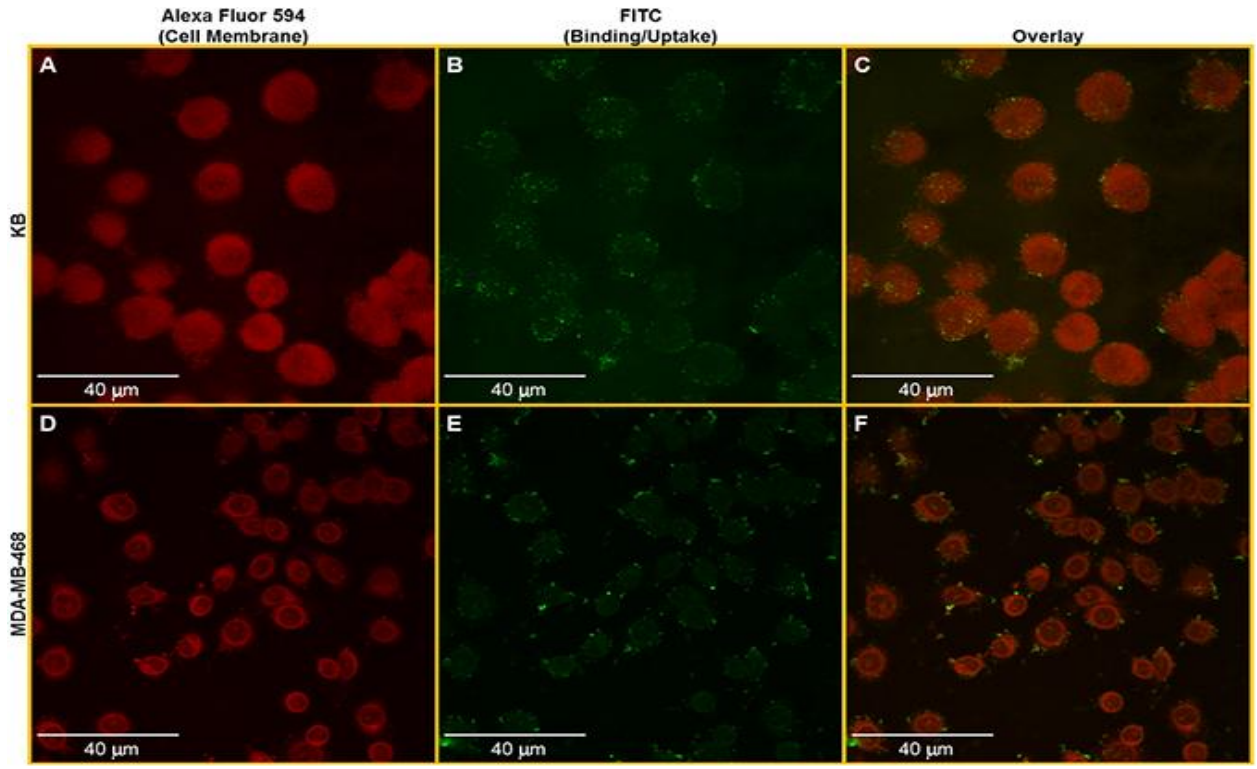

Figure 4-4: Representative confocal images of CNC-FA bound to KB and MDA-MB-468 cell membrane. KB (A-C) and MDA-MB-468 (D-F) cells were treated for 10 and 20 min, respectively, with FITC-CNC-FA, thoroughly washed with HBSS, and fixed in ethanol. Cell membranes were briefly stained with Concanavalin A Alexa Fluor® 633 and cells were imaged with a Zeiss LSM 510 confocal microscope. Image cross sections were taken from the bottom half of the cell at z=3.1 µm (KB) and z=8.1 µm (MDA-MB-468). Data shown are representative images for

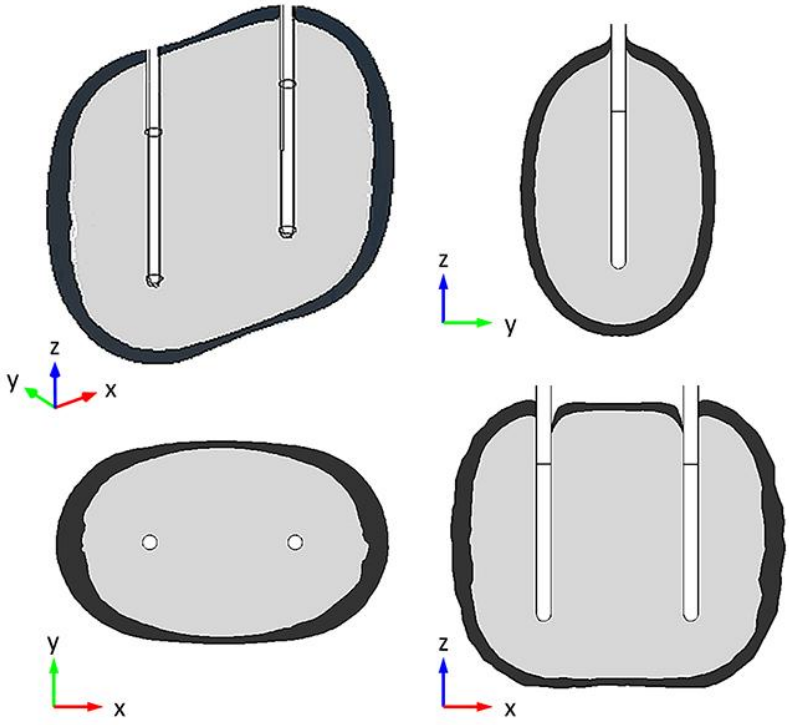

Figure 4-5: Results of the numerical model (4 orientations) for illustrating the potentiation of IRE-induced cytotoxicity with CNC-FA. The gray color represents regions of tissue exposed to an electric field threshold of 600 V/cm or greater that experience non-selective IRE. The black color represents regions of tissue exposed to an electric field between 550 V/cm and 600 V/cm that experience cancer cell-specific IRE with the inclusion of CNC-FA.

4.4.5. Discussion

The present study demonstrates the advantages of selectively enhancing electroporation-based therapies applied to cancer cell monolayers, *via* targeted nanoparticles. Without changing IRE parameters it is possible to increase the cytotoxic effect on FR-positive cancer cells while not causing further damage to healthy tissue (Figure 4-2 and Figure 4-3). In addition to providing a degree of selectivity to IRE, nanoparticles can reduce the required voltage to mitigate thermal effects[135] and muscle contractions[68]. As described in Raffa et al.[68], it is important to take note of the size of particles used for this purpose. BNNTs cytotoxicity depends on their aspect ratio and overall length; BNNTs over 10 µm can induce cytotoxicity to a variety of cell types on their own[68, 123]. Rod-like CNCs are similar in shape to BNNTs, however their aspect ratio is drastically smaller with an average length between 100 and 150 nm and an average width between 4.5 and 5 nm depending on the cellulose source and hydrolysis conditions[50]. It is possible to increase the aspect ratio of CNCs by decreasing the hydrolysis time, which may lead to larger potentiation effects. Care must be taken to see if larger aspect ratios of CNCs cause cytotoxicity.

The mechanism of nanoparticle potentiation of IRE-induced cytotoxicity was not investigated in this study. However, mechanistic theories of electroporation have been discussed for over thirty years with the most likely scenario being the production of nanoscale pores. Three cytotoxicity mechanisms induced from these pores have frequently been proposed. Nanoscale pores may significantly disrupt the cell's homeostasis inducing necrosis, cell contents may continuously leak out through long lasting pores, or reactive oxygen species may be generated in association with increased membrane permeability[128, 136-139]. In addition, the mechanism of how CNC-FA binds and is uptaken into FR-positive cell types has been studied (unpublished works). When CNC-FA binds to the FR on the plasma membrane, endocytosis is initiated. It may be that this process makes the plasma membrane more vulnerable to electroporation-induced pores and provokes necrosis with no changes to IRE parameters. The idea that membrane defects facilitate electroporation *via* water penetration is in agreement with molecular dynamics simulations[140]. Once the particles are endocytosed they most likely no longer have an effect on the plasma membrane. It is also noteworthy to mention studies by Habibi et al.[125] and Csoka et al.[124]. CNCs have been shown to align perpendicular to an applied electric field, which may cause insulative

behavior that would increase the electric field strength at the poles of the cell. This may also play a role in potentiation[124].

The up-regulation of FR expression has been reported in many types of cancers including breast, ovarian, lung, kidney, brain, and endometrium[23-28]. On the other hand, the FR is seldom expressed in normal tissues with the exceptions of the kidneys, placenta, and salivary gland[64, 84, 141]. Since FR overexpression is generally present in many cancer types, CNC-FA-mediated potentiation of cytotoxicity induced by IRE can be applied to multiple treatment regimes. Garcia et al.[56] conducted a form of IRE in canine patients diagnosed with intracranial malignant gliomas. To completely eradicate the cancer, adjuvant radiation therapy was added to the treatment regime; however, radiation therapy has serious and undesirable side effects. CNC-FA has the potential to replace or diminish the amount of radiation needed for complete remission.

Decreasing the amount of normal tissue being treated irreversibly with electroporation without decreasing the percentage of tumor being eradicated has vast clinical importance. An *in vivo* translational model is showcased in Figure 4-6. If this concept is fully translational, brain tumor patients, for example, would be able to have an inoperable tumor treated completely without the aid of radiation or traditional chemotherapy. Furthermore, harsh side effects associated with radiation and chemotherapy will not be experienced by the patient, improving their quality of life. According to the numerical model, lowering the IRE threshold by 50 V/cm would extend the treatment margin by 2 mm, allowing for a substantial volume of infiltrative diseased tissue to be treated without damaging the surrounding healthy cells. This 50 V/cm difference is based on experiments in 2D monolayers, and it is possible that the difference would be larger in 3D, possibly extending the zone of selective cell death.

Future work will include testing potentiation in a 3D mock tumor tissue. Arena et al.[131] recently published a high order *in vitro* model for designing and testing IRE protocols in more realistic tumor environments. A number of unknown parameters need to be optimized before animal models are subjected to testing; transport of CNC-FA through extracellular matrix remains unclear, as well as timing between nanoparticle introduction and PEF application. Electroporation in tissue is also much more complex. There have been studies in recent years successfully mapping the techniques and theory necessary, yet adding another layer such as nanoparticle potentiation may drastically change electroporation techniques for the better. This should be well investigated before *in vivo* testing begins.

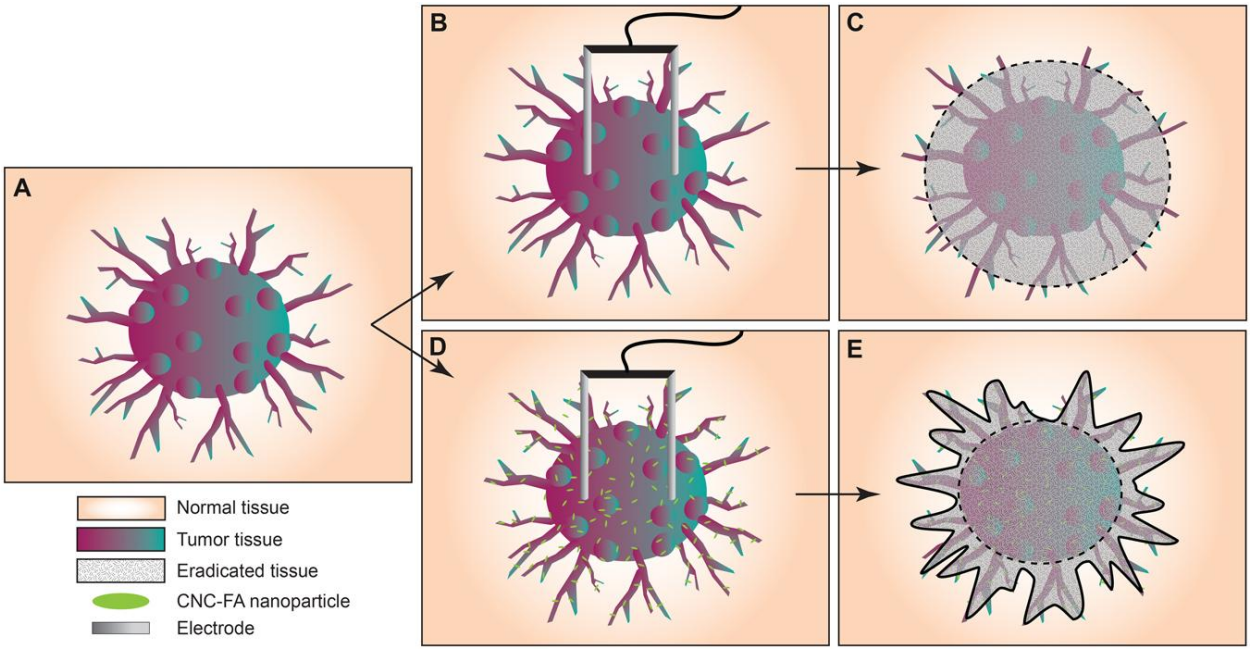

Figure 4-6: *In vivo* translational hypothesis. Tumors (A), treated with IRE alone (B), have a uniform distribution of irreversible electroporation regions (C). To treat the entire tumor you would have to design the IRE parameters to include a larger region including a substantial amount of normal tissue. Based on the results presented, if conjugated CNCs are introduced to the tumor before electroporation (D) we could decrease the PEF applied and would see a less uniform region of irreversible electroporation with a higher tumor to normal tissue ratio (E). The dotted lines (C, E) showcase the area treated by IRE alone, while the solid line (E) represents the additional treatment area seen by pre-treating with CNC-FA.

In conclusion, the data presented demonstrates that noncytotoxic CNC-FA is bound to the receptor on the cell membrane of FR-positive cancer cells and significantly increases the cytotoxic effect of IRE. From this we conclude that a lower PEF can be applied to tumor cells to achieve the same cytotoxicity when pre-treated with CNC-FA. Since these particles selectively bind to FR-positive cancer cells, it suggests that only FR-positive cells will see an increase in cytotoxicity. This would imply that the treated region would not have to be uniform in shape, sparing normal tissue.

4.5. Conflict of Interest

The authors of this manuscript do not have any conflicts of interest to disclose.

4.6. Acknowledgments

I would like to thank Joo Won Im and Hyung Joon Cho for their illustration expertise in creating Figure 4-6. This work was supported by the NSF (#DMR0907567 and #CBET093335) and the Institute for Critical Technology and Applied Science (ICTAS).

Chapter 5. Three Dimensional *in vitro* Tumor Model: Folic Acid Conjugated Cellulose Nanocrystals Binding and Uptake Ability to Folate Receptor Positive Cancer Cells

Katelyn R. Colacino[1], Alex Callo[2], Shuping Dong[3], Maren Roman[3], Yong Woo Lee[1, 4]

[1]School of Biomedical Engineering and Sciences, Virginia Tech-Wake Forest University, Blacksburg, VA

[2]Department of Biology and Biochemistry, Virginia Tech, Blacksburg, VA

[3]Macromolecules and Interfaces Institute and Department of Sustainable Biomaterials, Virginia Tech, Blacksburg, VA

[4]Department of Biomedical Sciences and Pathobiology, Virginia-Maryland Regional College of Veterinary Medicine, Virginia Tech, Blacksburg, VA

Preliminary data.

5.1. Abstract

To develop new delivery systems and strategies, scientists turn to 2D *in vitro* and small animal models for testing. The differences between these two stages are vast and an intermediate step is available. Collagen I hydrogels present realistic mechanical properties in a 3D *in vitro* setting, allowing for more accurate cell-cell and cell-extracellular matrix interactions. In this study, we tailored an established hydrogel model for future investigations of fluorescently labeled, folate conjugated cellulose nanocrystals (FITC-CNC-FA) ability to potentiate irreversible electroporation. Parameters including hydrogel thickness, seeding cell density, cell incubation time, and FITC-CNC-FA diffusion characteristics were investigated. This model can more accurately predict FITC-CNC-FA and IRE effects *in vivo*, as compared with a 2D system.

5.2. Introduction

The most common way cancer research is conducted *in vitro*, is within two-dimensional (2D) cell systems (Petri dishes, glass slides, and well plates to name a few). For a group studying the effects of a novel therapeutic on cancer progression, the natural progression after successful *in vitro* experimentation, is the use of small animal models. As a result of the vast differences in microenvironment, protein expression and cell-extracellular matrix (ECM) interactions, there are quite a few iterations between *in vivo* experimentation and tweaking of the original therapeutic system. This can be avoided with the use of three-dimensional (3D) *in vitro* tumor models. Though no one system has become the gold standard in this application, Szot et al.[142] have shown great progression in the development of a 3D *in vitro* tumor model. They use type I collagen to create hydrogels as effective biomimetic scaffolds for tumor growth and proliferation. Collagen I hydrogels accessibility, biocompatibility, and non-toxicity render them appropriate representations of the tumor extracellular matrix[143]. In addition to their compatibility with cancer cells, collagen hydrogels also accurately depict the pre-vascularized tumor matrix with regards to stiffness, structure, and remodeling potential, leading to proliferation, migration, and infiltration[144]. Furthermore, there are many factors of small animal models that cannot be as easily controlled as *in vitro*. The combination of improved cell-cell and cell-ECM interactions seen in hydrogel models, showcases their valuable nature as an effective intermediate step between 2D experimentation, and small animal models, saving time, mice, and money[142].

Though the mechanism of IRE induced cytotoxicity is not clearly understood, it is widely believed excessive amounts of nanopores are formed in the cell membrane due the changes in cell membrane potential (Figure 1-7), from which homeostasis is no longer balanced and the cell cannot recover from the damage. If the electric field is weaker, cells can undergo reversible electroporation in which the amount of nanopores is few enough to ensure recovery of homeostasis. When examining IRE in a 2D model vs. 3D, the properties and parameters change drastically[131]. Though IRE parameter translations can be made between the two systems through mathematical modeling, the effects on cells cannot be accurately predicted and need to be tested before continuing into animal models.

The folate receptor (FR) is well known to be overexpressed in various cancer cell lines, helping to contribute to the cells' rapid growth. When compared to healthy tissue, as seen in Chapter 2, cancer cells can exhibit up 8×10^6 fold higher FR expression levels. More specifically,

the FR has a great affinity for the folic acid (FA); and when attached to cellulose nanocrystals (CNCs) as carriers, selectively bind and become endocytosed by FR-positive cancer cells (Chapter 2, Figure 5-1). CNCs have been shown to align perpendicular to an applied electric field, which may cause a stronger insulative behavior that would increase the electric field strength at the poles of the cell; which may also play a role in potentiation[124]. Capitalizing on this information, renders folate-conjugated particles as attractive vehicles for targeted cancer treatment. The aim of this study is to tailor a 3D *in vitro* hydrogel model for continued investigation of CNC-FA's ability to potentiate IRE-induced cytotoxicity (Chapter 4). Hydrogel and cell seeding parameters were examined along with the permeation time of fluorescein-5'-isothiocyanate labeled CNC-FA (FITC-CNC-FA) within a cell seeded hydrogel. Fruits of this study will further be used to evaluate IRE parameters for optimal potentiation with CNC-FAs.

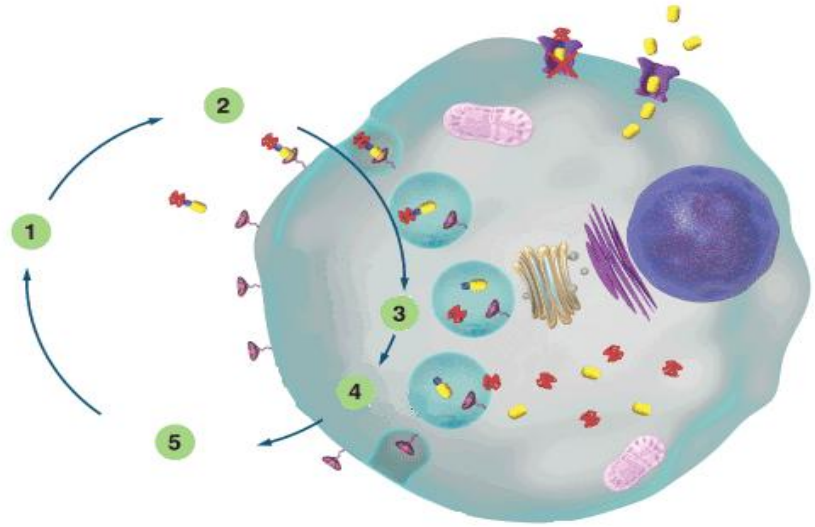

Figure 5-1: Endocytosis process of folate linked particle. (1) Folate linked particle is introduced into the tumor microenvironment. (2) Particle binds to the folate receptor and initiates endocytosis. (3) Particle breaks from folate receptor. Linked material is cleaved from folate or carrier. (4) Material becomes active within the cell. (5) Receptor is recycled back to the membrane. Modified with permission from Endocyte Inc.

5.3. Materials and Methods

5.3.1. Materials

Dissolving-grade softwood sulfite pulp (Temalfa 93A-A) was kindly provided by Tembec, Inc. (Montréal, QC, CA). FITC, FA, and Dulbecco's Modified Eagle Medium were purchased from Sigma-Aldrich Corporation (St. Louis, MO, USA). Folate-free RPMI 1640 medium, goat anti-rabbit Alexa Fluor® 555 (21429) secondary antibody, and Concanavalin A Alexa Fluor® 594 and 633 conjugates were purchased from Invitrogen Corp. (Carlsbad, CA, USA). Rabbit cleaved caspase-3 primary antibody was purchased from Cell Signaling (Danvers, MA, USA). Antibiotics (penicillin and streptomycin) and fetal bovine serum (FBS) were purchased from

Mediatech, Inc. (Manassas, VA, USA). Spectra/Por dialysis tubes were purchased from Spectrum Lans (Rancho Dominguez, CA, USA). The human cancer cell line, MDA-MB-468, was purchased from American Type Culture Collection (Manassas, VA, USA). ProLong® Gold Antifade Reagent with DAPI was purchased from Life Technologies (Carlsbad, CA, USA). Rat collagen type I was kindly donated from Dr. Rafael Davalos's lab (Blacksburg, VA, USA). Remaining reagents and supplies were purchased from Fisher Scientific (Pittsburgh, PA, USA).

5.3.2. Synthesis of FITC-CNC-FA

The same procedures were used as described in Chapter 2. Briefly, CNC suspension was prepared using sulfuric acid hydrolysis, dialyzed against deionized water, and brought to a neutral pH, using bleached softwood pulp. The resulting suspension was sonicated using an ultrasonic processor (Model VC505) once at 200 Watts for 10 min, then centrifuged at 4,550 × *g* for 10 min to remove large particles. Hydroxyl groups on the CNC surface were converted to carboxyl groups for moiety conjugation. FITC was first conjugated to the CNC surface followed by FA. The reaction scheme can be seen in Figure 2-1. Characterization of particles can be seen in Table 2-1

5.3.3. Cell culture

MDA-MB-468 cells were grown in folate free-RPMI 1640 supplemented with 10% FBS and containing 100 IU/ml penicillin and 100 µg/ml streptomycin. Cells were grown at 37ºC and 5% CO_2. All experiments were conducted in folate free-RPMI 1640 basal medium.

5.3.4. Collagen I hydrogels

Collagen I hydrogel-based *in vitro* tumor models were developed as described previously[142]. Briefly, Sprague Dawley rat tail tendons were dissolved in 10 mM HCl under agitation overnight, the suspension was centrifuged at 22,500 × *g* for 45 min, and the supernatant containing the collagen I was decanted. The concentration of the collagen I solution was calculated using dry-weight measurements, and the solution was sterilized by layering chloroform beneath the collagen I for 24 h. A neutralizing

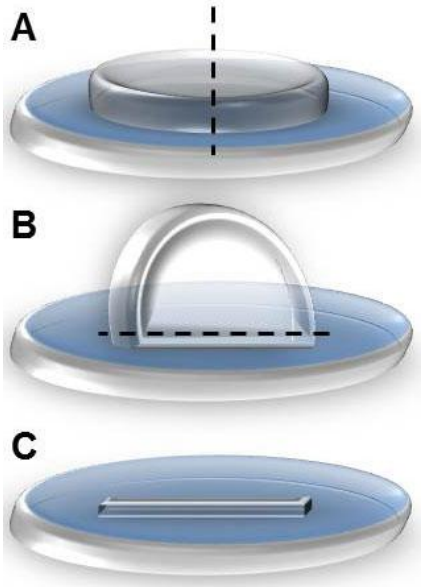

Figure 5-2: Hydrogel orientation for tissue sectioning. (A) Intact hydrogel cut in half to reveal cross section. (B) hydrogel stood up on cross section and before paraffin embedding. (C) 10 µm slice used in imaging analysis.

buffer containing 10× DMEM, 1 M NaOH, and distilled water was used to resuspend a pellet of MDA-MB468 cells. The cell suspension was then gently mixed on ice with an appropriate volume of collagen I to achieve a concentration of 8 mg/ml. This concentration supplies a matrix stiffness similar to those found in *in vivo* tumors[145]. The suspension was pipetted into 10 mm diameter cylindrical molds and allowed to set for a 20 min polymerization period at 37°C. The molds were removed, and the hydrogels were cultured in growth media until experimentation. Following experimentation, hydrogels were fixed and embedded in paraffin, sectioned, and prepared as described previously[142]. Figure 5-2 describes the orientation of tissue section slices.

5.3.5. Fluorescence microscopy

Paraffin hydrogel slices were fixed to glass slides before the removal of paraffin with xylene. For cell membrane staining, hydrogel sections were incubated with 50 ng/µl of Concanavalin A Alexa Fluor® 594 for 2 min and washed with PBS. Staining for apoptosis was performed by permeabilizing with 0.5% Triton X-100, blocking with 3% bovine serum albumin, and incubating with cleaved caspase-3 primary antibody (1:100 dilution) and Alexa Fluor® 555 secondary antibody (1:200 dilution), according to manufacturer's suggestions. Before imaging, sections were mounted with ProLong® Gold Antifade Reagent with DAPI. Images were obtained with a Leica AF6000 fluorescent microscope (Leica Microsystems Inc., Buffalo Grove, IL, USA).

5.3.6. Hydrogel parameter optimization

Parameters optimized included hydrogel thickness, cell density, and cell incubation time. To optimize hydrogel thickness, the diameter of each hydrogel was fixed to 10 mm and four volumes were tested: 150, 185, 200, and 235 µl, corresponding to heights of 1.91, 2.36, 2.55, and 3.00 mm respectively, and incubated for 3 days prior to fixation. To limit cell death before experimentation, three cell densities were tested; 5, 10, and 20 million cells/ml were incubated in hydrogels for 1 day. To achieve a confluent cell density of living cells within the hydrogels, incubation period with cells prior to experimentation was also investigated. 200 µl hydrogel solutions were prepared and incubated for 1, 2, and 3 days at a cell density of 1×10^6 cells/ml prior to fixation. Lastly, MDA-MB-468 containing hydrogels were treated with 10 µg/ml of FITC-CNC-FA (suspended in folate-free RPMI basal medium) and incubated varying amounts of time. The total incubation time between cell seeding and hydrogel fixation was 3 days.

5.4. Preliminary Results

5.4.1. Hydrogel height

Four hydrogel heights were investigated ranging from 1.91 mm to 3 mm. The shortest hydrogels did not polymerize well and were too fragile to be analyzed further. When comparing the remaining height variations, the 2.55 mm hydrogel was the thickest while being able to preserve cell density across the entire hydrogel. In the 3 mm hydrogel, cells were seen to migrate to the top of the hydrogel with more frequency creating an inner layer of hydrogel with little to no viable cells (data not shown).

5.4.2. Hydrogel cell seeding conditions

Moving forward, three cell density seeding conditions were tested; 5×10^6, 10×10^6, and 20×10^6 cell/ml. As seen in Figure 5-3 after 1 day of incubation, the highest cell density showed drastically higher cleaved caspase-3 expression, equating to lower cell viability. The lowest and middle cell densities showed very similar cell viability, yet the middle cell density logically demonstrates a higher amount of cells per hydrogel. Therefore we concluded that 10×10^6 cells/ml was a suitable density for further experimentation.

After cell seeding, cell-cell communications and cell-ECM interactions are desired. For this to occur, cells need to freely migrate and display elongated morphologies; extending the amount of incubation time gives them this opportunity[146]. Comparing the one-to-three day incubation time, we observed little differences in the cell viability, yet saw an increase in cell number and noticed cells migrating toward the surfaces of the hydrogel to gain access to more nutrients (data not shown).

5.4.3. FITC-CNC-FA permeation and binding

Now that we have a more optimized 3D model for our MDA-MB-468 cells, we can test permeation of FITC-CNC-FA nanoparticles in the cell seeded hydrogel. 2.55 mm tall, cell seeded hydrogels were incubated for 3 days with 10×10^6 cells/ml. Growth medium was replaced with basal medium containing 10 µg/ml FITC concentration of FITC-CNC-FA at seven different time points; 20 and 40 min, 1, 2, 4, 8, and 24 h prior to the end of the 3 day cell incubation period. Diffusion of FITC-CNC-FA after 4 h reached a steady state; looking at Figure 5-4, we can determine that full diffusion of FITC-CNC-FA occurs between the 40 min and 1 h mark. According to Chapter 4, the ideal pairing of nanoparticles and IRE to reach maximum

potentiation effects is when the nanoparticles first initiate endocytosis. Adding in IRE, would best be suited between the 40 and 60 min mark because of this.

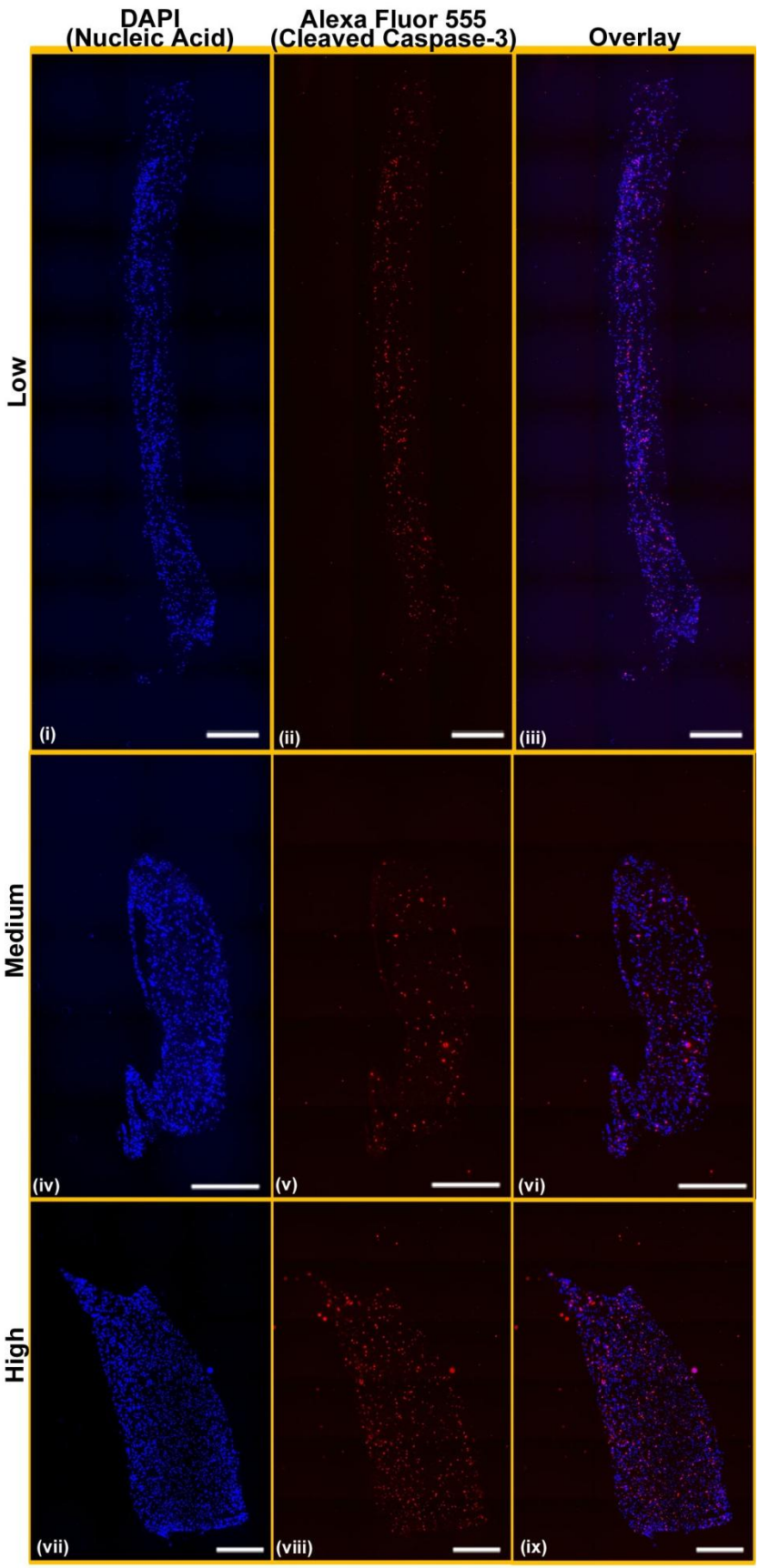

Figure 5-3: Hydrogels seeded with various initial cell densities. Hydrogels were seeded with MDA-MB-468 breast cancer cells for 24 h at the following densities: 5×10^6 (i, ii, iii), 10×10^6 (iv, v, vi), and 20×10^6 (vii, viii, ix) cells/ml. Hydrogels were stained for DAPI (i, iv, vii), to show nucleic acids, and Alexa Fluor® 555 (ii, v, viii), to show cleaved caspase-3 protein staining. The third column (iii, vi, ix) shows an overlay of the two channels. (Bar: 750 µm)

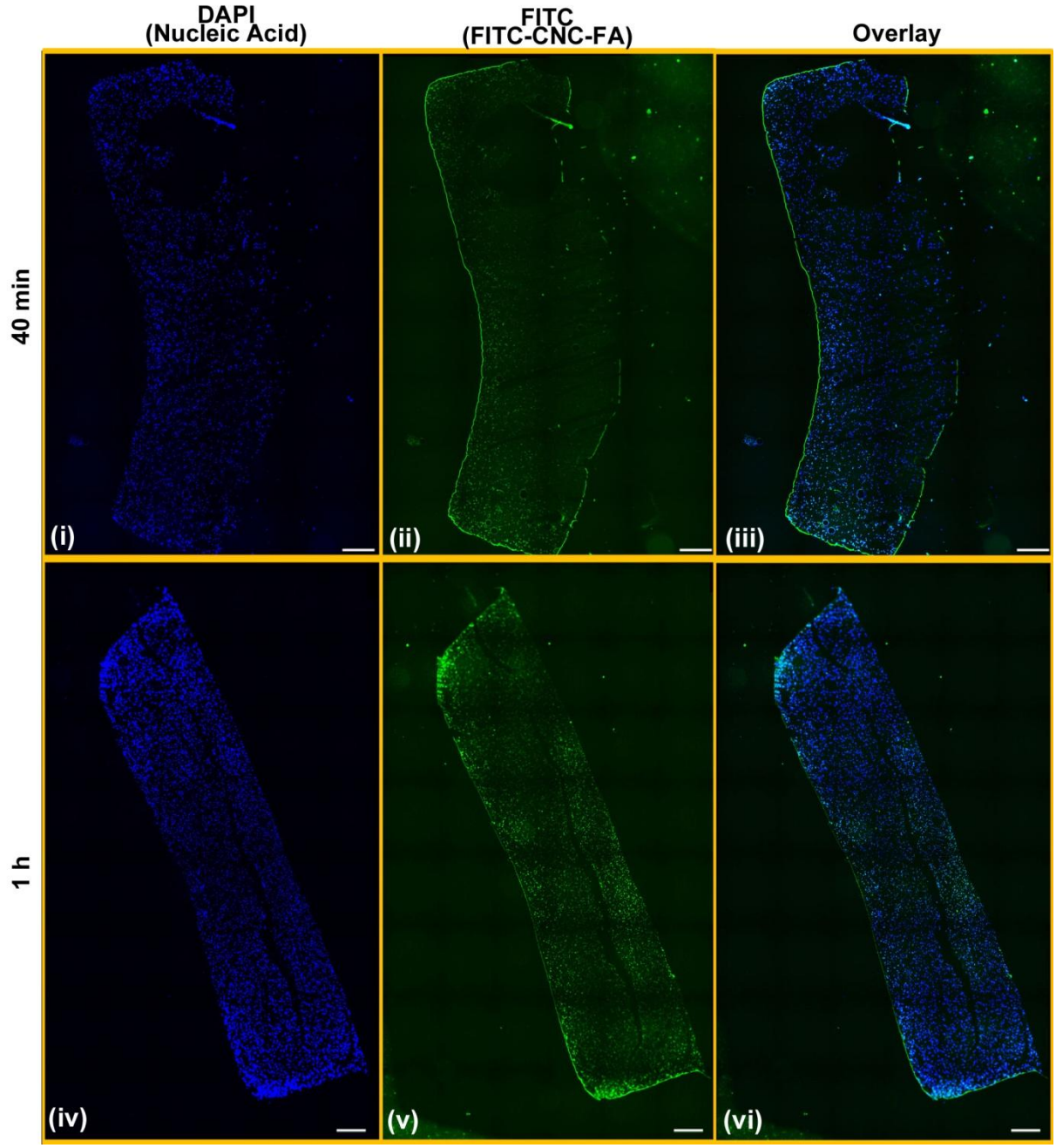

Figure 5-4: Hydrogels seeded with various initial cell densities. Hydrogels were seeded with MDA-MB-468 breast cancer cells for 3 days. FITC-CNC-FA was added at 40 min (i-iii) and 1 h (iv-vi), prior to being fixed. Hydrogels were stained for DAPI (i, iv, vii), to show nucleic acids. FITC (ii, v, viii) shows CNC conjugate binding/diffusion in hydrogel. The third column (iii, vi, ix) shows an overlay of the two channels. (Bar: 500 µm)

5.5. Discussion

Much of this work has been qualitative to this point and there are many aspects of 3D modeling we did not investigate. Countless groups dedicate their research to making 3D models the new gold standard for simulating *in vivo* studies[142]. They focus on design, stiffness, and structure of ECM materials, monitor the cell-cell and cell-ECM interactions by analyzing gene and protein expression, and compare cell phenotypes between the *in vitro* and *in vivo* models[147-149]. These aspects are pivotal to understanding the model that you are using and accurately describe the interactions between cells and varying stimuli (novel drug molecules, carriers, or angiogenesis). The intent of this study was to tailor the 3D hydrogel model to MDA-MB-468 breast cancer cells for future use in irreversible electroporation (IRE) and CNC-FA studies. The results from this study provide insight into the basic design, but since each experiment included groups of n=1, no statistical analysis could be completed, as well as a determination of significance.

Future experiments involving this model, involve a continuation of Chapter 4. In Figure 4-6, we propose an *in vivo* translation of the experiments conducted in 2D. To investigate this hypothesis, 3D hydrogels will be used to observe the CNC-FA potentiation effects of IRE-induced cytotoxicity. From Chapter 4 above, we observed these effects at optimal parameters. As previously stated, IRE effects are drastically different from a 2D to a 3D approach. Depending on the material, the amount of voltage needed to induce the same effect in 3D is much higher than in 2D[131]. Combining the results from this study and the previous one, we hope to observe the same effects in hydrogels so we can continue experimentation *in vivo*.

Described previously (Chapter 4), the ultimate goal is to marry the timing of initiation of CNC-FA endocytosis and the start of IRE. Particle size and shape greatly influence receptor mediated endocytosis[4, 68]. As a troubleshooting mechanism, the aspect ratio of the CNC conjugate can be increased or decreased by adjusting the exposure time of cellulose to the sulfuric acid hydrolysis procedure or by changing the source of cellulose (bacterial or tunicin cellulose). Larger aspect ratio particles may increase the potentiation effects due to the higher difficulty of the cell to endocytose completely (Figure 1-5). We could capitalize on the point where CNC-FA binds to the cell membrane by increasing the time before being entirely taken in or released[4].

5.6. Acknowledgements

This work was supported by Virginia Tech's Institute for Critical Technology and Applied Science (ICTAS) and the National Science Foundation (DMR0907567). We would like to extend special thanks to Katherine Prokop for isolating the collagen.

Chapter 6. Conclusions and Future Work

6.1. Summary and Conclusions

The literature is full of studies trying to discover the magic bullet for cancer therapy all of which have advantages and disadvantages. While there are many nano-carriers being studied, only one other group has published studies using CNCs as carriers[150]. We have demonstrated development of stable and reproducible CNCs with multiple conjugations for use in cancer detection and treatment. Furthermore we have shown potentiating effect of CNC conjugates on cytotoxicity induced by IRE. Since cellulose nanocrystals are so versatile and abundant in nature, avenues of its potential are endless.

In "Cellulose Nanocrystals Conjugated with Folic Acid Selectively Target Folate Receptor Positive Cancer Cells" we examined the modification of CNCs and its transformation into a targeting molecule for imaging and chemotherapeutic delivery. Specifically, CNCs are rod-shaped nanocrystals with a diameter of about 4-5 nm and an average length between 100-150 nm. Their surface is abundant with hydroxyl groups, which were converted to amine and carboxyl groups for the conjugation of FITC, DOX-ALAL, and FA.

We continued these studies in "Pharmacokinetic Analysis of Cellulose Nanocrystals Conjugated with Folic Acid for use in Selectively Targeting Folate Receptor Positive Tumors." According to this study, pharmacokinetic analysis demonstrates that FITC-CNC-FA show little to no apparent toxicity in tumor bearing nude mice and non-tumor bearing BALB/c mice. Furthermore, these nanoparticles were imaged non-invasively in live mice aggregating at the xenografted tumor site. Lastly, a PBPK model was developed that accurately depicts the life cycle of FITC-CNC-FA particles and settling properties in the body. Though, further work needs to be completed for a full understanding of how these particles interact with the body, this study shows promise in FITC-CNC-FA's ability in the early detection of FR-positive cancer.

For Chapter 4, "Folate-Attached Cellulose Nanocrystals Potentiate Irreversible Electroporation-Induced Cytotoxicity in Cancer Cells," CNC-FAs were investigated for their abilities to potentiate IRE-induced cytotoxic effects. We optimized the IRE parameters *in vitro* to maximize the potentiation effect and compared cells treated with IRE alone with CNC-FA + IRE. For FR-positive KB and MDA-MB-468 cancer cells, we observed a dose and time-

dependent increase in CNC-FA potentiated IRE-induced cytotoxicity, while no significant difference was observed in FR-negative A549 cells or with untargeted CNCs (CNC-COOH).

Lastly, in Chapter 5, "Three Dimensional *in vitro* Tumor Model: Folic Acid Conjugated Cellulose Nanocrystals Binding and Uptake Ability to Folate Receptor Positive Cancer Cells," we developed an *in vitro* experimental model to further examine effects of CNC-FA on IRE-induced cytotoxicity in a 3D hydrogel environment. We optimized hydrogel thickness, cell seeding density, and cell incubation time to achieve a more realistic *in vitro* tumor model. Furthermore we tested the permeation time of FITC-CNC-FA within the hydrogel. These preliminary studies can increase our understanding of the potentiation effect of CNC-FA on IRE-induced cytotoxicity, while sparing time and money before going further into small animal models.

6.2. Future Directions

6.2.1. DOX-ALAL-CNC-FA *in vivo*

After completion of FITC-CNC-FA *in vivo* analysis, attention can be turned to DOX-ALAL-CNC-FA characteristics *in vivo*. Pharmacokinetic investigation can be conducted in the same manner as FITC-CNC-FA. Due to DOX's inherent cardiotoxicity, these CNC conjugates will have to be monitored more closely for side effects and toxicity. In tumor bearing mice DOX-ALAL-CNC-FA's efficacy in treating FR-positive cancer can be compared to free DOX dosing regimens. The main hypothesis to be tested is "DOX-ALA-CNC-FA effectively reduce FR-positive tumor size with significantly less side effects when compared to free DOX." Our PBPK model can be slightly modified to handle multiple drug bolus injections and increasing/decreasing tumor volumes. This work has the potential to yield scientifically and translationally significant data to be used in future clinical trials.

6.2.2. CNC-FA + IRE investigations in a 3D hydrogel *in vitro* model

Chapter 5 sets the stage for CNC-FA's potentiation of IRE-induced cytotoxicity in a 3D setting. To continue this study, IRE parameters will be further translated into a 3D environment. Cells will be seeded into hydrogels and pre-treated with fluorescently labeled CNC-FA prior to IRE treatment. LIVE/DEAD assays and confocal microscopy will elucidate the changes in treatment region between FR-positive and FR-negative cell types. Furthermore a co-culture of

FR-positive and FR-negative cells can be tested in the same fashion. This study will enhance results seen in Chapter 4 and confirm or reject the hypothesis stated in Figure 4-6.

6.2.3. Multistage nanoparticles

Nanoparticle delivery occurs in stages and for optimization purposes should be broken up into these stages rather than lumped together. For instance, parameters such as evading the immune system and increasing circulation time vary from optimal parameters for cellular uptake. Decuzzi et al.[9, 11, 14, 114, 151], describe the synthesis of multistage nanoparticles to cater to these issues. They have created a two stage system which enables a more personalized targeting strategy. Firstly they create nanoparticles that are optimized in size and shape solely for cellular uptake by cancer cells. Next they encapsulate these particles within a disk-like silica microparticles constructed solely to evade filtration and increase time circulation. These microparticles are designed to trigger release of the nanoparticles when in the presence of diseased vasculature as seen in the cancer microenvironment. This type of tailored drug delivery can be modified for CNC delivery as well, increasing efficacy and efficiency of our nanoparticle system.

Chapter 7. References

(1) Taurin, S.; Nehoff, H.; Greish, K. Anticancer nanomedicine and tumor vascular permeability; where is the missing link? *J. Controlled Release* **2012,** *164*, 265-75.

(2) Hanahan, D.; Weinberg, R. A. Hallmarks of cancer: the next generation. *Cell* **2011,** *144*, 646-74.

(3) Kritzer, J. A. Stapled peptides: Magic bullets in nature's arsenal. *Nat. Chem. Biol.* **2010,** *6*, 566-7.

(4) Decuzzi, P.; Pasqualini, R.; Arap, W.; Ferrari, M. Intravascular delivery of particulate systems: Does geometry really matter? *Pharm. Res.* **2009,** *26*, 235-43.

(5) Wang, S.; Low, P. S. Folate-mediated targeting of antineoplastic drugs, imaging agents, and nucleic acids to cancer cells. *J. Controlled Release* **1998,** *53*, 39-48.

(6) American Cancer Society. Cancer facts and figures 2013. Atlanta: American Cancer Society; **2013**.

(7) National Cancer Institute. National cancer program: An annual plan and budget proposal for fy 2013. **2012**.

(8) Cheng, Z.; Al Zaki, A.; Hui, J. Z.; Muzykantov, V. R.; Tsourkas, A. Multifunctional nanoparticles: Cost versus benefit of adding targeting and imaging capabilities. *Science* **2012,** *338*, 903-10.

(9) Lee, S. Y.; Ferrari, M.; Decuzzi, P. Shaping nano-/micro-particles for enhanced vascular interaction in laminar flows. *Nanotechnology* **2009,** *20*, 495101.

(10) Godin, B.; Driessen, W. H.; Proneth, B.; Lee, S. Y.; Srinivasan, S.; Rumbaut, R.; Arap, W.; Pasqualini, R.; Ferrari, M.; Decuzzi, P. An integrated approach for the rational design of nanovectors for biomedical imaging and therapy. *Adv. Genet.* **2010,** *69*, 31-64.

(11) Decuzzi, P.; Godin, B.; Tanaka, T.; Lee, S. Y.; Chiappini, C.; Liu, X.; Ferrari, M. Size and shape effects in the biodistribution of intravascularly injected particles. *J. Controlled Release* **2010,** *141*, 320-7.

(12) Decuzzi, P.; Ferrari, M. Design maps for nanoparticles targeting the diseased microvasculature. *Biomaterials* **2008,** *29*, 377-84.

(13) Boso, D. P.; Lee, S. Y.; Ferrari, M.; Schrefler, B. A.; Decuzzi, P. Optimizing particle size for targeting diseased microvasculature: From experiments to artificial neural networks. *Int. J. Nanomed.* **2011,** *6*, 1517-26.

(14) Adriani, G.; de Tullio, M. D.; Ferrari, M.; Hussain, F.; Pascazio, G.; Liu, X.; Decuzzi, P. The preferential targeting of the diseased microvasculature by disk-like particles. *Biomaterials* **2012,** *33*, 5504-13.

(15) Love, R. R.; Leventhal, H.; Easterling, D. V.; Nerenz, D. R. Side-effects and emotional distress during cancer-chemotherapy. *Cancer* **1989,** *63*, 604-12.

(16) National Cancer Institute. Comprehensive cancer information. **2013**.

(17) Gabizon, A.; Shiota, R.; Papahadjopoulos, D. Pharmacokinetics and tissue distribution of doxorubicin encapsulated in stable liposomes with long circulation times. *J. Natl. Cancer Inst.* **1989,** *81*, 1484-8.

(18) Hagtvet, E.; Evjen, T. J.; Nilssen, E. A.; Olsen, D. R. Assessment of liposome biodistribution by non-invasive optical imaging: a feasibility study in tumour-bearing mice. *J. Nanosci. Nanotechnol.* **2012,** *12*, 2912-8.

(19) Hantel, C.; Lewrick, F.; Reincke, M.; Suss, R.; Beuschlein, F. Liposomal doxorubicin-based treatment in a preclinical model of adrenocortical carcinoma. *J. Endocrinol.* **2012,** *213*, 155-61.
(20) Tredan, O.; Galmarini, C. M.; Patel, K.; Tannock, I. F. Drug resistance and the solid tumor microenvironment. *J. Natl. Cancer Inst.* **2007,** *99*, 1441-54.
(21) Maeda, H.; Wu, J.; Sawa, T.; Matsumura, Y.; Hori, K. Tumor vascular permeability and the epr effect in macromolecular therapeutics: a review. *J. Controlled Release* **2000,** *65*, 271-84.
(22) Maeda, H. Macromolecular therapeutics in cancer treatment: the epr effect and beyond. *J. Controlled Release* **2012,** *164*, 138-44.
(23) Dainty, L. A.; Risinger, J. I.; Morrison, C.; Chandramouli, G. V.; Bidus, M. A.; Zahn, C.; Rose, G. S.; Fowler, J.; Berchuck, A.; Maxwell, G. L. Overexpression of folate binding protein and mesothelin are associated with uterine serous carcinoma. *Gynecol. Oncol.* **2007,** *105*, 563-70.
(24) Hartmann, L. C.; Keeney, G. L.; Lingle, W. L.; Christianson, T. J. H.; Varghese, B.; Hillman, D.; Oberg, A. L.; Low, P. S. Folate receptor overexpression is associated with poor outcome in breast cancer. *Int. J. Cancer* **2007,** *121*, 938-42.
(25) Toffoli, G.; Cernigoi, C.; Russo, A.; Gallo, A.; Bagnoli, M.; Boiocchi, M. Overexpression of folate binding protein in ovarian cancers. *Int. J. Cancer* **1997,** *74*, 193-8.
(26) Weitman, S. D.; Frazier, K. M.; Kamen, B. A. The folate receptor in central nervous system malignancies of childhood. *J. Neurooncol.* **1994,** *21*, 107-12.
(27) Weitman, S. D.; Weinberg, A. G.; Coney, L. R.; Zurawski, V. R.; Jennings, D. S.; Kamen, B. A. Cellular localization of the folate receptor: Potential role in drug toxicity and folate homeostasis. *Cancer Res.* **1992,** *52*, 6708-11.
(28) Weitman, S. D.; Lark, R. H.; Coney, L. R.; Fort, D. W.; Frasca, V.; Zurawski, V. R., Jr.; Kamen, B. A. Distribution of the folate receptor GP38 in normal and malignant cell lines and tissues. *Cancer Res.* **1992,** *52*, 3396-401.
(29) Parker, N.; Turk, M. J.; Westrick, E.; Lewis, J. D.; Low, P. S.; Leamon, C. P. Folate receptor expression in carcinomas and normal tissues determined by a quantitative radioligand binding assay. *Anal. Biochem.* **2005,** *338*, 284-93.
(30) Yang, J.; Chen, H. T.; Vlahov, I. R.; Cheng, J. X.; Low, P. S. Characterization of the pH of folate receptor-containing endosomes and the rate of hydrolysis of internalized acid-labile folate-drug conjugates. *J. Pharmacol. Exp. Ther.* **2007,** *321*, 462-8.
(31) Tan, S. Y.; Grimes, S. Paul ehrlich (1854-1915): Man with the magic bullet. *Singapore Med. J.* **2010,** *51*, 842-3.
(32) Dong, S.; Hirani, A.; Colacino, K. R.; Lee, Y. W.; Roman, M. Cytotoxicity and cellular uptake of cellulose nanocrystals. *Nano LIFE* **2012,** *2*, 1241006-1.
(33) Zhang, L.; Gu, F. X.; Chan, J. M.; Wang, A. Z.; Langer, R. S.; Farokhzad, O. C. Nanoparticles in medicine: Therapeutic applications and developments. *Clin. Pharmacol. Ther.* **2008,** *83*, 761-9.
(34) Ji, Z.; Lin, G.; Lu, Q.; Meng, L.; Shen, X.; Dong, L.; Fu, C.; Zhang, X. Targeted therapy of smmc-7721 liver cancer in vitro and in vivo with carbon nanotubes based drug delivery system. *J. Colloid Interface Sci.* **2012,** *365*, 143-9.
(35) Lacerda, L.; Bianco, A.; Prato, M.; Kostarelos, K. Carbon nanotubes as nanomedicines: From toxicology to pharmacology. *Adv. Drug Del. Rev.* **2006,** *58*, 1460-70.

(36) Sarkar, S.; Zimmermann, K.; Leng, W.; Vikesland, P.; Zhang, J.; Dorn, H.; Diller, T.; Rylander, C.; Rylander, M. N. Measurement of the thermal conductivity of carbon nanotube--tissue phantom composites with the hot wire probe method. *Ann. Biomed. Eng.* **2011,** *39*, 1745-58.
(37) Gabizon, A. A.; Shmeeda, H.; Zalipsky, S. Pros and cons of the liposome platform in cancer drug targeting. *J. Liposome Res.* **2006,** *16*, 175-83.
(38) Mattheolabakis, G.; Rigas, B.; Constantinides, P. P. Nanodelivery strategies in cancer chemotherapy: Biological rationale and pharmaceutical perspectives. *Nanomedicine* **2012,** *7*, 1577-90.
(39) Vonarbourg, A.; Passirani, C.; Saulnier, P.; Simard, P.; Leroux, J. C.; Benoit, J. P. Evaluation of pegylated lipid nanocapsules versus complement system activation and macrophage uptake. *J. Biomed. Mater. Res. A* **2006,** *78*, 620-8.
(40) Dong, S.; Roman, M. Fluorescently labeled cellulose nanocrystals for bioimaging applications. *J. Am. Chem. Soc.* **2007,** *129*, 13810-1.
(41) Johnston, H.; Pojana, G.; Zuin, S.; Jacobsen, N. R.; Moller, P.; Loft, S.; Semmler-Behnke, M.; McGuiness, C.; Balharry, D.; Marcomini, A.; Wallin, H.; Kreyling, W.; Donaldson, K.; Tran, L.; Stone, V. Engineered nanomaterial risk. Lessons learnt from completed nanotoxicology studies: Potential solutions to current and future challenges. *Crit. Rev. Toxicol.* **2013,** *43*, 1-20.
(42) Magdolenova, Z.; Collins, A.; Kumar, A.; Dhawan, A.; Stone, V.; Dusinska, M. Mechanisms of genotoxicity. A review of in vitro and in vivo studies with engineered nanoparticles. *Nanotoxicology* **2013**.
(43) Alkilany, A. M.; Murphy, C. J. Toxicity and cellular uptake of gold nanoparticles: What we have learned so far? *J. Nanopart. Res.* **2010,** *12*, 2313-33.
(44) Oberdorster, G.; Oberdorster, E.; Oberdorster, J. Nanotoxicology: an emerging discipline evolving from studies of ultrafine particles. *Environ. Health Perspect.* **2005,** *113*, 823-39.
(45) Carlsson, M.; Stenman, D.; Merenyi, G.; Reitberger, T. A comparative study on the degradation of cotton linters induced by carbonate and hydroxyl radicals generated from peroxynitrite. *Holzforschung* **2005,** *59*, 132-42.
(46) Sinha, T. J.; Vasudevan, P. Blood-cellulosics interactions. *Biomater. Med. Devices Artif. Organs* **1984,** *12*, 273-87.
(47) Holland, A. J.; Ford, W. D.; Bourne, A. J. Conservative surgery for benign non-parasitic splenic cysts. *Pediatr. Surg. Int.* **1997,** *12*, 353-5.
(48) Zhang, J.; Rana, S.; Srivastava, R. S.; Misra, R. D. On the chemical synthesis and drug delivery response of folate receptor-activated, polyethylene glycol-functionalized magnetite nanoparticles. *Acta Biomater.* **2008,** *4*, 40-8.
(49) Viet, D.; Beck-Candanedo, S.; Gray, D. G. Dispersion of cellulose nanocrystals in polar organic solvents. *Cellulose* **2007,** *14*, 109-13.
(50) Beck-Candanedo, S.; Roman, M.; Gray, D. G. Effect of reaction conditions on the properties and behavior of wood cellulose nanocrystal suspensions. *Biomacromolecules* **2005,** *6*, 1048-54.
(51) Lima, M. M. D.; Borsali, R. Rodlike cellulose microcrystals: Structure, properties, and applications. *Macromol. Rapid Commun.* **2004,** *25*, 771-87.
(52) Roman, M.; Dong, S.; Hirani, A.; Lee, Y. W., Cellulose nanocrystals for drug delivery. In *Polysaccharide materials: Performance by design*, American Chemical Society: 2009; Vol. 1017, pp 81-9.

(53) Lemarchand, C.; Gref, R.; Couvreur, P. Polysaccharide-decorated nanoparticles. *Eur. J. Pharm. Biopharm.* **2004,** *58*, 327-41.
(54) Hubbe, M. A.; Rojas, O.; Lucia, L. A.; Sain, M. Cellulosic nanocomposites: A review. *BioResources* **2008,** *3*, 929-80.
(55) Davalos, R. V.; Mir, I. L.; Rubinsky, B. Tissue ablation with irreversible electroporation. *Ann. Biomed. Eng.* **2005,** *33*, 223-31.
(56) Garcia, P. A.; Pancotto, T.; Rossmeisl, J. H., Jr.; Henao-Guerrero, N.; Gustafson, N. R.; Daniel, G. B.; Robertson, J. L.; Ellis, T. L.; Davalos, R. V. Non-thermal irreversible electroporation (n-tire) and adjuvant fractionated radiotherapeutic multimodal therapy for intracranial malignant glioma in a canine patient. *Technol. Cancer Res. Treat.* **2011,** *10*, 73-83.
(57) Maor, E.; Ivorra, A.; Leor, J.; Rubinsky, B. The effect of irreversible electroporation on blood vessels. *Technol. Cancer Res. Treat.* **2007,** *6*, 307-12.
(58) Li, W.; Fan, Q.; Ji, Z.; Qiu, X.; Li, Z. The effects of irreversible electroporation (IRE) on nerves. *PLoS One* **2011,** *6*, e18831-1-7.
(59) Mir, L. M.; Moller, P. H.; Andre, F.; Gehl, J. Electric pulse-mediated gene delivery to various animal tissues. *Adv. Genet.* **2005,** *54*, 83-114.
(60) Lavee, J.; Onik, G.; Mikus, P.; Rubinsky, B. A novel nonthermal energy source for surgical epicardial atrial ablation: Irreversible electroporation. *Heart. Surg. Forum* **2007,** *10*, E162-7.
(61) Miller, L.; Leor, J.; Rubinsky, B. Cancer cells ablation with irreversible electroporation. *Technol. Cancer Res. Treat.* **2005,** *4*, 699-705.
(62) Helenius, G.; Backdahl, H.; Bodin, A.; Nannmark, U.; Gatenholm, P.; Risberg, B. In vivo biocompatibility of bacterial cellulose. *J. Biomed. Mater. Res. A* **2006,** *76A*, 431-8.
(63) Hutson, J. R.; Stade, B.; Lehotay, D. C.; Collier, C. P.; Kapur, B. M. Folic acid transport to the human fetus is decreased in pregnancies with chronic alcohol exposure. *PLoS One* **2012,** *7*, e38057.
(64) Salazar, M. D.; Ratnam, M. The folate receptor: What does it promise in tissue-targeted therapeutics? *Cancer Metastasis Rev.* **2007,** *26*, 141-52.
(65) Edd, J. F.; Davalos, R. V. Mathematical modeling of irreversible electroporation for treatment planning. *Technol. Cancer Res. Treat.* **2007,** *6*, 275-86.
(66) Cooper, J. S.; Mukherji, S. K.; Toledano, A. Y.; Beldon, C.; Schmalfuss, I. M.; Amdur, R.; Sailer, S.; Loevner, L. A.; Kousouboris, P.; Ang, K. K.; Cormack, J.; Sicks, J. An evaluation of the variability of tumor-shape definition derived by experienced observers from ct images of supraglottic carcinomas (acrin protocol 6658). *Int. J. Radiat. Oncol. Biol. Phys.* **2007,** *67*, 972-5.
(67) O'Sullivan, F.; Roy, S.; O'Sullivan, J.; Vernon, C.; Eary, J. Incorporation of tumor shape into an assessment of spatial heterogeneity for human sarcomas imaged with fdg-pet. *Biostatistics* **2005,** *6*, 293-301.
(68) Raffa, V.; Riggio, C.; Smith, M. W.; Jordan, K. C.; Cao, W.; Cuschieri, A. BNNT-mediated irreversible electroporation: Its potential on cancer cells. *Technol. Cancer Res. Treat.* **2012,** *11*, 459-65.
(69) Kona, S.; Dong, J. F.; Liu, Y. L.; Tan, J. F.; Nguyen, K. T. Biodegradable nanoparticles mimicking platelet binding as a targeted and controlled drug delivery system. *Int. J. Pharm.* **2012,** *423*, 516-24.

(70) Bai, M.; Bornhop, D. J. Recent advances in receptor-targeted fluorescent probes for in vivo cancer imaging. *Curr. Med. Chem.* **2012,** *19*, 4742-58.
(71) Gaur, P. K.; Mishra, S.; Gupta, V. B.; Rathod, M. S.; Purohit, S.; Savla, B. A. Targeted drug delivery of rifampicin to the lungs: Formulation, characterization, and stability studies of preformed aerosolized liposome and in situ formed aerosolized liposome. *Drug Dev. Ind. Pharm.* **2010,** *36*, 638-46.
(72) Kamps, J. A. A. M.; Asgeirsdottir, S. A.; Morselt, H. W. M.; Bartsch, M.; Scherphof, G. L.; Molema, G. Targeted liposome mediated drug delivery into endothelial subsets and endothielial cells in inflammatory sites. *J. Vasc. Res.* **2006,** *43*, 10-.
(73) Wang, H. J.; Zhao, P. Q.; Su, W. Y.; Wang, S.; Liao, Z. Y.; Niu, R. F.; Chang, J. PLGA/polymeric liposome for targeted drug and gene co-delivery. *Biomaterials* **2010,** *31*, 8741-8.
(74) Asadishad, B.; Vosoughi, M.; Alamzadeh, I.; Tavakoli, A. Synthesis of folate-modified, polyethylene glycol-functionalized gold nanoparticles for targeted drug delivery. *J. Dispersion Sci. Technol.* **2010,** *31*, 492-500.
(75) Wang, Y. L.; Newell, B. B.; Irudayaraj, J. Folic acid protected silver nanocarriers for targeted drug delivery. *J. Biomed. Nanotechnol.* **2012,** *8*, 751-9.
(76) Cao, W. Q.; Zhou, J.; Mann, A.; Wang, Y.; Zhu, L. Folate-functionalized unimolecular micelles based on a degradable amphiphilic dendrimer-like star polymer for cancer cell-targeted drug delivery. *Biomacromolecules* **2011,** *12*, 2697-707.
(77) Sideratou, Z.; Kontoyianni, C.; Drossopoulou, G. I.; Paleos, C. M. Synthesis of a folate functionalized pegylated poly(propylene imine) dendrimer as prospective targeted drug delivery system. *Bioorg. Med. Chem. Lett.* **2010,** *20*, 6513-7.
(78) Owens, D. E.; Peppas, N. A. Opsonization, biodistribution, and pharmacokinetics of polymeric nanoparticles. *Int. J. Pharm.* **2006,** *307*, 93-102.
(79) Lacerda, L.; Herrero, M. A.; Venner, K.; Bianco, A.; Prato, M.; Kostarelos, K. Carbon-nanotube shape and individualization critical for renal excretion. *Small* **2008,** *4*, 1130-2.
(80) Fleming, K.; Gray, D. G.; Matthews, S. Cellulose crystallites. *Chemistry* **2001,** *7*, 1831-5.
(81) Skoog, D. A.; West, D. M.; Holler, F. J., *Fundamentals of analytical chemistry*. 7th ed.; Saunders College Pub.: Fort Worth, 1996.
(82) Isogai, A.; Kato, Y. Preparation of polyuronic acid from cellulose by tempo-mediated oxidation. *Cellulose* **1998,** *5*, 153-64.
(83) Lee, W. H.; Sonntag, W. E.; Mitschelen, M.; Yan, H.; Lee, Y. W. Irradiation induces regionally specific alterations in pro-inflammatory environments in rat brain. *Int. J. Radiat. Biol.* **2010,** *86*, 132-44.
(84) Sudimack, J.; Lee, R. J. Targeted drug delivery via the folate receptor. *Adv. Drug Del. Rev.* **2000,** *41*, 147-62.
(85) Reddy, J. A.; Dorton, R.; Westrick, E.; Dawson, A.; Smith, T.; Xu, L. C.; Vetzel, M.; Kleindl, P.; Vlahov, I. R.; Leamon, C. P. Preclinical evaluation of ec145, a folate-vinca alkaloid conjugate. *Cancer Res.* **2007,** *67*, 4434-42.
(86) Mathias, C. J.; Wang, S.; Lee, R. J.; Waters, D. J.; Low, P. S.; Green, M. A. Tumor-selective radiopharmaceutical targeting via receptor-mediated endocytosis of gallium-67-deferoxamine-folate. *J. Nucl. Med.* **1996,** *37*, 1003-8.
(87) Low, P. S.; Antony, A. C. Folate receptor-targeted drugs for cancer and inflammatory diseases. *Adv. Drug Del. Rev.* **2004,** *56*, 1055-8.

(88) Nukolova, N. V.; Oberoi, H. S.; Cohen, S. M.; Kabanov, A. V.; Bronich, T. K. Folate-decorated nanogels for targeted therapy of ovarian cancer. *Biomaterials* **2011,** *32*, 5417-26.
(89) Low, P. S.; Kularatne, S. A. Folate-targeted therapeutic and imaging agents for cancer. *Curr. Opin. Chem. Biol.* **2009,** *13*, 256-62.
(90) Gabrielson, N. P.; Pack, D. W. Efficient polyethylenimine-mediated gene delivery proceeds via a caveolar pathway in hela cells. *J. Controlled Release* **2009,** *136*, 54-61.
(91) Chen, L.; Xiong, S.; She, H.; Lin, S. W.; Wang, J.; Tsukamoto, H. Iron causes interactions of TAK1, p21ras, and phosphatidylinositol 3-kinase in caveolae to activate ikappab kinase in hepatic macrophages. *J. Biol. Chem.* **2007,** *282*, 5582-8.
(92) Gumbleton, M.; Abulrob, A. G.; Campbell, L. Caveolae: an alternative membrane transport compartment. *Pharm. Res.* **2000,** *17*, 1035-48.
(93) Rejman, J.; Bragonzi, A.; Conese, M. Role of clathrin- and caveolae-mediated endocytosis in gene transfer mediated by lipo- and polyplexes. *Mol. Ther.* **2005,** *12*, 468-74.
(94) Momparler, R. L.; Karon, M.; Siegel, S. E.; Avila, F. Effect of adriamycin on DNA, rna, and protein synthesis in cell-free systems and intact cells. *Cancer Res.* **1976,** *36*, 2891-5.
(95) Saftig, P.; Klumperman, J. Lysosome biogenesis and lysosomal membrane proteins: Trafficking meets function. *Nat. Rev. Mol. Cell Biol.* **2009,** *10*, 623-35.
(96) Lee, R. J.; Wang, S.; Low, P. S. Measurement of endosome pH following folate receptor-mediated endocytosis. *Biochim. Biophys. Acta* **1996,** *1312*, 237-42.
(97) Schmid, B.; Chung, D. E.; Warnecke, A.; Fichtner, I.; Kratz, F. Albumin-binding prodrugs of camptothecin and doxorubicin with an ala-leu-ala-leu-linker that are cleaved by cathepsin b: Synthesis and antitumor efficacy. *Bioconjugate Chem.* **2007,** *18*, 702-16.
(98) Ross, J. F.; Chaudhuri, P. K.; Ratnam, M. Differential regulation of folate receptor isoforms in normal and malignant tissues in vivo and in established cell lines. Physiologic and clinical implications. *Cancer* **1994,** *73*, 2432-43.
(99) American Cancer Society. www.cancer.org (*June 7th, 2013*).
(100) American Lung Association. www.lung.org (*June 7th, 2013*).
(101) National Cancer Institute. Seer cancer statistics review, 1975-2009. **2012**.
(102) Mohammed, A.; Janakiram, N. B.; Lightfoot, S.; Gali, H.; Vibhudutta, A.; Rao, C. V. Early detection and prevention of pancreatic cancer: Use of genetically engineered mouse models and advanced imaging technologies. *Curr. Med. Chem.* **2012,** *19*, 3701-13.
(103) Reisfeld, B.; Metzler, C. P.; Lyons, M. A.; Mayeno, A. N.; Brooks, E. J.; Degroote, M. A. A physiologically based pharmacokinetic model for capreomycin. *Antimicrob. Agents Chemother.* **2012,** *56*, 926-34.
(104) Jones, H. M.; Parrott, N.; Jorga, K.; Lave, T. A novel strategy for physiologically based predictions of human pharmacokinetics. *Clin. Pharmacokinet.* **2006,** *45*, 511-42.
(105) Fani, M.; Tamma, M. L.; Nicolas, G. P.; Lasri, E.; Medina, C.; Raynal, I.; Port, M.; Weber, W. A.; Maecke, H. R. In vivo imaging of folate receptor positive tumor xenografts using novel 68ga-nodaga-folate conjugates. *Mol. Pharm.* **2012,** *9*, 1136-45.
(106) Wu, G.; Qiu, X. L.; Zhou, L.; Zhu, J.; Chamberlin, R.; Lau, J.; Chen, P. L.; Lee, W. H. Small molecule targeting the hec1/nek2 mitotic pathway suppresses tumor cell growth in culture and in animal. *Cancer Res.* **2008,** *68*, 8393-9.

(107) Meier, R.; Henning, T. D.; Boddington, S.; Tavri, S.; Arora, S.; Piontek, G.; Rudelius, M.; Corot, C.; Daldrup-Link, H. E. Breast cancers: Mr imaging of folate-receptor expression with the folate-specific nanoparticle p1133. *Radiology* **2010,** *255*, 527-35.
(108) Zhang, X.; Guo, S.; Fan, R.; Yu, M.; Li, F.; Zhu, C.; Gan, Y. Dual-functional liposome for tumor targeting and overcoming multidrug resistance in hepatocellular carcinoma cells. *Biomaterials* **2012,** *33*, 7103-14.
(109) Evjen, T. J.; Hagtvet, E.; Nilssen, E. A.; Brandl, M.; Fossheim, S. L. Sonosensitive dioleoylphosphatidylethanolamine-containing liposomes with prolonged blood circulation time of doxorubicin. *Eur. J. Pharm. Sci.* **2011,** *43*, 318-24.
(110) Mouton, J. W.; Theuretzbacher, U.; Craig, W. A.; Tulkens, P. M.; Derendorf, H.; Cars, O. Tissue concentrations: Do we ever learn? *J. Antimicrob. Chemother.* **2008,** *61*, 235-7.
(111) Wohl-Bruhn, S.; Badar, M.; Bertz, A.; Tiersch, B.; Koetz, J.; Menzel, H.; Mueller, P. P.; Bunjes, H. Comparison of in vitro and in vivo protein release from hydrogel systems. *J. Controlled Release* **2012,** *162*, 127-33.
(112) Cheng, K. C.; Catchmark, J. M.; Demirci, A. Enhanced production of bacterial cellulose by using a biofilm reactor and its material property analysis. *J. Biol. Eng.* **2009,** *3*, 12.
(113) Saito, T.; Nishiyama, Y.; Putaux, J. L.; Vignon, M.; Isogai, A. Homogeneous suspensions of individualized microfibrils from tempo-catalyzed oxidation of native cellulose. *Biomacromolecules* **2006,** *7*, 1687-91.
(114) Tasciotti, E.; Liu, X. W.; Bhavane, R.; Plant, K.; Leonard, A. D.; Price, B. K.; Cheng, M. M. C.; Decuzzi, P.; Tour, J. M.; Robertson, F.; Ferrari, M. Mesoporous silicon particles as a multistage delivery system for imaging and therapeutic applications. *Nat. Nanotechnol.* **2008,** *3*, 151-7.
(115) Thomson, K. R.; Cheung, W.; Ellis, S. J.; Federman, D.; Kavnoudias, H.; Loader-Oliver, D.; Roberts, S.; Evans, P.; Ball, C.; Haydon, A. Investigation of the safety of irreversible electroporation in humans. *J. Vasc. Interv. Radiol.* **2011,** *22*, 611-21.
(116) Neal, R. E., 2nd; Rossmeisl, J. H., Jr.; Garcia, P. A.; Lanz, O. I.; Henao-Guerrero, N.; Davalos, R. V. Successful treatment of a large soft tissue sarcoma with irreversible electroporation. *J. Clin. Oncol.* **2011,** *29*, e372-7.
(117) Lee, E. W.; Loh, C. T.; Kee, S. T. Imaging guided percutaneous irreversible electroporation: Ultrasound and immunohistological correlation. *Technol. Cancer Res. Treat.* **2007,** *6*, 287-93.
(118) Weaver, J. C.; Smith, K. C.; Esser, A. T.; Son, R. S.; Gowrishankar, T. R. A brief overview of electroporation pulse strength-duration space: A region where additional intracellular effects are expected. *Bioelectrochemistry* **2012,** *87*, 236-43.
(119) Apollonio, F.; Liberti, M.; Marracino, P.; Mir, L. In *Electroporation mechanism: Review of molecular models based on computer simulation*, 2012 6th European Conference on Antennas and Propagation (EUCAP), 26-30 March 2012, 2012; 2012; pp 356-8.
(120) Marszalek, P.; Liu, D. S.; Tsong, T. Y. Schwan equation and transmembrane potential induced by alternating electric field. *Biophys. J.* **1990,** *58*, 1053-8.
(121) Davalos, R. V.; Rubinsky, B. Temperature considerations during irreversible electroporation. *Int. J. Heat Mass Transfer* **2008,** *51*, 5617-22.
(122) Ciofani, G.; Ricotti, L.; Danti, S.; Moscato, S.; Nesti, C.; D'Alessandro, D.; Dinucci, D.; Chiellini, F.; Pietrabissa, A.; Petrini, M.; Menciassi, A. Investigation of interactions between poly-l-lysine-coated boron nitride nanotubes and c2c12 cells: Up-take, cytocompatibility, and differentiation. *Int. J. Nanomed.* **2010,** *5*, 285-98.

(123) Horvath, L.; Magrez, A.; Golberg, D.; Zhi, C.; Bando, Y.; Smajda, R.; Horvath, E.; Forro, L.; Schwaller, B. In vitro investigation of the cellular toxicity of boron nitride nanotubes. *ACS nano* **2011,** *5*, 3800-10.
(124) Csoka, L.; Hoeger, I. C.; Peralta, P.; Peszlen, I.; Rojas, O. J. Dielectrophoresis of cellulose nanocrystals and alignment in ultrathin films by electric field-assisted shear assembly. *J. Colloid Interface Sci.* **2011,** *363*, 206-12.
(125) Habibi, Y.; Lucia, L. A.; Rojas, O. J. Cellulose nanocrystals: Chemistry, self-assembly, and applications. *Chem. Rev.* **2010,** *110*, 3479-500.
(126) Lu, Y.; Sega, E.; Leamon, C. P.; Low, P. S. Folate receptor-targeted immunotherapy of cancer: Mechanism and therapeutic potential. *Adv. Drug Del. Rev.* **2004,** *56*, 1161-76.
(127) Rochman, H.; Selhub, J.; Karrison, T. Folate binding protein and the estrogen receptor in breast cancer. *Cancer Detect. Prev.* **1985,** *8*, 71-5.
(128) Krassowska, W.; Nanda, G. S.; Austin, M. B.; Dev, S. B.; Rabussay, D. P. Viability of cancer cells exposed to pulsed electric fields: the role of pulse charge. *Ann. Biomed. Eng.* **2003,** *31*, 80-90.
(129) Saulis, G.; Venslauskas, M. S. Cell electroporation: Part 1. Theoretical simulation of the process of pore formation in a cell. *Bioelectrochem. Bioenerg.* **1993,** *32*, 221-35.
(130) Pucihar, G.; Krmelj, J.; Rebersek, M.; Napotnik, T. B.; Miklavcic, D. Equivalent pulse parameters for electroporation. *IEEE Trans. Biomed. Eng.* **2011,** *58*, 3279-88.
(131) Arena, C. B.; Szot, C. S.; Garcia, P. A.; Rylander, M. N.; Davalos, R. V. A three-dimensional in vitro tumor platform for modeling therapeutic irreversible electroporation. *Biophys. J.* **2012,** *103*, 2033-42.
(132) Sel, D.; Cukjati, D.; Batiuskaite, D.; Slivnik, T.; Mir, L. M.; Miklavcic, D. Sequential finite element model of tissue electropermeabilization. *IEEE Trans. Biomed. Eng.* **2005,** *52*, 816-27.
(133) Onik, G.; Mikus, P.; Rubinsky, B. Irreversible electroporation: Implications for prostate ablation. *Technol. Cancer Res. Treat.* **2007,** *6*, 295-300.
(134) Rubinsky, B.; Onik, G.; Mikus, P. Irreversible electroporation: a new ablation modality--clinical implications. *Technol. Cancer Res. Treat.* **2007,** *6*, 37-48.
(135) Arena, C. B.; Rylander, M. N.; Davalos, R. V. In *Pilot study on the enhancement of irreversible electroporation (IRE) with carbon nanotubes (cnt)*, ASME Summer Bioengineering Conference, Lake Tahoe, CA, 2009; ASME: Lake Tahoe, CA, 2009; pp 347-8.
(136) Bonnafous, P.; Vernhes, M.; Teissie, J.; Gabriel, B. The generation of reactive-oxygen species associated with long-lasting pulse-induced electropermeabilisation of mammalian cells is based on a non-destructive alteration of the plasma membrane. *Biochim. Biophys. Acta* **1999,** *1461*, 123-34.
(137) Hofmann, G. A. The optimizor: a graphic pulse analyzer to monitor electro cell fusion and electroporation experiments. *BioTechniques* **1988,** *6*, 996-1003.
(138) Hulsheger, H.; Niemann, E. G. Lethal effects of high-voltage pulses on e. Coli k12. *Radiat. Environ. Biophys.* **1980,** *18*, 281-8.
(139) Lubicki, P.; Jayaram, S. High voltage pulse application for the destruction of the gram-negative bacterium yersinia enterocolitica. *Bioelectrochem. Bioenerg.* **1997,** *43*, 135-41.
(140) Tieleman, D. P. The molecular basis of electroporation. *BMC Biochem.* **2004,** *5*, 10.
(141) Jing-Bo, L.; Ying, Y.; Bing, Y.; Xiang-Bing, M.; Zhi-Qing, H.; Guo-Quan, H.; Hong, C.; Dai-Wen, C. Folic acid supplementation prevents the changes in hepatic promoter

methylation status and gene expression in intrauterine growth-retarded piglets during early weaning period. *J. Anim. Physiol. Anim. Nutr.* **2012**.

(142) Szot, C. S.; Buchanan, C. F.; Freeman, J. W.; Rylander, M. N. 3d in vitro bioengineered tumors based on collagen i hydrogels. *Biomaterials* **2011,** *32*, 7905-12.

(143) Raeber, G. P.; Lutolf, M. P.; Hubbell, J. A. Molecularly engineered peg hydrogels: a novel model system for proteolytically mediated cell migration. *Biophys. J.* **2005,** *89*, 1374-88.

(144) Lee, C. H.; Singla, A.; Lee, Y. Biomedical applications of collagen. *Int. J. Pharm.* **2001,** *221*, 1-22.

(145) Paszek, M. J.; Zahir, N.; Johnson, K. R.; Lakins, J. N.; Rozenberg, G. I.; Gefen, A.; Reinhart-King, C. A.; Margulies, S. S.; Dembo, M.; Boettiger, D.; Hammer, D. A.; Weaver, V. M. Tensional homeostasis and the malignant phenotype. *Cancer Cell* **2005,** *8*, 241-54.

(146) Yamada, K. M.; Cukierman, E. Modeling tissue morphogenesis and cancer in 3d. *Cell* **2007,** *130*, 601-10.

(147) Kim, J. B. Three-dimensional tissue culture models in cancer biology. *Semin. Cancer Biol.* **2005,** *15*, 365-77.

(148) Kim, J. B.; Stein, R.; O'Hare, M. J. Three-dimensional in vitro tissue culture models of breast cancer-- a review. *Breast Cancer Res. Treat.* **2004,** *85*, 281-91.

(149) Fischbach, C.; Chen, R.; Matsumoto, T.; Schmelzle, T.; Brugge, J. S.; Polverini, P. J.; Mooney, D. J. Engineering tumors with 3d scaffolds. *Nat. Methods* **2007,** *4*, 855-60.

(150) Yallapu, M. M.; Dobberpuhl, M. R.; Maher, D. M.; Jaggi, M.; Chauhan, S. C. Design of curcumin loaded cellulose nanoparticles for prostate cancer. *Curr. Drug Metab.* **2012,** *13*, 120-8.

(151) Frieboes, H. B.; Wu, M.; Lowengrub, J.; Decuzzi, P.; Cristini, V. A computational model for predicting nanoparticle accumulation in tumor vasculature. *PLoS One* **2013,** *8*, e56876.

Appendix A: Code for PBPK model developed in Chapter 3.

The current state of the model is experiencing an implementation issue and will be resolved before the submission of this ETD. Currently added is the code in its current state. This section will be revised before submission.

Appendix B: Co-Authored Work

Shuping Dong[1], Anjali A. Hirani[2], Katelyn R. Colacino[2], Yong Woo Lee[2, 3], Maren Roman[1]

[1]Macromolecules and Interfaces Institute and Department of Sustainable Biomaterials, Virginia Tech, Blacksburg, VA

[2]School of Biomedical Engineering and Sciences, Virginia Tech-Wake Forest University, Blacksburg, VA

[3]Department of Biomedical Sciences and Pathobiology, Virginia-Maryland Regional College of Veterinary Medicine, Virginia Tech, Blacksburg, VA

Manuscript has been accepted to NanoLIFE, July 17th 2012.
DOI: 10.1142/S1793984412410061

The following paper was a collaborative effort directly related to the work presented in this dissertation.